

**ADVERTIMENT.** L'accés als continguts d'aquesta tesi queda condicionat a l'acceptació de les condicions d'ús establertes per la següent llicència Creative Commons:  [http://cat.creativecommons.org/?page\\_id=184](http://cat.creativecommons.org/?page_id=184)

**ADVERTENCIA.** El acceso a los contenidos de esta tesis queda condicionado a la aceptación de las condiciones de uso establecidas por la siguiente licencia Creative Commons:  <http://es.creativecommons.org/blog/licencias/>

**WARNING.** The access to the contents of this doctoral thesis it is limited to the acceptance of the use conditions set by the following Creative Commons license:  <https://creativecommons.org/licenses/?lang=en>



Universitat Autònoma de Barcelona

TESIS DOCTORAL

# Halide Perovskite Solar Cells: Strategies for High Stability

DEFENDED BY:

José Carlos Pereyra Marina

THESIS DIRECTOR:

Prof. Mónica Lira-Cantú

PROGRAMA DE DOCTORAT EN QUÍMICA  
UNIVERSITAT AUTÒNOMA DE BARCELONA  
DEPTARTAMENT DE QUÍMICA  
FACULTAT DE CIÈNCIES  
February 22



ICN2<sup>R</sup>



EXCELENCIA  
SEVERO  
OCHOA

**Institut Català  
de Nanociència  
i Nanotecnologia**

Institut Català de Nanociència i Nanotecnologia ICN2  
Idifici ICN2 Campus UAB  
08193 Bellaterra, Barcelona

Universitat Autònoma de Barcelona  
Departament de Química  
08193 Bellaterra, Barcelona

**Memòria presentada per aspirar al Grau de Doctor per José Carlos  
Pereyra Marina:**

---

**José Carlos Pereyra Marina**

La Prof. Mónica Lira-Cantú, responsable del Nanostructured Materials for Photovoltaic Energy Group, al centre d'investigació Institut Català de Nanociència i Nanotecnologia (ICN2).

Certifica que el treball descrit en aquesta tesi titulada: “Halide Perovskite Solar Cells: Strategies for High Stability”, presentada per José Carlos Pereyra Marina per optar al grau de Doctor, ha estat realitzada sota la seva direcció.

---

Prof. Mónica Lira-Cantú

Vist i plau del tutor de la tesi:

---

Dra. María Muñoz Tapia

A Bellaterra, al febrer del 2022





***To my family.***

*“Where life begins & love never ends”*



# Contents

---

## Table of Contents

<b><i>Abstract</i></b>	<b>1</b>
<b><i>Resum</i></b>	<b>3</b>
<b><i>Abbreviations &amp; Symbols</i></b>	<b>5</b>
<b><i>Synonyms</i></b>	<b>7</b>
<b><i>List of Figures</i></b>	<b>9</b>
<b><i>List of Tables</i></b>	<b>15</b>
<b><i>1. Chapter 1: Introduction</i></b>	<b>17</b>
<b>1.1. Current status of photovoltaic devices</b>	<b>17</b>
<b>1.2. Development and marketing</b>	<b>19</b>
<b>1.3. Configurations of solar cells</b>	<b>22</b>
<b>1.4. PSC Principles</b>	<b>24</b>
1.4.1. Perovskite crystal structure	25
1.4.2. Optical properties	26
1.4.3. Electronic properties and charge recombination	27
1.4.4. Chemistry of metal halide perovskites	28
1.4.5. Halide Perovskite Solar Cells	30
1.4.6. Stability of metal halide perovskites	32
<b>1.5. Objectives of the thesis</b>	<b>33</b>
1.5.1. General objectives	33
1.5.2. Specific objectives	34
<b>1.6. Scope of the thesis work</b>	<b>35</b>
<b>1.7. References</b>	<b>37</b>
<b><i>2. Chapter 2: Additive Engineering in Halide Perovskite Solar Cells</i></b>	<b>41</b>
<b>2.1. Introduction</b>	<b>41</b>
<b>2.2. Results</b>	<b>43</b>
2.2.1. Additive selection	43
2.2.2. Photovoltaic performance and recombination dynamics	47
2.2.3. Device stability and ion immobilization	53

2.2.4.	Effect of H3pp on the perovskite thin film: microstructure and binding mode	58
2.2.5.	Passivation of shallow point defects in the HP absorber	66
<b>2.3.</b>	<b>Discussions</b>	<b>68</b>
<b>2.4.</b>	<b>References</b>	<b>70</b>
<b>3.</b>	<b><i>Chapter 3: Carbon-based Perovskite Solar Cells</i></b>	<b>75</b>
<b>3.1.</b>	<b>Introduction</b>	<b>75</b>
<b>3.2.</b>	<b>Results</b>	<b>78</b>
3.2.1.	Photovoltaic performance	78
3.2.2.	Device stability	82
<b>3.3.</b>	<b>Discussions</b>	<b>88</b>
<b>3.4.</b>	<b>References</b>	<b>90</b>
<b>4.</b>	<b><i>Chapter 4: Ferroelectric oxide/Halide Perovskite Solar Cells</i></b>	<b>93</b>
<b>4.1.</b>	<b>Introduction</b>	<b>93</b>
<b>4.2.</b>	<b>Results</b>	<b>99</b>
4.2.1.	Synthesis and characterization of BFO	99
4.2.2.	Photovoltaic response of PSCs with BFO as ETL	106
4.2.3.	Poling Method	108
4.2.4.	Grain Size in BFO/Perovskite heterojunctions, charge transport and efficiency	115
4.2.5.	Switching properties	120
4.2.6.	Stability	122
<b>4.3.</b>	<b>Discussions</b>	<b>124</b>
<b>4.4.</b>	<b>References</b>	<b>126</b>
<b>5.</b>	<b><i>Chapter 5: Material and Methodology</i></b>	<b>131</b>
<b>5.1.</b>	<b>Materials</b>	<b>131</b>
5.1.1.	Chemical and solvents	131
<b>5.2.</b>	<b>Methodology</b>	<b>132</b>
5.2.1.	Device fabrication	132
5.2.2.	Characterization	139
<b>5.3.</b>	<b>References</b>	<b>155</b>
<b>6.</b>	<b><i>Chapter 6: General Conclusions</i></b>	<b>156</b>
	<b><i>List of Publications</i></b>	<b>161</b>
	<b><i>Acknowledgements</i></b>	<b>163</b>

# Abstract

---

Among the most advanced emerging photovoltaic technologies, halide perovskite solar cells (PSCs) have evolved significantly in only a few years, achieving certified power conversion efficiencies (PCE) above 25%. However, some drawbacks of the technology that limits their commercialization are the presence of toxic Pb-based materials, limitations in the scale-up of the technology and most important, its long-term stability under continuous operation. Semiconductor oxides (including graphene oxide) have been employed as excellent barrier layers due to their low fabrication cost and ease of synthesis, but above all, due to the properties of stability and long life that provide to the final PSC device. In this thesis, we propose three strategies to overcome instability issues in PSCs: (a) additive engineering on the halide perovskite adsorbed (Chapter 2), (b) the fabrication of carbon-based PSCs (Chapter 3) and (c), the replacement of classical semiconductor oxides for ferroelectric oxides as transport layers (Chapter 4).

I initiate the description of this work with a brief introduction to the topic of energy and perovskite solar cells (Chapter 1). The I present the three different strategies employed to enhance PSC stability. The first strategy, described in Chapter 2, includes the use of organic additives with phosphonate and carboxylic functional groups that are able to passive shallow point defects, resulting in ion immobilization and the enhancement of the PSC stability. The use of Carbon-based electrodes in PSC (Chapter 3) have demonstrated to

improve moisture resistance and thus, overall solar cell performance. In this section, I will present the most recent results on the fabrication of complete PSCs applying carbon electrodes. Finally, I describe the work carried out on the replacement of classical semiconductor oxides applied in PSC as transport layers (such as  $\text{TiO}_2$  or  $\text{SnO}_2$ ), by ferroelectric oxides, especially Lead Zirconate Titanate (PZT) and Bismuth Ferrite (BFO). Initial studies with PZT have shown that the detrimental oxygen vacancies present in semiconductor oxides, which degrade the halide perovskite, are linked to the polarization properties in ferroelectric oxide and not to the photodegradation of the device. Finally, Chapter 5 and 6 describe the different methodologies employed in this thesis and the conclusion of the work, respectively.

# Resum

---

Entre les tecnologies fotovoltaiques emergents més avançades, les cel·les solars de perovskita d'halur (PSC) han evolucionat significativament en tant sols uns pocs anys, aconseguint eficiències de conversió d'energia certificades (PCE) superiors al 25%. No obstant això, alguns dels inconvenients de la tecnologia que limita la seva comercialització és la presència de materials tòxics a base de Pb, limitacions en l'escalat de la tecnologia, i el més important, la seva estabilitat a llarg termini en operació contínua. Els òxids semiconductors (inclòs l'òxid de grafè) s'han emprat com a excel·lents capes de barrera a causa del seu baix cost de fabricació i facilitat de síntesi, però, sobretot, per les propietats d'estabilitat i llarga vida que li confereixen al dispositiu PSC final. En aquesta tesi, proposem tres estratègies per superar els problemes d'estabilitat en les PSC: (a) enginyeria additiva en la perovskita d'halur adsorbida (Capítol 2), (b), la fabricació de PSC basada en carbó (Capítol 3) i (c), la substitució d'òxids semiconductors clàssics per òxids ferroelèctrics com a capes de transport (Capítol 4). Iniciem la descripció del següent treball amb una breu introducció al tema de l'energia i les cel·les solars de perovskita (Capítol 1). Seguidament, presentem les tres estratègies diferents emprades per millorar l'estabilitat de les PSC. La primera estratègia, descrita al Capítol 2, inclou l'ús d'additius orgànics amb grups funcionals de fosfonat i carboxílics que son capaços de passivar defectes puntuals poc profunds, el que dona com a resultat d'immobilització d'ions i la millora de l'estabilitat de les PSC. S'ha demostrat que la utilització



d'elèctrodes a base de carboni en les PSC (Capítol 3) millora la resistència a la humitat i, per tant, el rendiment general de les cel·les solars. En aquesta secció, presentarem els resultats més recents sobre la fabricació de PSC completes aplicant elèctrodes de carboni. Finalment, descrivim el treball realitzat sobre la substitució d'òxids semiconductors clàssics aplicats a les PSC com a capes de transport (com  $\text{TiO}_2$  o  $\text{SnO}_2$ ), per òxids ferroelèctrics, especialment Titanat de Plom Zirconat (PZT) i Ferrita de Bismut (BFO). Els estudis inicials amb PZT han demostrat que les vacants d'oxigen perjudicials presents als òxids semiconductors, que degraden la perovskita d'halur, estan relacionades amb les propietats de polarització de l'òxid ferroelèctric i no amb la fotodegradació del dispositiu. Finalment, els Capítols 5 i 6 descriuen les diferents metodologies emprades en aquesta tesi i la conclusió del treball, respectivament.

# Abbreviations & Symbols

---

ACN	Acetonitrile	FTIR	Fourier transform infrared spectroscopy
Ag	Silver		
Au	Gold	$\eta$	efficiency
Ar	Argon	H3pp	3-phosphono propionic acid
C	Carbon		
CB	Conduction band	h	Hour
CE	Counter electrode	HP	Perovskite
c-TiO <sub>2</sub>	Compact titanium dioxide	HTM	Hole transport material
DMSO	Dimethylsulfoxide	IPCE	Incident photon-to-current efficiency
DSC	Dye sensitized solar cell	ITO	Indium tin oxide
e <sup>-</sup>	Electron	I-V curves	Current-Voltage curves
EDS	Energy disperse x-ray spectroscopy	J <sub>sc</sub>	Short-circuit current density (mA/cm <sup>2</sup> )
EDX	Energy disperse x-ray Spectroscopy		
E <sub>g</sub>	Band gap	J-V curves	Current Density-Voltage curves
EELS	Electron energy loss spectroscopy	K <sub>B</sub>	Boltzmann's constant
EIS	Electrochemical impedance spectroscopy	m-TiO <sub>2</sub>	Mesoporous titanium dioxide
EQE	External quantum efficiency	min	Minute
ETM	Electron transport material	NP	Nanoparticle
FA	Formamidinium	ns	nanoseconds
FF	Fill factor (%)	PCE	Power conversion efficiency (%)
FTO	Fluorinated indium tin oxide	PSC	Perovskite solar cell

C-PSC	Carbon based Perovskite solar cell	RT	Room temperature
$P_{in}$	Power incident light	XPS	X-ray Photoelectron Spectroscopy
PL	Photoluminescence	$O_{vac}$	Oxygen Vacancies
$P_{max}$	Power at the maximum power point	BFO	Bismuth Ferrite
Pt	Platinum	PZT	Lead Zirconate Titanate
rpm	Revolutions per minute	$SnO_2$	Tin(IV) oxide
$R_s$	Series resistance	UPS	Ultraviolet photoelectron spectroscopy
$R_{sh}$	Shunt resistance	AFM	Atomic force microscopy
s	Second	DMF	Dimethyl- formamide
SEM	Scanning electron microscopy	MPP	Maximum power point
T	Temperature		
TCO	Transparent conductive oxide		
TEM	Transmission electron microscopy		
TRPL	Time resolved photoluminescence		
TPC	Transient photocurrent		
OCVD	Open circuit voltage decay		
OPTP	Optical pump-THz probe		
UV	Ultraviolet		
VB	Valence band		
$V_{oc}$	Open-circuit voltage (V)		
XRD	X-ray diffraction		

# Synonyms

---

Dye sensitized solar cells (DSC)

Efficiency

Electron Transport layer (ETL)

Hole Transport Layer (HTL)

Isopropanol

IPCE

n-type material

p-type material

Solar Cell (SC)

Grätzel cells

Power Conversion Efficiency

Acceptor material

Donor material

2-propanol

EQE

Electron Transport Material (ETM)

Hole Transport Material (HTM)

Photovoltaic Cell (PV)



# List of Figures

FIGURE 1.1. ESTIMATED RENEWABLE SHARE OF TOTAL FINAL ENERGY CONSUMPTION, 2020 [1].....	18
FIGURE 1.2. A) MONOCRYSTALLINE SILICON SOLAR CELL [11], B) THIN FILM CdTe SOLAR CELL [12], C) FLEXIBLE CIGS THIN-FILM SOLAR CELL [13] AND D) POLYMER SOLAR CELL [14]. ....	21
FIGURE 1.3. BEST RESEARCH-CELL EFFICIENCIES [15].....	22
FIGURE 1.4. TYPICAL SCHEMES OF DIFFERENT GENERATIONS OF SOLAR CELLS, (A) CRYSTALLINE SILICON[16], (B) CdTe THIN FILM, (C) CIGS THIN FILM[11] AND (D) PEROVSKITE[17] .....	23
FIGURE 1.5. THE BEST EFFICIENCIES OF PEROVSKITE SOLAR CELLS [18]. ....	24
FIGURE 1.6. THE CRYSTAL STRUCTURE OF THE PEROVSKITE. ....	26
FIGURE 1.7. SCHEMATIC ILLUSTRATION OF DIFFERENT RECOMBINATION PROCESSES [35]. ....	28
FIGURE 1.8. SCHEMATIC CRYSTAL STRUCTURES OF THE BROAD FAMILY OF HYBRID PEROVSKITES [37]. ....	30
FIGURE 1.9. BAND DIAGRAM AND OPERATION PRINCIPLE OF PEROVSKITE SOLAR CELL [39]. ...	32
FIGURE 1.10. DEGRADATION PATHWAYS OF THE PEROVSKITE MATERIAL [41].....	33
FIGURE 2.1. PERFORMANCE OF PEROVSKITE SOLAR CELLS DOPED WITH DIFFERENT ORGANIC ADDITIVES OF THE PHOSPHONOPROPIONIC ACID FAMILY. PHOSPHONOACETIC ACID (H2PP), 3-PHOSPHONOPROPIONIC ACID (H3PP), 6-PHOSPHONOPROPIONIC ACID (H6PP) AND 16-PHOSPHONOPROPIONIC ACID (H16PP) AND 4-METHOXYBENZYLPHOSPHONIC ACID (4-METHOX). ....	45
FIGURE 2.2. OPTOELECTRONIC PROPERTIES OF THE PSCs AS A FUNCTION OF H3PP CONCENTRATION. A, POWER CONVERSION EFFICIENCY (PCE), B, SHORT CIRCUIT CURRENT ( $J_{sc}$ ), C, OPEN CIRCUIT VOLTAGE ( $V_{oc}$ ) AND D, FILL FACTOR (FF). H3PP: RbCsMAFA PEROVSKITE = 1:500, 1:250, 1:150, 1:75, 1:50, 1:25 AND 1:12.5 (MOLAR RATIO). ....	46
FIGURE 2.3. A, OPTOELECTRONIC PARAMETERS OF THE BEST DEVICE WITH H3PP: RbCsMAFA PEROVSKITE = 1:500 (MOLAR RATIO). B, IPCE OF THE CHAMPION H3PP-DOPED RbCsMAFA PEROVSKITE SOLAR CELL (1:500). THE INTEGRATED $J_{sc}$ FOR THE DEVICE IS 23.7 MA/CM <sup>2</sup> , IN AGREEMENT WITH THE MEASURED $J_{sc}$ OF 24.5 MA/CM <sup>2</sup> . STATISTIC OPTOELECTRONIC PROPERTIES OF THE REFERENCE AND H3PP-DOPED PSCs (1:500): C, $J_{sc}$ . D, $V_{oc}$ . E, FF AND F, HYSTERESIS INDEX (HI). HI = (PCEREVERSE-PCEFORWARD)/PCEREVERSE. ....	48
FIGURE 2.4. CHARACTERIZATION MADE TO COMPLETE PSC DEVICES OF THE TYPE FTO/C-TiO <sub>2</sub> /M-TiO <sub>2</sub> /HP/SPIRO- OMeTAD/Au WITH (ORANGE) AND WITHOUT (BLUE) THE H3PP ADDITIVE. (A) LIGHT INTENSITY DEPENDENT $V_{oc}$ ; (B) TRANSIENT PHOTOCURRENT, AND (C) OPEN CIRCUIT VOLTAGE DECAY. IN ALL CASES SIMILAR $J_{sc}$ AND $V_{oc}$ WITH (ORANGE) AND WITHOUT H3PP ADDITIVE (BLUE) ARE OBSERVED. ....	50
FIGURE 2.5. TRPL FOR THE HP (BLUE) AND THE 1:500 H3PP:HP RATIO (ORANGE) ON GLASS. ....	51
FIGURE 2.6. SPACE-CHARGE-LIMITED CURRENT (SCLC) FOR ELECTRON-ONLY (A) AND HOLE-ONLY (B) DEVICES WITH AND WITHOUT THE ADDITION OF THE H3PP ADDITIVE. ....	53
FIGURE 2.7. OPERATIONAL STABILITY OF PSCs APPLYING RbCsMAFA (●) AND CsMAFA (■) WITH ONLY HP (BLUE) AND WITH THE H3PP:HP (ORANGE), UNDER 1,000 H OF CONTINUOUS ILLUMINATION AT 1 SUN UNDER A N <sub>2</sub> ATMOSPHERE USING WHITE LEDs AND MPP TRACKING. THE PEROVSKITE-H3PP DOPING RATIO IS THE OPTIMAL 1:500. THE INITIAL ABSOLUTE	

EFFICIENCIES ARE 19.1% AND 19.5% FOR THE REFERENCE AND H3PP-PSC (1:500) DEVICES, RESPECTIVELY. ....	54
FIGURE 2.8. THERMAL STABILITY ANALYSIS CARRIED OUT TO PSCs UNDER N <sub>2</sub> ATMOSPHERE AT 65 °C FOR 120 H. ....	55
FIGURE 2.9. A, OPTP ANALYSES OF PEROVSKITE FILMS ON SILICA, CARRIED OUT IN N <sub>2</sub> UNDER 4 SUNS FOR 10 H. AND B, PL MEASUREMENTS CARRIED OUT ON PEROVSKITE FILMS ON GLASS IN N <sub>2</sub> UNDER 100 SUNS FOR 500 S. ....	56
FIGURE 2.10. (A) FREQUENCY-DEPENDENT CAPACITANCE OF PSCs UNDER 1 SUN. (B) TEMPERATURE-DEPENDENT DARK CONDUCTIVITY OF HP THIN FILMS ON GLASS. ....	58
FIGURE 2.11. TOP-VIEW SEM IMAGE OF THE HP THIN FILM (LEFT) AND THE HP WITH THE H3PP ADDITIVE (RIGHT). ....	59
FIGURE 2.12. ADF-STEM MICROGRAPH (LATERAL VIEW) OF THE HP:H3PP 1:500 RATIO PSC (LEFT), AND THE CORRESPONDING EELS APPLIED FOR THE I, P AND I+P ANALYSIS IN THE ELEMENTAL MAPS (RIGHT). ....	60
FIGURE 2.13. XRD PATTERNS OF RbCsMAFA PEROVSKITE THIN FILMS DOPED WITH DIFFERENT CONCENTRATION OF H3PP. ....	60
FIGURE 2.14. SOLID-STATE NUCLEAR MAGNETIC RESONANCE (NMR). (A) NITROGEN-14 SOLID-STATE MAGIC ANGLE SPINNING (MAS) NMR SPECTRA (21.1 T, 298 K AND 5 KHz) OF (1) BULK MECHANOCHEMICAL A-FAPbI <sub>3</sub> AND (2) H3PP DOPED BULK MECHANOCHEMICAL A-FAPbI <sub>3</sub> (1:25 MOL/MOL). (B) PHOSPHORUS-31 MAS NMR SPECTRA AT 21.1 T OF (3) NEAT H3PP (298 K, 12 KHz MAS, ECHO-DETECTED) AND H3PP-DOPED BULK MECHANOCHEMICAL A-FAPbI <sub>3</sub> (1 :25 MOL/MOL): (4) AT 298 K AND 20 KHz MAS (ECHO-DETECTED) AND (5) AT 100 K AND 12 KHz MAS (1H-31P CP MAS), AND (6) H3PP-DOPED BULK MECHANOCHEMICAL RbCsMAFA PEROVSKITE (1:5 MOL/MOL) AT 298 K AND 20 KHz MAS (ECHO-DETECTED). ANALYSES CARRIED OUT TO THE HP AND THE HP: H3PP. (C) UV-VIS SPECTRA AND (D) PHOTOLUMINESCENCE SPECTRA. ....	61
FIGURE 2.15. FTIR ANALYSIS OF THE HP (ORANGE) AND HP:H3PP (BLUE), INDICATING THE PEAKS CORRESPONDING TO THE P=O STRETCHING MODE BETWEEN 1,220 AND 1,300 NM AND THE C=O STRETCHING MODE BETWEEN 1,600 AND 1,800 NM. ....	62
FIGURE 2.16. EXAMPLE OF ONE DOMINANT INTERACTION MODE, WHERE H3PP BINDS TO THE FAI-TERMINATED SURFACE OF FAPbI <sub>3</sub> , FORMING THREE HYDROGEN BONDS OF TWO DIFFERENT TYPES. (B) CHARGE REDISTRIBUTION AT THE H3PP/FAPbI <sub>3</sub> INTERFACE UPON THE ADSORPTION OF H3PP, WHERE CHARGE ACCUMULATION AND DEPLETION ARE INDICATED BY YELLOW AND CYAN, RESPECTIVELY. ....	64
FIGURE 2.17. XPS AND FTIR ANALYSIS OF THE HP AND THE H3PP:HP: (A) WITH DIFFERENT CONCENTRATION OF THE ADDITIVE H3PP XPS ANALYSIS (B) FTIR ANALYSES OF THE MAPbI <sub>3</sub> (MAPI), THE H3PP, THE PbI <sub>2</sub> AND THE COMBINATION OF H3PP WITH MAPI AND PbI <sub>2</sub> . XRD AND NMR ANALYSES OF THE HP AND THE HP:H3PP: (C) XRD ANALYSES OF THE PEROVSKITE SAMPLES WITH AND WITHOUT THE H3PP ADDITIVE, AFTER 1000 H UNDER CONTINUOUS LIGHT IRRADIATION OF 1 SUN, MPP TRACKING, N <sub>2</sub> ATMOSPHERE, RT. (D) LIQUID-STATE 1H NMR SPECTRA OF THE NEAT H3PP, THE RbPbI <sub>3</sub> :H3PP (R+H3PP), PEROVSKITE:H3PP (P+H3PP) MIXTURES AND THE NEAT PEROVSKITE (P). HERE PEROVSKITE IS RbCsMAFA. TO ENSURE THE DETECTION RESOLUTION, RbCsMAFA (OR RbPbI <sub>3</sub> ): H3PP= 2.5:1 WAS PREPARED IN 0.5 mL DMF-d <sub>7</sub> [45]. ....	65
FIGURE 2.18. (A–F) DIFFERENTIATED CAPACITANCE SPECTRA (A AND D), ARRHENIUS PLOTS OF THE INFLECTION FREQUENCIES DETERMINED FROM THE DERIVATIVE OF THE ADMITTANCE SPECTRA (B AND E) AND TRAP DENSITY OF STATES (TDOS) DEDUCED FROM TEMPERATURE-DEPENDENT C–F PLOTS (C AND F) FOR THE PEROVSKITE SOLAR CELLS WITH (D–F) AND WITHOUT H3PP (A–C).	

THE ACTIVATION ENERGY ( $E_a$ ) WAS EXTRACTED FOR EACH DEFECT AND SHOWN INSIDE THE FIGURES [54].....	67
FIGURE 3.1. DIAGRAM OF IMPROVEMENTS WHEN USING CARBON AS HOLE TRANSPORT LAYER IN PEROVSKITE SOLAR CELLS. ....	76
FIGURE 3.2. ALLOTROPES OF CARBON .....	77
FIGURE 3.3. SCHEMATICS OF (A) DEVICE AND (B) THE CORRESPONDING ENERGY LEVEL DIAGRAM (C) THE CROSS-SECTIONAL SEM IMAGE OF THE PEROVSKITE SOLAR CELL. (D) MAGNIFICATION IMAGE OF THE HIGHLIGHTED RECTANGLE AREA IN FIGURE (C).....	79
FIGURE 3.4. SEM IMAGES OF TOP-VIEW OF (A) PEROVSKITE FILM, (B) X-RAY DIFFRACTION PATTERNS OF PEROVSKITE FILMS BEFORE AND AFTER THERMAL TREATMENT.....	80
FIGURE 3.5. STATISTICS OF THE OPTOELECTRONIC PROPERTIES OF THE THERMALLY TREATED PSCs: A, FF B, $V_{OC}$ . C, $J_{SC}$ . AND D, EFFICIENCY. ....	82
FIGURE 3.6. (A) PCE MEASURED AT DIFFERENT TEMPERATURES FOR PSCs WITH AND WITHOUT TREATMENT AND (B) STABILITY TEST CARRIED OUT TO THE BEST DEVICE AT 45 °C IN THE DARK FOR 100 H. ....	83
FIGURE 3.7. (A) J-V CURVES ACQUIRED UNDER REVERSE POLARIZATION SCANNING OF THE BEST DEVICES WITHOUT HTL AND WITH HTL AFTER THERMAL TREATMENT AND (B) THERMAL STRESS TEST PERFORMED ON HTL-FREE PSC COMPARED TO DEVICE WITH HTL, STRUCTURES WITHOUT ENCAPSULATION.....	85
FIGURE 3.8. INCIDENT PHOTON-TO-ELECTRON CONVERSION EFFICIENCY (IPCE) SPECTRA OF C-PSCs. ....	86
FIGURE 3.9. STATISTICS OF THE OPTOELECTRONIC PROPERTIES OF PSCs WITH AND WITHOUT THERMALLY TREATED HTL: A, FF B, $V_{OC}$ . C, $J_{SC}$ . AND D, EFFICIENCY. ....	87
FIGURE 4.1. (A) STRUCTURE OF THE PZT AND (B) RHOMBOHEDRAL (R3C) STRUCTURE OF $\text{BiFeO}_3$ . .	96
FIGURE 4.2. PZT-BASED PEROVSKITE SOLAR CELL. (A) SCHEMATICS OF THE SOLAR CELLS; (B) IV CURVES IN REVERSE (BLACK LINE) AND FORWARD (GRAY LINE) OF THE SOLAR CELL RIGHT AFTER FABRICATION; (C) IV CURVES OF THE SOLAR CELL DURING POLING UNDER UV LIGHT AND (D) STABILITY. ....	97
FIGURE 4.3. RELATION BETWEEN $O_{vac}$ AND FERROELECTRICITY IN PZT. ....	98
FIGURE 4.4. X-RAY DIFFRACTION PATTERNS FOR BFO THIN FILMS SYNTHESIZED: A) AT DIFFERENT TEMPERATURES (INDICATED ABOVE EACH PATTERN IN UNITS OF CELSIUS); B) WITH DIFFERENT CONCENTRATION OF PRECURSOR SOLUTION. C) AFM IMAGE OF A BFO THIN FILM SURFACE. D) SURFACE SEM IMAGE OF A BFO THIN FILM. ....	100
FIGURE 4.5. A) I-V CURVES OF BFO IN CAPACITOR CONFIGURATION UNPOLED AT ROOM TEMPERATURE DENOTED BY THE RED PLOT. THE BLUE PLOT REPRESENTS THE I-V CURVE FOR THE SAME CAPACITOR AT 124K AND POLED WITH 24 V. B) I-V CURVES OF THE CAPACITOR CONFIGURATION OF BFO WITH PLATINUM UNDER ROOM TEMPERATURE AND ILLUMINATION WITH AND WITHOUT POLING, C) I-V CURVES OF THE SAME CONFIGURATION AT 127K UNDER ILLUMINATION. ....	102
FIGURE 4.6. A) EXPERIMENTAL CHARGE CURRENT HYSTERESIS J VS. E, LOOPS MEASURED IN THE FILM WITHOUT (BLACK) AND WITH ILLUMINATION (RED) AT 125 K. D) POLARIZATION HYSTERESIS P VS. E LOOPS CALCULATED BY THE INTEGRATION OF THE J-E LOOPS. C) TAUC PLOT SHOWING THE DIRECT BANDGAP OF BFO. D) CONDUCTIVITY CHANGES OF BFO THIN FILM UNDER AM 1.5G SOLAR IRRADIATION AND INCREASING POLING BIAS .....	104
FIGURE 4.7. XPS AND UPS OF BFO THIN FILMS ON FTO SUBSTRATE, A) SURVEY SCAN, B) BISMUTH PEAKS, C) IRON PEAKS, D) OXYGEN PEAK, E) WORK FUNCTION SPECTRA, F) VALENCE BAND SPECTRA. ....	105



FIGURE 4.8. A) SCHEMATIC DIAGRAM OF THE SOLAR CELL. B) CORRESPONDING STATISTICS FOR EACH CONCENTRATION FOR 7 DEVICES OF EACH CONCENTRATION. ....	106
FIGURE 4.9. CROSS SECTIONAL IMAGE OF BFO SOLAR CELLS HAVING VARIOUS CONCENTRATION AND THICKNESS. A) 0.25 M B) 0.20 M, c) 0.15 M AND D) 0.10 M.....	107
FIGURE 4.10. I-V POLING CURVES WITH INCREASING BIAS AND AM 1.5G IRRADIATION FOR DIFFERENT CONCENTRATIONS. A) 0.25 M, b) 0.20 M, c) 0.15 M AND D) 0.10 M.....	109
FIGURE 4.11. A) I-V CURVE FOR THE CHAMPION CELL. B) PERFORMANCE STATISTICS OF THE OPTIMISED BFO CONCENTRATION BATCH BEFORE AND AFTER POLING. ....	110
FIGURE 4.12. A) THE EQE AND INTEGRATED CURRENT FOR THE BEST DEVICE. B) A COMPARISON OF CURRENT DENSITY OF A DEVICE WHILE POLING ACQUIRED FROM I-V AND IPCE. ....	110
FIGURE 4.13. ENERGY LEVELS OF THE COMPONENTS DERIVED FROM UPS.....	112
FIGURE 4.14. A COMPARISON OF EXTRACTED CHARGE FOR A SOLAR CELL BEFORE AND AFTER POLING. ....	114
FIGURE 4.15. A) A COMPARISON OF CAPACITANCE VS. FREQUENCY CURVES UNDER LIGHT SWEEP OF A SOLAR CELL BEFORE AND AFTER POLING. B) NORMALISED TRANSIENT PHOTOCURRENT DECAYS BEFORE AND AFTER POLING. ....	115
FIGURE 4.16. BFO-BASED PSC. EVOLUTION OF IV CURVES DURING POLING DEPENDING ON THE HALIDE PEROVSKITE GRAIN SIZE (A) SMALL GRAIN AND (B) BIG GRAIN. ....	116
FIGURE 4.17. SEM IMAGE OF PZT FILM WITH SMALL (A) AND BIG (B) GRAIN SIZE, (c) STATISTICS OF INITIAL EFFICIENCY AND AFTER POLING DEPENDING ON GRAIN SIZE OF PEROVSKITE IN PSCs, (b) DIFFERENCE OF INITIAL EFFICIENCY AND END OF PSCs WITH DIFFERENT GRAIN SIZE. ....	117
FIGURE 4.18. HORIZONTAL CHARGE TRANSPORT IN LARGE PEROVSKITE GRAINS AND VERTICAL CHARGE TRANSPORT IN SMALL PEROVSKITE GRAINS. ....	118
FIGURE 4.19. AFM TOPOGRAPHIC IMAGES AND CONDUCTIVITY MAPS IMAGES MEASURED IN THE LIGHT FOR THE WITH SIZE OF (A-D) 360 NM, (F-H) 400 NM, (I-K) 500 NM AND (L-N)) 700 NM. MEASURED AREAS WERE 5 MM × 5 MM. ....	119
FIGURE 4.20. A) BIAS DEPENDENT OPERATION CHARACTERISTICS OF THE BFO SOLAR CELLS. B) STANDARD STABILITY TEST IN NITROGEN ATMOSPHERE UNDER AM 1.5 G IRRADIATION AT 45 °C WITHOUT UV FILTER. ....	120
FIGURE 4.21. THE PHOTOVOLTAIC PARAMETER EVOLUTION WITH INCREASING POLING BIAS AND INCREASING TIME, DEPICTING THE DEPENDENCY OF EFFICIENCY ON OTHER PARAMETERS. J <sub>sc</sub> (BLUE), V <sub>oc</sub> (GREEN), FF (BROWN), EFFICIENCY (RED).....	122
FIGURE 4.22. DEPENDENCY OF EFFICIENCY WITH RESPECT TO THE CONDITIONS EXPOSED UNDER AIR/N <sub>2</sub> OR WITH OR WITHOUT UV FILTER.....	123
FIGURE 5.1. GENERAL DEVICE FABRICATION SCHEME (PSCs).....	136
FIGURE 5.2. GENERAL DEVICE FABRICATION SCHEME (CARBON-BASED PSCs). ....	136
FIGURE 5.3. GENERAL DEVICE FABRICATION SCHEME (BFO-PSCs).....	136
FIGURE 5.4. IMAGE OF A SPIN COATER USED IN THIS THESIS.....	137
FIGURE 5.5. CARBON DEPOSITION ACCORDING TO THE DOCTOR-BLADE TECHNIQUE. ....	138
FIGURE 5.6. THERMAL EVAPORATION EQUIPMENT. ....	139
FIGURE 5.7. IMAGE OF THE SEM EQUIPMENT USED IN THIS THESIS.....	141
FIGURE 5.8. TWO-WAVE DIFFRACTION WITH CONSTRUCTIVE INTERFERENCE. ....	143
FIGURE 5.9. IMAGE OF THE X-RAY DIFFRACTION EQUIPMENT USED IN THIS THESIS. ....	144
FIGURE 5.10. IMAGE OF THE PAIOS EQUIPMENT USED IN THIS THESIS. ....	146
FIGURE 5.11. IMAGE OF THE UV-VISIBLE SPECTROPHOTOMETER USED IN THIS THESIS. ....	147
FIGURE 5.12. IMAGE OF THE FTIR EQUIPMENT USED IN THIS THESIS. ....	149
FIGURE 5.13. IMAGE OF THE PROFILOMETER USED IN THIS THESIS. ....	150
FIGURE 5.14. THE IPCE SETUP USED IN THIS THESIS. ....	151

FIGURE 5.15. XPS AND UPS EQUIPMENT. ....	154
FIGURE 5.16. A) OPEN CIRCUIT POTENTIAL ( $V_{OC}$ ) OF A CAPACITOR MEASURED AS A FUNCTION OF TIME WITH AND WITHOUT ILLUMINATION AT RT. B) SHORT-CIRCUITED PHOTOCURRENT DENSITY MEASURED IN THE FILM WITH AND WITHOUT ILLUMINATION AT RT. ....	154



# List of Tables

---

TABLE 2-1. MEASURED PLQE AND ESTIMATED QFLS OF HP THIN FILMS AND DEVICES WITH AND WITHOUT H3PP UNDER ONE SUN.....	51
TABLE 3-1. SUMMARY OF THE SOLAR CELL CONFIGURATION AND THE CORRESPONDING PHOTOVOLTAIC PARAMETERS OBTAINED FROM DIFFERENT GROUPS APPLYING THE DOCTOR BLADE TECHNIQUE FOR THE FABRICATION OF CARBON ELECTRODES IN PEROVSKITE SOLAR CELLS.....	76
TABLE 3-2. PHOTOVOLTAIC PARAMETERS DERIVED FROM J–V MEASUREMENTS OF DEVICES WITH AND WITHOUT TREATMENT. ....	83
TABLE 3-3. PHOTOVOLTAIC PARAMETERS DERIVED FROM J - V MEASUREMENTS OF DEVICES WITH AND WITHOUT HTL, MEASUREMENTS BEFORE TREATMENT. ....	84
TABLE 4-1. BIASING PROCESS USED FOR BIAS DEPENDENT STABILITY TEST.....	108



# Chapter 1: Introduction

---

## 1.1. Current status of photovoltaic devices

Global energy consumption has increased rapidly over the last half century and this trend is expected to continue in the years to come. The increase in energy consumption in recent years was stimulated using "cheap" fossil fuels and by the high speed of industrialization, mainly in North America and Europe. Also, in recent years the energy consumption of countries such as India and China have increased in a worrying way due to the growing population growth of these countries. This, coupled with the depletion of fossil resources in the near future and the effect of human activities on climate change, has prompted the development of new technologies for the production of energy from renewable sources. Figure 1.1 represents the percentages of the world energy consumption published by The 2021 Edition of the REN21 Renewables Global Status Report [1]. The total consumption of non-renewable energies is around 78.4%, well above the 19.3% reported for renewable sources. In contrast, solar energy played a small role in the overall energy scene (only 1.6%).

For the third year in a row, global energy-related carbon dioxide (CO<sub>2</sub>) emissions from fossil fuels and industry were nearly flat in 2020, increasing by just an estimated 0.2%, continuing to move away from the average growth trend 2.2% during the previous

decade [2]. Thus, there is a down trend for emissions growth, by amplifying renewable energy source availability and efficacy, and by decreasing coal use around the world.

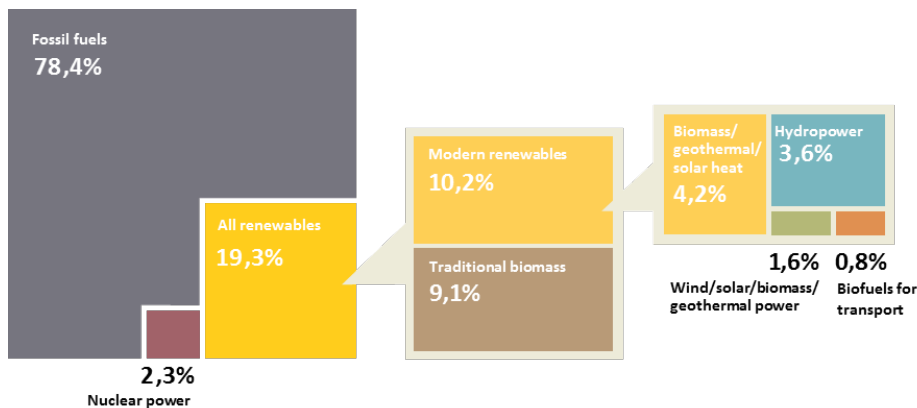


Figure 1.1. Estimated Renewable Share of Total Final Energy Consumption, 2020 [1].

Thanks to this generalized increase in the use of renewable energy, carbon emissions values are improving. However, its participation in total energy consumption has been moderate, despite the enormous growth produced by the renewable energy sector worldwide. More specifically, photovoltaic solar energy is in the first position above wind power and hydropower. On the other hand, we must not fail to consider other renewable energies, which, although they do not occupy a large place in the total percentage, represent other alternative sources (biomass) to the traditional source [3].

This increase in the use of renewable energy is in line with an increase in the generation of this type of energy, with the largest annual increase in renewable energy generation in 2020 being 261 gigawatts (GW) [1]. Total global renewable energy capacity

increased by almost 9% compared to 2015 [1]. Photovoltaic solar energy is postulated for the first time as the renewable energy source with greater additional energy capacity (net of decommissioned capacity) than any other generation technology [4][5]. In addition, it represents 47% of the total resources installed in 2020 for power generation globally, well above wind power or hydropower, which represent 34% and 15.5%, respectively [1].

Furthermore, of all renewable energy sources, solar energy is rapidly becoming the most viable alternative for energy production at the lowest cost, mainly because solar energy far outperforms any other renewable or non-renewable energy source in terms of energy availability. In addition, it is expected that in 2040, 32% of the total energy consumed by the planet will be provided solely by photovoltaic energy, which further reduces the threshold of economic viability of other renewable energy sources. This is due to the rapid reduction of unsubsidized costs generated from photovoltaic solar energy, which has enabled costs to compete with fossil fuels in most parts of the world [6].

## 1.2. Development and marketing

The photovoltaic effect was discovered by the French scientist Alexandre-Edmond Becquerel in the year 1839. Becquerel was experimenting with an electrolytic cell with platinum electrodes, one coated with silver chloride (AgCl) and the other with silver bromide (AgBr), both submerged in an acid solution, found that the current rose in one of the electrodes when it was exposed to the sun



[7], Other investigators reported materials with the same photovoltaic effect: in 1876 William Adams and Richard Day discovered that selenium with platinum have this effect; also, combining selenium and gold, as discovered by Charles Fritts in 1894; or even, copper-copper oxide thin films in Lead(II) sulfide and Thallium(I) sulfide ( $\text{PbS}$  and  $\text{Tl}_2\text{S}$ ). All these solar cells present a barrier to current flow and were thin film Schottky barrier devices [8][9][10]. The barrier to current flow is all the power contained in sunlight (about  $1000 \text{ W/m}^2$ ) falling on an ideal solar cell, and only 33.7% of sunlight could be turned into electricity ( $337 \text{ W/m}^2$ ).

Solar PV, also referred to as solar cells, has experienced three generations since the first practical silicon solar cells created by Bell Labs in 1954. The first generation of solar cells presents a relatively high efficiency with a high production cost, harsh preparation conditions, and serious environmental pollution. One example is monocrystalline and polycrystalline solar cells, in which an electron-hole pair is generated through the  $p$ - $n$  junction of a doped silicon-based semiconductor. The commercial market is dominated by this generation. On the other hand, there are thin film solar cells based on amorphous silicon, CdTe and Cu (In, Ga)Se<sub>2</sub> (CIGS), known as second generation cells. These have a conversion efficiency much lower energy compared to the first generation, they are much cheaper to produce, and less time is required for production process. They are mainly used for photovoltaic power plants, integrated into buildings or smaller solar energy systems. The third-generation solar cells are any cell that is not grouped in the first or second generation; they use a wide variety of technologies and materials and are not limited by the Shockley-Queisser limit. They are devices

based on inorganic, organic and polymeric materials. These allow reasonable efficiencies of energy conversion; also, its production cost is lower due to the fabrication methods and the costs of the materials. Most of them have not yet been commercially applied and are still in the research or development stage. The most recent technology discovered inside the third generation PV has been perovskite solar cells (PSC) that will be explained more in detail in subsequently section. Figure 1.2 shows the representative solar cells of the three generations.

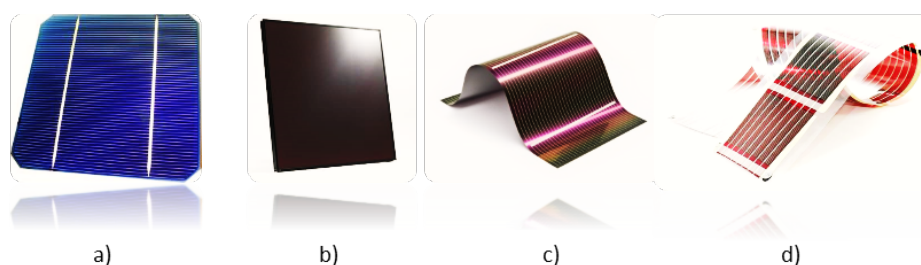


*Figure 1.2. a) Monocrystalline silicon solar cell [11], b) Thin film CdTe solar cell [12], c) Flexible CIGS thin-film solar cell [13] and d) Polymer solar cell [14].*

Currently there is a wide variety of technologies that allow the development of photovoltaic solar energy from different fields. A summary of the best certified solar cell efficiencies, published by the National Renewable Energy Laboratory (NREL), is shown in Figure 1.3. These technologies can be classified as first, second or third generation technologies. In the first generation is the silicon technology, both monocrystalline and polycrystalline silicon. In the second generation is the thin-film technology, whose devices can be made of cadmium telluride, copper-indium-gallium selenide, or amorphous silicon. Lastly, in the third generation are tandem solar

cells, cells from group III-V of the periodic table, organic cells, etc. Currently, the efficiency of PSCs is at 25.8 % is very close to the one reported for Silicon solar cells at 26 %. The graph shows the rapid evolution of energy conversion efficiency observed for PSCs in recent years.

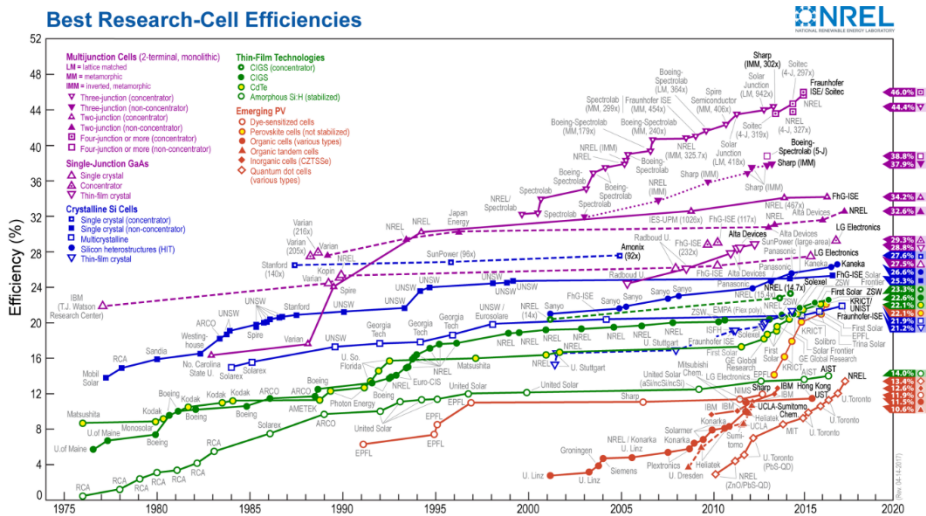


Figure 1.3. Best Research-Cell Efficiencies [15].

### 1.3. Configurations of solar cells

According to the photovoltaic effect of the  $p$ - $n$  junction, different schemes for the representative solar cells of the three generation are implemented, as shown in Figure 1.4. Silicon PV solar cells are the most widely used solar cells in solar panels that are commercially available, the  $p$ - $n$  junction of crystal silicon solar cells is  $p$ -type Si/ $n$ -type Si homojunction, (See Figure 1.4a), the typical CdTe thin film PV device, as shown Figure 1.4b. In this device design, the films are deposited on a glass substrate, which allows sunlight to enter. This

sunlight passes through the glass and generates electric current and voltage in the lower films. The best efficiencies presented for this type of CdTe devices is more than 22%. The typical CIGS thin film photovoltaic device (See Figure 1.4c). For this design, the layers that make up the device can vary depending on the purpose, they can be deposited on a glass, metal, or polymer substrate. Light from the sun enters the uppermost layer (transparent conductive oxide) of the device and produces electric current and voltage in the lower layers. Figure 1.4d shows the typical perovskite solar cell that has a layer of perovskite, most commonly a lead-based or tin-halide-based organic-inorganic hybrid material, as the active light-harvesting layer.

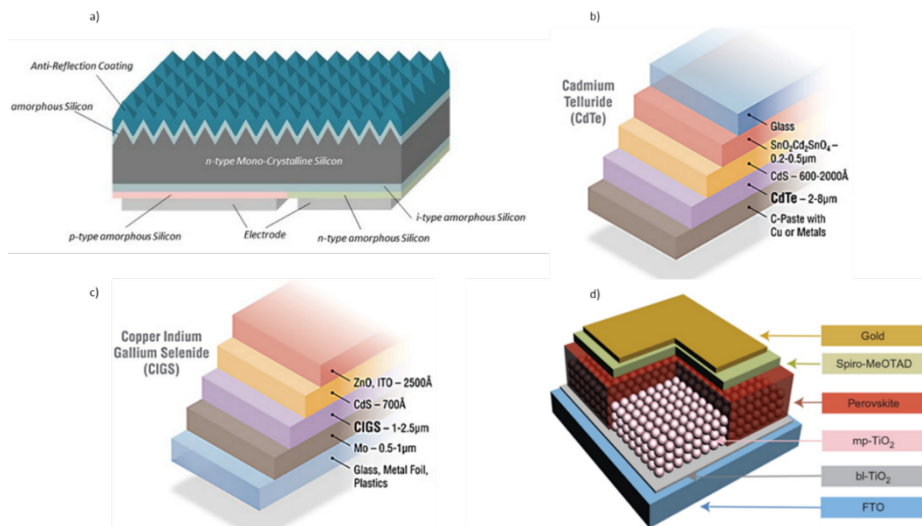


Figure 1.4. Typical schemes of different generations of solar cells, (a) Crystalline silicon[16], (b) CdTe thin film, (c) CIGS thin film[11] and (d) Perovskite[17]

## 1.4. PSC Principles

Perovskite materials are easy to find and abundant, they have a low energy of formation, therefore they are easy to deposit with different techniques. Halide perovskite solar cells (PSCs) have demonstrated high conversion efficiencies of over 25% in a short time, making them an attractive technology for the energy sector. The rapid progress and reported good efficiencies comparable with other thin-film photovoltaic (PV) systems has led to quickly becoming a breakthrough research area. Figure 1.5 Figure we appreciate the rapid evolution of perovskite solar cells in the last 11 years. All These features make PSCs potential competitors of well-established technologies such as those based on silicon. In the following subsections: we will give an overview of the generalities involving the  $\text{ABX}_3$  perovskite materials and solar cells.

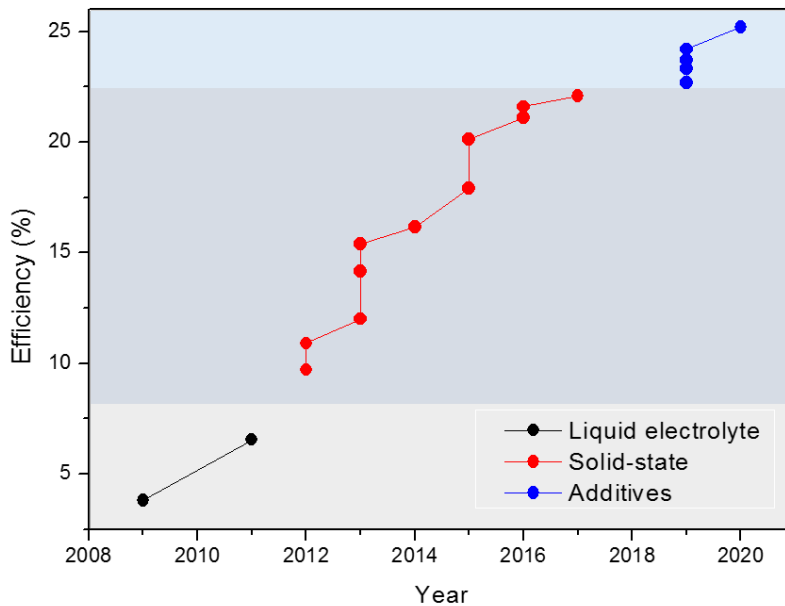
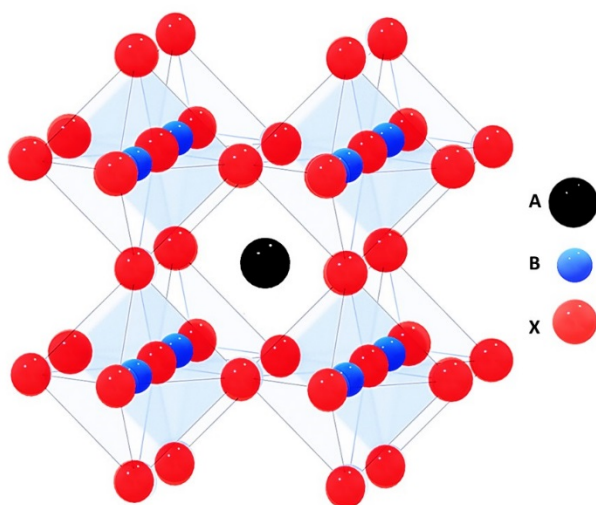


Figure 1.5. The best efficiencies of perovskite solar cells [18].

#### 1.4.1. Perovskite crystal structure

A perovskite is a crystal with a cubic cell and chemical formula  $ABX_3$  where A and B are cations of different sizes that fit in the corners of the cube and in the center of it, respectively; while X is an anion located on the faces. The ion A may be an alkaline lanthanide, B is typically a transition metal, and X is a halogen or oxygen. Many perovskites present interesting properties such as piezoelectricity and ferroelectricity, where there is the presence of a spontaneous polarization due to the displacement of the cation B; they can also present ferromagnetism, superconductivity, and photovoltaic effect. This last one, particularly important in perovskites. These materials have a band gap that allows them to absorb light from the visible part of the spectrum, in addition to having a broad absorption spectrum and a low recombination rate, among other properties, which makes them ideal for manufacturing photovoltaic cells. In recent years, many research efforts have been made to replace organic or inorganic cations to improve performance and stability. A typical perovskite crystal unit cell structure is shown in Figure 1.6 [19] [20].



*Figure 1.6. The crystal structure of the perovskite.*

#### 1.4.2. Optical properties

The solar cell operating principle is simple and starts with the light absorption by the material. Here, the material is a limiting step for solar to energy conversion, and compared to conventional devices materials, the great advantages of the perovskites are the high absorption coefficient and the ease of synchronization in their band gap. The organic or inorganic halide perovskites materials are semiconductors in which the conduction band (CB) originates by combining anti-bonding p orbitals ( $\pi^*$ ) of B cations and anti-bonding s orbitals ( $s^*$ ) of X anions, while the valence band (VB) is determined by the hybridization between  $s^*$  of cations B and  $\pi^*$  of anions X [25].

Solar cells that use this semiconductor material as a light-absorbing layer have attractive features such as: they have good photoelectric

properties, lower exciton binding energy, and high optical absorption coefficient [26]. Broad absorbance spectrum since they absorb in most of the visible and near-infrared spectrum of sunlight. High intrinsic mobility of charges: the electric charge can be transported by the electrons in the conduction band or by the holes left in the valence band (electrical current of electrons or holes) by making light fall on them [27]. High polarity: which represents the separation of electrical charges in the same molecule. High thermodynamic stability compared to organic dyes or coordination complexes [28]. These materials have a high dielectric constant, both electrons and holes are efficiently transmitted and congregated [29][30][31][32]. Perovskite material possesses a tuneable band-gap of 1.5 to 3.6 eV [33].

#### 1.4.3. Electronic properties and charge recombination

Photoexcited charge-carrier lifetime is an essential metric in a solar cell device, and the longer carrier lifetimes are directly correlated with higher energy conversion efficiency in the solar cells. The complete and precise knowledge of carriers recombination mechanisms is essential to understand its excellent performance, and further enhance efficiency [34].

The efficiency is determined by carriers' recombination, taking into account a quantum mechanics perspective. For Shockley-Read-Hall (SRH) recombination, both the electrons and the holes recombine through defects deep in the band gap, and the energy released by electron-hole recombination is dispersed into photons (Figure 1.7a).



For the radiative recombination, both electrons and holes directly recombine and emit photons (Figure 1.7b), and this is the light-emitting mechanism of LEDs. Two types of processes compose the Auger recombination. Firstly, when an electron and a hole recombine, and the excess of energy and momentum can be captured by a third carrier, which gets promoted to a higher state. In the second step, If the third carrier is an electron, the Auger recombination is an electron–electron–hole (eeh) process (Figure 1.7c), If is not an electron it is called a hole–hole–electron (hhe) process (Figure 1.7d). Being able to understand these processes helps us understand the unique behaviour of these materials, as well as generate more general design rules for high-performance perovskites [35].

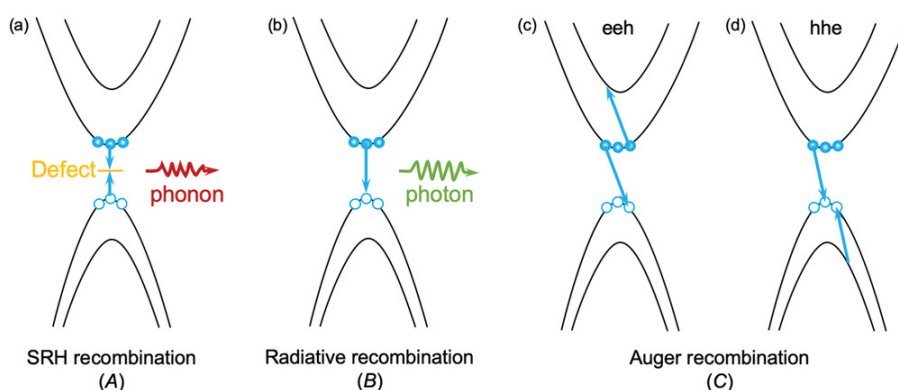
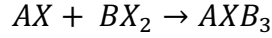


Figure 1.7. Schematic illustration of different recombination processes [35].

#### 1.4.4. Chemistry of metal halide perovskites

Metal halide perovskites are a class of semiconductor materials. In the case of perovskite solar cells, the most widely used materials are those with a generalized chemical formula  $ABX_3$  (Figure 1.6). In

general, metal halide perovskites are synthesized by a simple chemical reaction between organic ammonium ( $\text{NH}_4^+$ )/Cesium (Cs) halide and Lead (Pb)/Tin (Sn) halide [36]:



Especially, these materials can be easily processed into thin films using various low-temperature methods, and their microstructures can be highly adaptable to multiple scales. Such versatile fabrication makes it possible to obtain desired perovskite materials for researchers in almost all every field, including physics, chemistry, and materials science. In addition, there is a huge composition space in this material family, leading to versatile crystal structures Figure 1.8 and (opto) electronic properties. According to the morphology of the metal halide perovskites we can classify it in crystalline films, and single crystals. And the fabrication methods of perovskite films can vary from blade coating, vacuum thermal evaporation, spin-coating, pulsed laser deposition, spray coating, etc. [37].

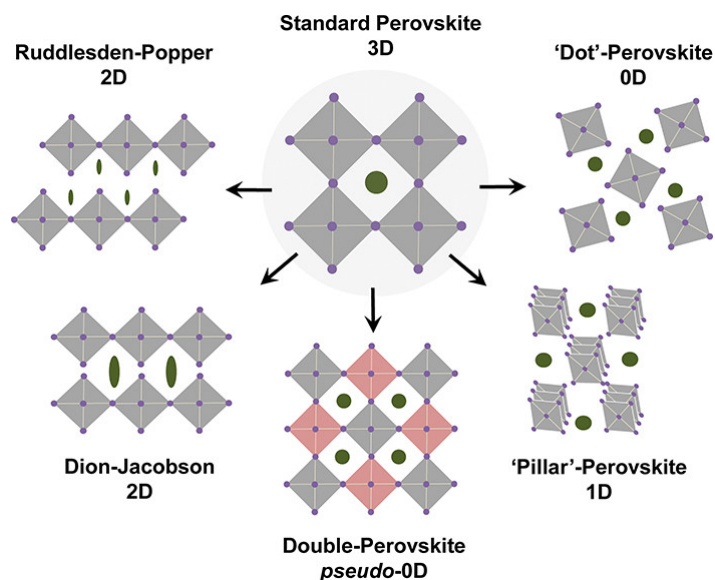


Figure 1.8. Schematic crystal structures of the broad family of hybrid perovskites [37].

#### 1.4.5. Halide Perovskite Solar Cells

Research has already shown experimental-scale perovskite solar devices to perform as well as commercial solar cells such as silicon. Perovskite cells have the potential to dominate the solar energy sector. This type of perovskite solar cell has the potential to be produced simply from a thin film, by simple deposition techniques. Figure 1.9 shows the band diagram of a typical perovskite solar cell. This cell is made up of selective contacts that allow charge separation to be carried out, which is why an electron transport layer (ETL) and another hole transport layer (HTL) are necessary. This complex solar device is composed of a multilayer structure, in which the correct operation is based on interfaces or "junctions" between semiconductor materials. The most common configuration proposed for perovskite solar cells is made up of thin layers: a glass

coated with fluorine-doped tin oxide (FTO) that will serve as the substrate. A compact layer of selective contact of electrons, usually TiO<sub>2</sub> and mesoporous layer of the same semiconductor. A layer of perovskite (active layer). A layer of a hole-carrying material, typically Spiro-OMeTAD. A conductive electrical contact, such as gold. According to this structure, light penetrates through the FTO, with the active layer of perovskite being responsible for absorbing the incident light. The photons absorbed by the active layer of perovskite will generate an electron-hole pair in the material. The generated electrons are injected into the mesoporous layer and pass to the external circuit until they reach the gold contact. On the other hand, the holes are directed towards the HTL and diffuse by electrical conduction to the gold. Only with the use of selective contacts will an electric current be generated by favouring an efficient separation of the charges that minimize recombination processes [38][39][40]. For this process to be adequate, it is necessary that there is an adequate alignment of the bands of the different layers so that an efficient load extraction occurs.

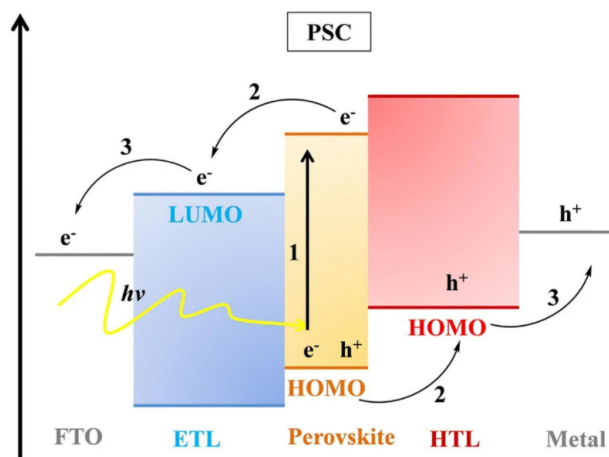


Figure 1.9. Band diagram and operation principle of perovskite solar cell [39].

#### 1.4.6. Stability of metal halide perovskites

Perovskite solar cells have shown competitive efficiencies with potential for higher performance, this is very promising considering that the Shockley-Queisser limit predicts the maximum theoretical efficiency that a solar cell employing a single p-n junction can achieve is 33.7% with a band gap of 1.34 eV. These characteristics have meant that perovskites have become widely studied. However, despite all its good qualities, the commercialization of solar cells based on this type of perovskites is mainly limited by two obstacles. The first of these is the chemical instability of this family of materials, which tend to decompose easily in ambient conditions, especially in the presence of air, humidity and/or light (Figure 1.10). Considering the perovskite  $\text{MAPbI}_3$ , one of the most used, the effect of humidity initially triggers the decomposition of the crystal into its precursors: lead and methylammonium iodides, finally obtaining, with the help of atmospheric  $\text{O}_2$ , methylamine and molecular iodine.

In addition, the entire process is favoured by the intervention of UV radiation. The second, directly related to the previous one, is the high toxicity of lead and its halogenated derivatives, such as  $\text{PbI}_2$ , which can be released as a result of its degradation. Its solubility product is very small, on the order of  $10^{-8}$ , many orders of magnitude higher than that of other compounds commonly used in solar cells and containing heavy metals [41].

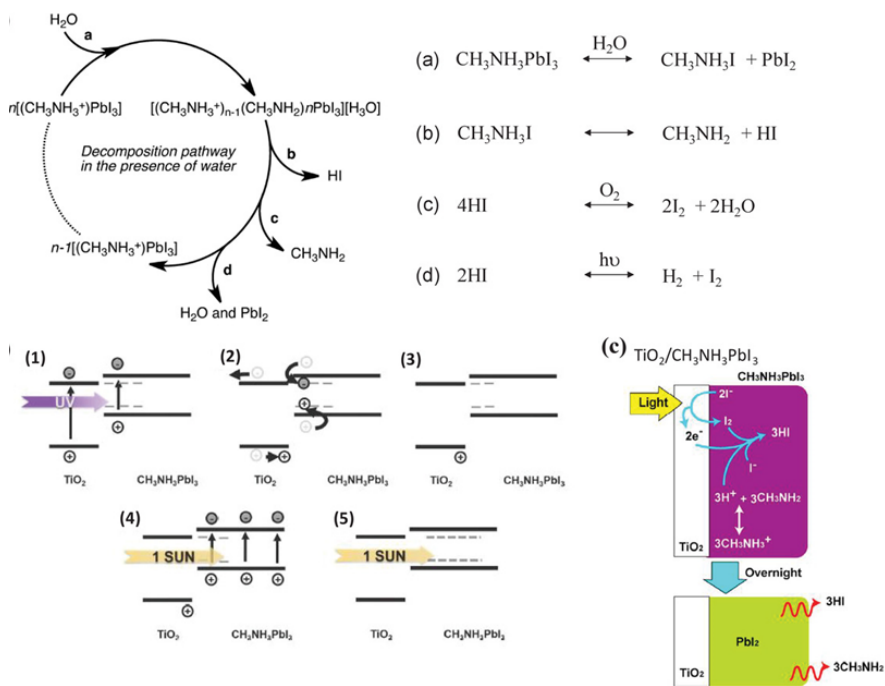


Figure 1.10. Degradation pathways of the perovskite material [41].

## 1.5. Objectives of the thesis

### 1.5.1. General objectives

The general objective of this work is the study of different approaches to improve the power conversion efficiency (PCE) and

the stability of PSCs. Three different approaches have been selected: (a) application of additives, (b) development of carbon-based electrodes and (c) use of novel ferroelectric oxides as ETLs.

#### 1.5.2. Specific objectives

The specific objectives are based on the three different approaches selected:

##### **Additive Engineering.**

The effect of additive engineering on the halide perovskite (HP) absorber and its effect on the stability of complete perovskite solar cells were carried out. The main goal is to understand the relation between defect passivation of the additive and the PSC efficiency and stability. Surface functionalization was studied using small molecules and its effect on the stability and lifetime of solar cells perovskite.

##### **Carbon based PSCs.**

Given that the most stable PSCs are those based on C-based PSCs an analysis and optimization of these types of solar cells and their long-term stability were carried out. The Au electrode was replaced by carbon-based materials to fabricate C-based PSCs (C-PSCs). Complete PSC devices were then fabricated in normal configuration and as hole transport-free carbon-based PSC applying low-cost techniques such as spin coating or doctor blade. Additionally, the doctor blade technique allowed the fabrication of PSCs on almost any substrate and at large scale. The aim is to analyse the

hygroscopic effect that carbon-based electrodes have on the stability of PSCs.

### **Ferroelectric Oxides as ETL.**

We carried out a deep study of the application of innovative oxides such as ferroelectric oxides as part of the ETL in PSCs. Following the initial results on the application of the PZT ferroelectric oxide in PSCs by the research group, in this section we developed novel Pb-free BiFeO<sub>3</sub> ferroelectric materials made by solution processing and analyse their efficiency and stability under different atmospheres. In all cases, complete solar cell characterization was carried out under calibrated sun simulator under ambient air conditions. The degradation studies of the complete PSCs following the ISOS-protocols under continuous illumination in ambient conditions is also part of this study.

## **1.6. Scope of the thesis work**

This thesis is organized into five different chapters. Each chapter presents a brief introduction and review of the literature, followed by the experimental results. Each chapter ends with a brief summary of the conclusions of the work and the corresponding references. The content of each chapter is described below:

**Chapter 1:** This chapter presents a current introduction that provides a brief overview of photovoltaic technology and its role as a viable option for generating electricity.



**Chapter 2:** This chapter is focused on additive engineering, studying, and optimizing its effects on photovoltaic performance and PSC stability, mainly on the perovskite active layer passivation technique.

**Chapter 3:** This chapter focuses on carbon-based PSCs without hole transport materials (C-PSC), these devices have the best stability since the carbon is resistant to water and humidity and inert to the migration of ions, a problem that is generated at the interface of the perovskite and the metal electrodes.

**Chapter 4:** Ferroelectric oxides are applied as electron transport materials in perovskite solar cells. In this chapter we discuss on the working principle and characterization of PSCs. We analyse how this work could be a cutting-edge technology for the development of PSCs.

**Chapter 5:** Details of the experimental process and characterization of perovskite solar cells, as well as a brief description of the equipment used in this work.

**Chapter 6:** This final chapter encompass a brief discussion of the results and conclusions of this thesis work.

## 1.7. References

- [1] "RENEWABLES 2017 GLOBAL STATUS REPORT."
- [2] C. Le Quéré *et al.*, "Global Carbon Budget 2016," *Earth Syst. Sci. Data*, vol. 8, no. 2, pp. 605–649, 2016.
- [3] "Key world energy statistics," 2017.
- [4] IAEA, "PRIS - Home," 2016. [Online]. Available: <https://www.iaea.org/pris/>. [Accessed: 03-May-2018].
- [5] "Frankfurt School-UNEP Centre/BNEF. 2016. Global Trends in Renewable Energy Investment 2016, <http://www.fs-unep-centre.org> (Frankfurt am Main)."
- [6] H. Larsen and L. S. Petersen, *Risø Energy Report 9*, vol. 1469, no. November. 2010.
- [7] M. A. Green, "Photovoltaic principles," in *Physica E: Low-Dimensional Systems and Nanostructures*, 2002, vol. 14, no. 1–2, pp. 11–17.
- [8] J. Nelson, *The Physics of Solar Cells*. PUBLISHED BY IMPERIAL COLLEGE PRESS AND DISTRIBUTED BY WORLD SCIENTIFIC PUBLISHING CO., 2003.
- [9] W. Shockley and H. J. Queisser, "Detailed Balance Limit of Efficiency of  $p$ - $n$  Junction Solar Cells," *J. Appl. Phys.*, vol. 32, no. 3, pp. 510–519, Mar. 1961.
- [10] S. Rühle, "Tabulated values of the Shockley-Queisser limit for single junction solar cells," *Sol. Energy*, vol. 130, pp. 139–147, 2016.
- [11] A. Mohammad Bagher, "Types of Solar Cells and Application," *Am. J. Opt. Photonics*, vol. 3, no. 5, p. 94, Aug. 2015.
- [12] "Optimum Sun\_Solar bracket,Solar Home Kit,Solar Street Light." [Online]. Available: <http://www.optimumsun.com/>. [Accessed: 16-Aug-2018].
- [13] "Innovation: Thin Film Solar Cells at MX2016 - MaterialDistrict." [Online]. Available: <https://materialdistrict.com/article/innovation-thin-film-solar-cells-at-mx2016/>. [Accessed: 16-Aug-2018].
- [14] "Danish company InfinityPV flexible polymer solar cell-based suitable for building integrated photovoltaics (BIPV) – Match Observatory." [Online]. Available: <http://matchobservatory.eu/?p=946>. [Accessed: 11-Nov-2018].
- [15] Nrel, "National Renewable Energy Laboratory (NREL) Home Page," 2006. [Online]. Available: <https://www.nrel.gov/>.

- [Accessed: 28-Aug-2018].
- [16] "Sharp Develops 6-Inch-Size Mono-Crystalline Silicon Solar Cell with World's Highest Full Size Conversion Efficiency of 25.09%." [Online]. Available: <http://www.sharp-world.com/corporate/news/180327.html>. [Accessed: 21-Jan-2019].
  - [17] X. Li *et al.*, "Improved performance and stability of perovskite solar cells by crystal crosslinking with alkylphosphonic acid  $\omega$ -ammonium chlorides," *Nat. Chem.*, vol. 7, no. 9, pp. 703–711, Sep. 2015.
  - [18] C. Pereyra, H. Xie, and M. Lira-Cantu, "Additive engineering for stable halide perovskite solar cells," *Journal of Energy Chemistry*, vol. 60. Elsevier B.V., pp. 599–634, 01-Sep-2021.
  - [19] Q. Luo, "Applications in photovoltaics," in *Solution Processed Metal Oxide Thin Films for Electronic Applications*, Elsevier, 2020, pp. 109–140.
  - [20] M. V. Khenkin *et al.*, "Consensus statement for stability assessment and reporting for perovskite photovoltaics based on ISOS procedures," *Nat. Energy*, vol. 5, no. 1, pp. 35–49, Jan. 2020.
  - [21] C. Ran, J. Xu, W. Gao, C. Huang, and S. Dou, "Defects in metal triiodide perovskite materials towards high-performance solar cells: Origin, impact, characterization, and engineering," *Chemical Society Reviews*, vol. 47, no. 12. Royal Society of Chemistry, pp. 4581–4610, 21-Jun-2018.
  - [22] A. Rajagopal, K. Yao, and A. K. Y. Jen, "Toward Perovskite Solar Cell Commercialization: A Perspective and Research Roadmap Based on Interfacial Engineering," *Advanced Materials*, vol. 30, no. 32. Wiley-VCH Verlag, 09-Aug-2018.
  - [23] H. Zhang, M. K. Nazeeruddin, and W. C. H. Choy, "Perovskite Photovoltaics: The Significant Role of Ligands in Film Formation, Passivation, and Stability," *Advanced Materials*, vol. 31, no. 8. Wiley-VCH Verlag, 22-Feb-2019.
  - [24] J. W. Lee and N. G. Park, "Chemical Approaches for Stabilizing Perovskite Solar Cells," *Advanced Energy Materials*. 2020.
  - [25] A. Walsh, "Principles of Chemical Bonding and Band Gap Engineering in Hybrid Organic–Inorganic Halide Perovskites," *J. Phys. Chem. C*, vol. 119, no. 11, pp. 5755–5760, Mar. 2015.
  - [26] S. Sun *et al.*, "The origin of high efficiency in low-temperature solution-processable bilayer organometal halide hybrid solar cells," *Energy Environ. Sci.*, vol. 7, no. 1, pp. 399–407, Dec.

- 2013.
- [27] C. C. Stoumpos, C. D. Malliakas, and M. G. Kanatzidis, "Semiconducting Tin and Lead Iodide Perovskites with Organic Cations: Phase Transitions, High Mobilities, and Near-Infrared Photoluminescent Properties," *Inorg. Chem.*, vol. 52, no. 15, pp. 9019–9038, Aug. 2013.
  - [28] T. Baikie *et al.*, "Synthesis and crystal chemistry of the hybrid perovskite (CH<sub>3</sub>NH<sub>3</sub>)PbI<sub>3</sub> for solid-state sensitised solar cell applications," *J. Mater. Chem. A*, vol. 1, no. 18, pp. 5628–5641, Apr. 2013.
  - [29] M. A. Green, A. Ho-Baillie, and H. J. Snaith, "The emergence of perovskite solar cells," *Nat. Photonics* 2014 87, vol. 8, no. 7, pp. 506–514, Jun. 2014.
  - [30] S. P. Singh and P. Nagarjuna, "Organometal halide perovskites as useful materials in sensitized solar cells," *Dalt. Trans.*, vol. 43, no. 14, pp. 5247–5251, Mar. 2014.
  - [31] M. Luan, J. Song, X. Wei, F. Chen, and J. Liu, "Controllable growth of bulk cubic-phase CH<sub>3</sub>NH<sub>3</sub>PbI<sub>3</sub> single crystal with exciting room-temperature stability," *CrystEngComm*, vol. 18, no. 28, pp. 5257–5261, Jul. 2016.
  - [32] C. I, L. B, H. J, C. RP, and K. MG, "All-solid-state dye-sensitized solar cells with high efficiency," *Nature*, vol. 485, no. 7399, pp. 486–489, May 2012.
  - [33] M. Saliba, J.-P. Correa-Baena, M. Grätzel, A. Hagfeldt, and A. Abate, "Perovskite Solar Cells: From the Atomic Level to Film Quality and Device Performance," *Angew. Chemie Int. Ed.*, vol. 57, no. 10, pp. 2554–2569, Mar. 2018.
  - [34] D. W. deQuilettes *et al.*, "Charge-Carrier Recombination in Halide Perovskites," *Chem. Rev.*, vol. 119, no. 20, pp. 11007–11019, Oct. 2019.
  - [35] X. Zhang, J.-X. Shen, and C. G. Van de Walle, "First-Principles Simulation of Carrier Recombination Mechanisms in Halide Perovskites," *Adv. Energy Mater.*, vol. 10, no. 13, p. 1902830, Apr. 2020.
  - [36] H. Dong, C. Zhang, X. Liu, J. Yao, and Y. S. Zhao, "Materials chemistry and engineering in metal halide perovskite lasers," *Chem. Soc. Rev.*, vol. 49, no. 3, pp. 951–982, Feb. 2020.
  - [37] Y. Zhou and W. Chen, "Hybrid organic-inorganic halide perovskites," *J. Appl. Phys*, vol. 128, p. 200401, 2020.
  - [38] A. K. Jena, A. Kulkarni, and T. Miyasaka, "Halide Perovskite Photovoltaics: Background, Status, and Future Prospects,"

- Chem. Rev.*, vol. 119, no. 5, pp. 3036–3103, Mar. 2019.
- [39] I. Hussain, H. P. Tran, J. Jaksik, J. Moore, N. Islam, and M. J. Uddin, “Functional materials, device architecture, and flexibility of perovskite solar cell,” *Emergent Mater.* 2018 13, vol. 1, no. 3, pp. 133–154, Nov. 2018.
- [40] M. A. Green and A. Ho-Baillie, “Perovskite Solar Cells: The Birth of a New Era in Photovoltaics,” *ACS Energy Lett.*, vol. 2, no. 4, pp. 822–830, Apr. 2017.
- [41] H. D. Pham, T. C.-J. Yang, S. M. Jain, G. J. Wilson, and P. Sonar, “Development of Dopant-Free Organic Hole Transporting Materials for Perovskite Solar Cells,” *Adv. Energy Mater.*, vol. 10, no. 13, p. 1903326, Apr. 2020.

# Chapter 2: Additive Engineering in Halide Perovskite Solar Cells

---

## 2.1. Introduction

Third-generation halide perovskite solar cells (PSCs) have shown rapid growth in just a few years, presenting an efficiency of over 25%, with an attractive future. Perovskite's halide solar cells (PSCs) are of great interest due to their advantages, such as their high efficiency, fabrication materials, ease of adjustment, great optical properties, and the possibility of fabrication at low temperatures. However, some issues related to PSCs need to be considered for the technology to be competitive with the commercial one's. The main problem for scale production and commercialization is the low long-term stability of PSCs. There are some strategies to improve PSCs stability, in this chapter, we pretend to improve stability with the additive engineering.

The additive engineering is an effective pathway for the enhancement of device lifetime where the main role of additives was the modulation of morphology of the perovskite films, the stabilization of formamidinium (FA) and cesium (Cs)-based perovskites phases, the tunability of the energy levels, the suppression of the non-radiative recombination through defect

passivation, reduction or elimination of hysteresis, and the enhancement of operational stability of PSCs.

Different types of additives can be applied to PSCs, like salts, molecules, polymers, or nanoparticles, among others [1][2][3][4][5][6][7]. According to the additive type, the ratio and the methodology used for applying the additive on the perovskite solar cells should be adapted. For example, additives can be introduced before layer preparation; others are introduced into the film during post-processing. The additive may disappear and in others remain after fabrication, in this case, the remaining additives can be found within the halide perovskite grains, others at boundaries and interfaces and many others at surfaces [7].

In general, the additives used are selected based on the functional groups that follow the sequence of amino, carbonyl, thio, carboxyl, hydroxyl and cyano groups [8]. This functional groups can act in ion immobilization, passivation, or grain boundaries growth among others [8][9][10][11]. The chemical shift trend for an additive varies considerably depending on the functional group participating in the bonding with the perovskite. In PSCs, the most used additives incorporate functional groups such as  $-\text{COOH}$  or  $-\text{NH}_3^+$ , meanwhile the  $-\text{PO}(\text{OH})_2$  group are the less used in additive engineering [12][13][14][15]. The characteristic of the phosphonic acid derivative has been related to a stronger hydrogen donor character, which plays an important role in charge injection [17]. For example, Brown et al. studied the benefits of  $-\text{PO}(\text{OH})_2$  and  $-\text{COOH}$  anchoring agents in solar cells: using  $-\text{PO}(\text{OH})_2$  to have better surface bonding stability, where they used carboxylic acids to increase electrode injection [18]. This reinforces the idea that the chemical bonds

between the perovskite and the additive have an important role in regulating the activation energy of ion migration, which could determine the long-term stability in perovskite solar devices [19].

It is also important to highlight that the incorporation of additives in the halide perovskite film is a procedure that can be used effectively to passivate defects, advancing not only the efficiency, but also increasing the stability of the PSCs [20][21][22][23]. However, the stability results are not always favourable, as they are not capable of showing less than 10% degradation after 1000 hours of operation with continuous lighting, in concordance with the ISOS protocols [24].

The importance of additive engineering approach is not simple and requires multiple factors as reviewed [25][26][13][24][27][28][29]. Despite all these advances in research, understanding these perovskite/additive binding processes—the relationship between defective passivation, efficiency, non-radiative recombination, and stability in perovskite solar cells—remain poorly understood.

## 2.2. Results

### 2.2.1. Additive selection

In the present work, we study the family of phosphonopropionic acid additives and analyse the effect that the two anchoring groups; phosphonate [ $-\text{PO}(\text{OH})_2$ ] and carboxylate [ $-\text{COOH}$ ], have on the functioning of PSCs. These two functional groups were selected due to their optimal interaction with the halide perovskite [17][30][31][32]. This family of molecules can be found in a variety



of chain lengths and shape: Phosphonoacetic acid (H2pp), 3-Phosphonopropionic acid (H3pp), 6-Phosphonopropionic acid (H6pp) and 16-Phosphonopropionic acid (H16pp) as displayed in Figure 2.1. For comparison purposes, we also include the organic molecule, 4-Methoxybenzylphosphonic acid (4-Methox), with  $\text{PO(OH)}_2$  and (methodology), the additives were introduced into the perovskite precursor solutions to fabricate complete solar cells with the configuration FTO/c-TiO<sub>2</sub>/m-TiO<sub>2</sub>/HP/Spiro-OMeTAD/Au. The halide perovskite was based on the multication perovskite absorber with the nominal formula  $\text{Rb}_{0.05}\text{Cs}_{0.05}\text{MA}_{0.15}\text{FA}_{0.75}\text{Pb}_{1.05}(\text{I}_{0.95}\text{Br}_{0.05})_3$  (RbCsMAFA). The perovskite precursor solutions were prepared by simply dissolving the corresponding additive in the perovskite precursor solution with different molar ratios. Figure 2.1 shows the photovoltaic response obtained from the solar cells with the different additive. The PSC without additive (labelled as HP) was used as a reference. We observed that, in all cases, the PCEs obtained were below those values found for the reference RbCsMAFA device without any additive.

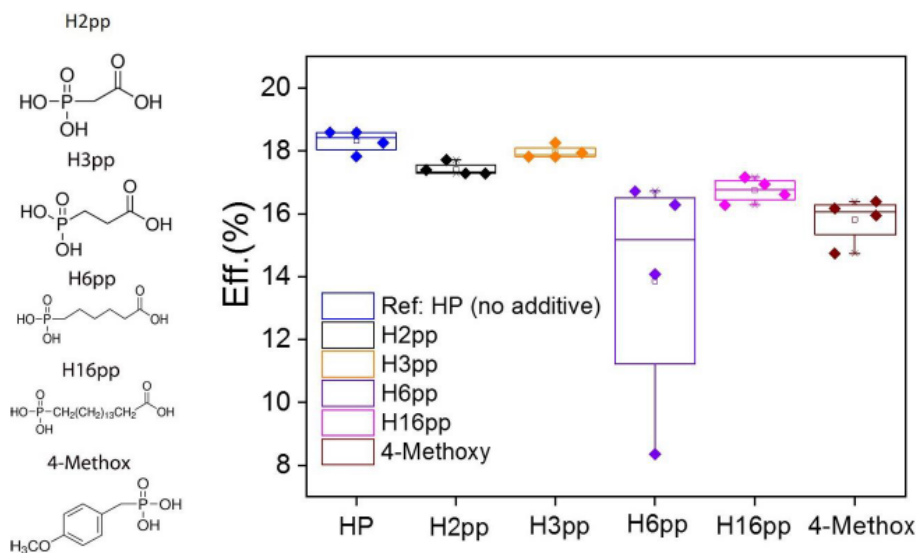


Figure 2.1. Performance of perovskite solar cells doped with different organic additives of the phosphonopropionic acid family. Phosphonoacetic acid (H2pp), 3-Phosphonopropionic acid (H3pp), 6-Phosphonopropionic acid (H6pp) and 16-Phosphonopropionic acid (H16pp) and 4-Methoxybenzylphosphonic acid (4-Methox).

The best PV efficiency was observed for the H3pp additive with efficiency values very similar to the reference PSC at about 18% (champion solar cells at 21% efficiency). We noticed that the H3pp was one of the smallest and simplest molecules in the catalogue we explored. However, the smallest molecule with only 2 carbons, the H2pp, also showed low efficiencies as well as the following one in size, the H6pp with 6 carbons. In this later case, the efficiency was not only low, we also observed a high degree of variability in the PCE. We believe these are signs of the importance of the molecule size with respect to the halide perovskite which has to be optimal for an adequate additive/perovskite interaction.

Figure 2.2 shows the optimization of the H3pp additive concentration with respect to the HP. Our results demonstrated that a 1:500 H3pp:HP ratio resulted in PSCs with the highest PCE,

comparable to that of the reference PSCs. Here it is important to notice that the  $V_{oc}$  of the solar cells are similar or lower than the  $V_{oc}$  of the reference PSCs independently of the concentration of the additive. In fact, increasing the concentration of the additive decreases PCE and  $V_{oc}$  drastically but, in any case, these photovoltaic values are never higher than the reference device. The null improvement of the  $V_{oc}$  and PCE is the first indication that our additives are not passivating deep defect traps (which are directly related to non-radiative recombination as will be explained in the following sections).

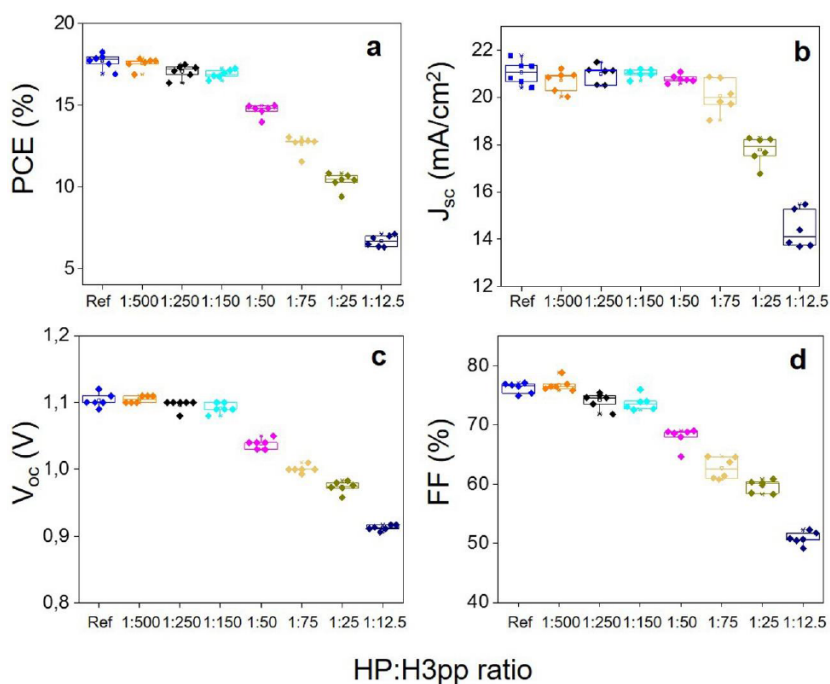


Figure 2.2. Optoelectronic properties of the PSCs as a function of H3pp concentration. a, Power conversion efficiency (PCE), b, Short circuit current ( $J_{sc}$ ), c, Open circuit voltage ( $V_{oc}$ ) and d, Fill factor (FF). H3pp: RbCsMAFA perovskite = 1:500, 1:250, 1:150, 1:75, 1:50, 1:25 and 1:12.5 (molar ratio).

### 2.2.2. Photovoltaic performance and recombination dynamics

For investigate stability of PSCs with the additive H3pp, we assessed the photovoltaic performance of the devices and the recombination dynamics of perovskite with H3pp. As shown in Figure 2.3a, the reverse efficiency of the best device is 21.2%, meanwhile their forward efficiency is 20.4%, reaching stability efficiency of 21.1%. Moreover, the Figure 2.3b. shows how the  $J_{sc}$  from the I-V curves agrees with the integrated current density obtained from the incident photon-to-electron conversion efficiency (IPCE) analysis. These current densities obtained from the I-V curves was analysed and compared with the integrated density by measuring IPCE. The optimization process of the devices yielded good PCE statistics of  $20.2\% \pm 0.7$  and  $20.6\% \pm 0.4$ . Even adding the H3pp to the perovskite, the device shown in both cases the same  $V_{oc}$  of  $1.12\text{ V} \pm 0.01$ , and in the rest of the photovoltaic parameters, they presented similar values (Figure 2.3c-f). Once again, we confirm that the champion PSC shows very similar photovoltaic values as the reference PSC without additive. The  $V_{oc}$  and PCE were never higher than the reference device as described before for other additives of the same family.

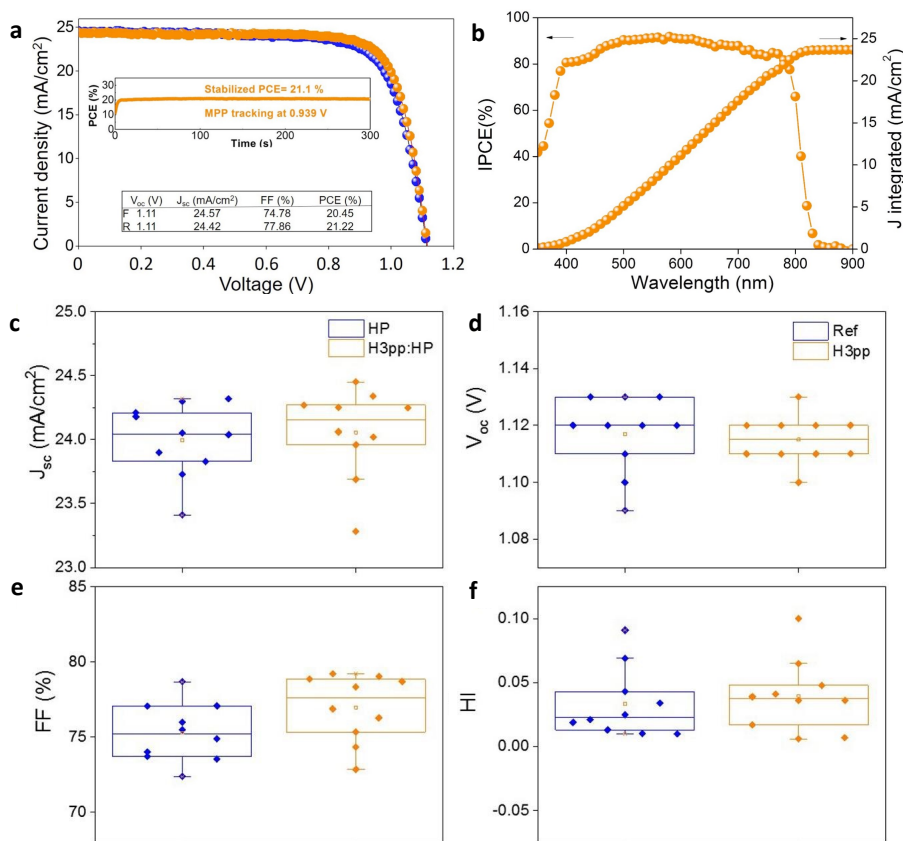


Figure 2.3. a, Optoelectronic parameters of the best device with H3pp: RbCsMAFA perovskite = 1:500 (molar ratio). b, IPCE of the champion H3pp-doped RbCsMAFA perovskite solar cell (1:500). The integrated  $J_{sc}$  for the device is 23.7 mA/cm<sup>2</sup>, in agreement with the measured  $J_{sc}$  of 24.5 mA/cm<sup>2</sup>. Statistic optoelectronic properties of the reference and H3pp-doped PSCs (1:500): c,  $J_{sc}$ . d,  $V_{oc}$ . e, FF and f, hysteresis index (HI).  $HI = (PCE_{Reverse} - PCE_{Forward})/PCE_{Reverse}$ .

**Recombination dynamics.** To analyse and understand the charge recombination process and the effect of the additive on our PSCs, we carried out a series of light intensity-dependent  $V_{oc}$  tests on the entire sample, with structure FTO/c-TiO<sub>2</sub>/m-TiO<sub>2</sub>/perovskite/Spiro-OMeTAD/Au, with and without the H3pp additive (Figure 2.4a). With the following relation:

$$V_{OC} = E_g + \left( \frac{n_{id}kT}{q} \right) \ln \left( \frac{I}{I_0} \right)$$

where  $E_g$  is the bandgap,  $k$  is Boltzmann's constant,  $T$  is temperature,  $q$  is elemental charge, and  $I_0$  is a reference intensity normally at 1 sun. We can extract the diode ideality factor ( $n_{id}$ ) [33]. With this analysis, the  $n_{id} = 1.80$  for PSC with H3pp and 1.85 for PSC without H3pp were observed, which shows that the quality of p-n junction and trap assisted recombination for both devices are approximately the same [34],[35]. Transient photocurrent (TPC) and open circuit voltage drop (OCVD) analyses showed similar characteristics for both recombination and carrier transport, both in the PSC without and with additive (Figure 2.4b and Figure 2.4c).

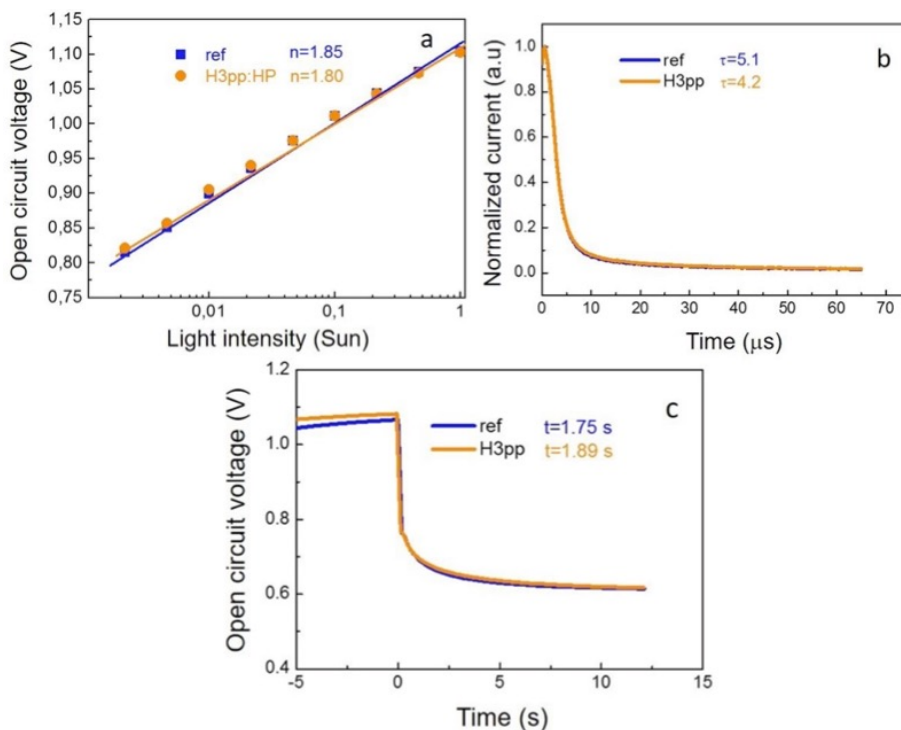


Figure 2.4. Characterization made to complete PSC devices of the type FTO/c-TiO<sub>2</sub>/m-TiO<sub>2</sub>/HP/spiro-OMeTAD/Au with (orange) and without (blue) the H3pp additive. (a) Light intensity dependent  $V_{oc}$ ; (b) Transient photocurrent, and (c) Open circuit voltage decay. In all cases similar  $J_{sc}$  and  $V_{oc}$  with (orange) and without H3pp additive (blue) are observed.

This recombination process of the photoexcited carriers can be studied by time-resolved photoluminescence (TRPL) analyses. This test can elucidate if this process comes from the perovskite layer with and without additives (H3pp). In Figure 2.5 we can observe the TRPL measurements carried out at low fluence of the PSC with and without additives, and the results give similar lifetimes for both samples of  $t \approx 230$  ns [36]. The defect/trap density of the perovskite material is strongly related to the lifetime of charge carriers, specifically non-radiative recombination [34]. The photoluminescence quantum efficiencies (PLQE) at 1 sol, managed to reach 1.90% for the perovskite film without additive and 1.94%

for the perovskite film with additive, concluding the good quality of the films and confirming that the recombination is the same for both samples (Table 2-1).

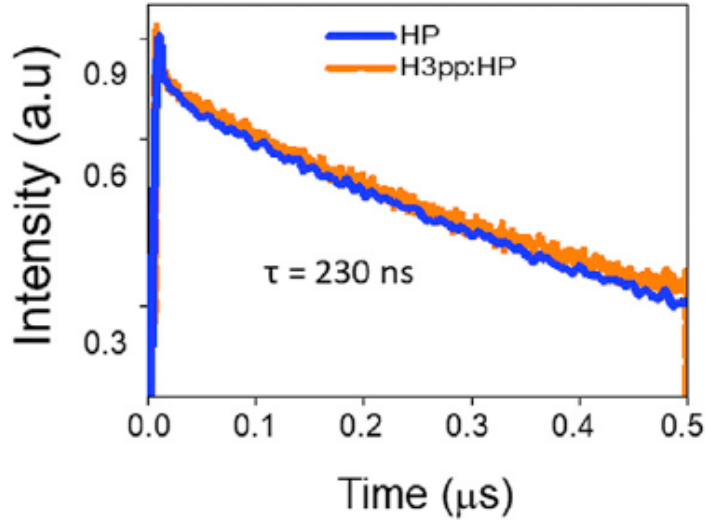


Figure 2.5. TRPL for the HP (blue) and the 1:500 H3pp:HP ratio (orange) on glass.

Table 2-1. Measured PLQE and estimated QFLS of HP thin films and devices with and without H3pp under one sun.

Configuration	HP		H3pp:HP 1:500	
	PLQE	QFLS (eV)	PLQE	QFLS (eV)
a. Glass/Perovskite	1.90%	1.232	1.94%	1.232
b. Glass/c-TiO <sub>2</sub> /m-TiO <sub>2</sub> /Perovskite/Spiro-OMeTAD	0.007%	1.087	0.004%	1.074

Quasi-Fermi level splitting (QFLS) determines the theoretical limit of  $V_{OC}$  that can be obtained for HP and PSCs ( $V_{OC,limit} = QFLS/q$ , where  $q$  is the elemental charge). The equation to calculate the QFLS from PLQE is [37]:

$$QFLS = kT \ln \left( PLQE * \frac{J_G}{J_{0,rad}} \right)$$



where  $k$  is the Boltzmann constant,  $T$  is the temperature,  $J_{0,rad}$  is the radiative thermal equilibrium recombination current density in the dark,  $J_G$  is the generated current density under illumination. For estimation, we assume  $J_G = J_{SC} = 220 \text{ A}\cdot\text{m}^{-2}$ ,  $J_{0,rad} = 6.5 \cdot 10^{-21} \text{ A}\cdot\text{m}^{-2}$  (typical value from the literature), the QFLS values are estimated to be 1.232 eV for the ref and H3pp doped HP, and 1.087 eV and 1.074 eV for the Ref and the H3pp doped PSCs, respectively. Indeed, the same batch of devices of Ref and 1:500 have an average  $V_{OC}$  of 1.07 V and 1.06 V, respectively. In sum, the PLQE results confirm the similar non-radiative recombination in the HP thin films and devices with and without the H3pp additive.

Non-radiative recombination for the films with and without additives was supported by the PLQE and QFLS values, as well as for the perovskite films and the PSCs. In addition, the trap densities of the perovskite films with and without additive were extracted from the space charge-limited current (SCLC) measurements. (Figure 2.6). The trap density can be extracted according to the equation:

$$N_t = \frac{2\varepsilon\varepsilon_0 V_{TFL}}{eL^2}$$

where  $\varepsilon$ ,  $\varepsilon_0$ ,  $V_{TFL}$ ,  $e$  and  $L$  represent the relative dielectric constant of the perovskite, the vacuum permittivity, the filling limit voltage of the trap, elemental charge, and perovskite layer thickness, respectively.

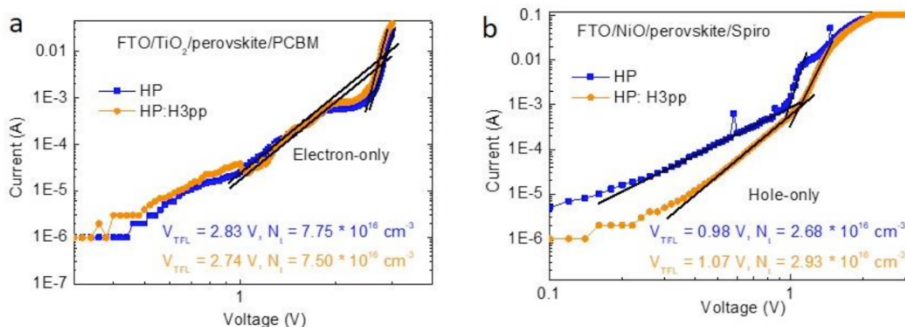


Figure 2.6. Space-charge-limited current (SCLC) for electron-only (a) and hole-only (b) devices with and without the addition of the H3pp additive.

The Optical pump-THz probe (OPTP) spectroscopy is used to test the dynamics of the carriers in a short time by photoconductivity induction. In this test, the conductivity of the induced light was varied, depending on the delay time of the pumping probe [38]. The observed positive photoconductivity indicates charge movements in the presence of light, and the second-order recombination process seems to be caused by the recombination of not generated electron-hole pairs [39].

### 2.2.3. Device stability and ion immobilization

Recently, the ISOS protocols (ISOS-L-11) for perovskites solar cells were recently published. These protocols establish continuous illumination conditions of 1 sun and 1000 hours of operation in an N<sub>2</sub> atmosphere [24] for analyse the operational stability and ion migration (Figure 2.7). We want to study the interaction between the H3pp additive and the PSCs and the possible effects by ion migration and operational stability tests.

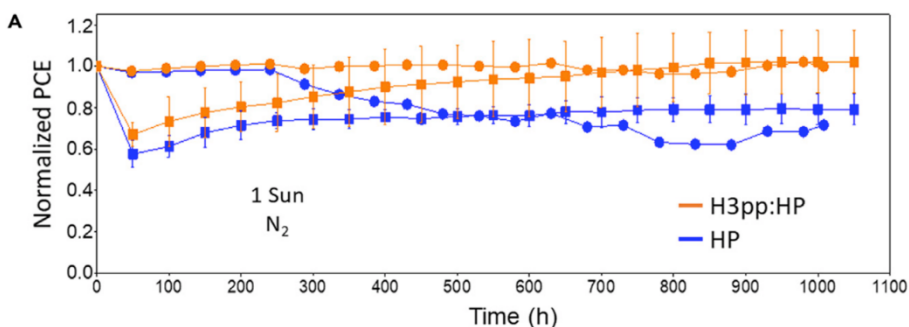


Figure 2.7. Operational stability of PSCs applying RbCsMAFA (●) and CsMAFA (■) with only HP (blue) and with the H3pp:HP (orange), under 1,000 h of continuous illumination at 1 sun under a N<sub>2</sub> atmosphere using white LEDs and MPP tracking. The perovskite-H3pp doping ratio is the optimal 1:500. The initial absolute efficiencies are 19.1% and 19.5% for the reference and H3pp-PSC (1:500) devices, respectively.

In Figure 2.7 we measure operational stability of PSCs devices with or without H3pp using a perovskite of RbCsMAFA (●) as absorbent. Surprisingly, the PSC with H3pp additive shows a retention of almost 100% of its initial PCE. Nevertheless, the reference PSC shows a notable loss of yield of approximately 28% after 1000 h of operation, the same conditions for both samples. Using the same parameters, we reproduce the experiment but modifying the perovskite composition: Cs<sub>0.05</sub>MA<sub>0.15</sub>FA<sub>0.80</sub>Pb<sub>1.05</sub>(I<sub>0.85</sub>Br<sub>0.15</sub>)<sub>3</sub> (CsMAFA) (■) (Figure 2.7). The stability test of the devices with the two different perovskites shows an initial decrease in PCE after few hours, however, after some time, they reach a stable state. This is a predictable behaviour because it is not the first time it has been observed. Here, the charge accumulation at the perovskite interface in the Spiro-OMeTAD is the responsible of this behaviour [40][41]. These surprising results show us that the H3pp additive can be added to different perovskites absorbers, obtaining good long-term stability, and this indicates us that the H3pp additive gives good

stability values to PSCs for different perovskite halides. The thermal stability of PSCs at high temperatures was also tested. The tests were carried out in PSCs without and with additive, in a controlled atmosphere of  $N_2$  and temperature at  $65^\circ\text{C}$ . Figure 2.8 shows the degradation path, the PSC with additive had an approximate loss of 20% of its initial PCE, while the reference sample lost more than 35% of its initial PCE. This demonstrates that the additive aids the stability of the perovskite adsorbent thereby improving the stability of the PSCs.

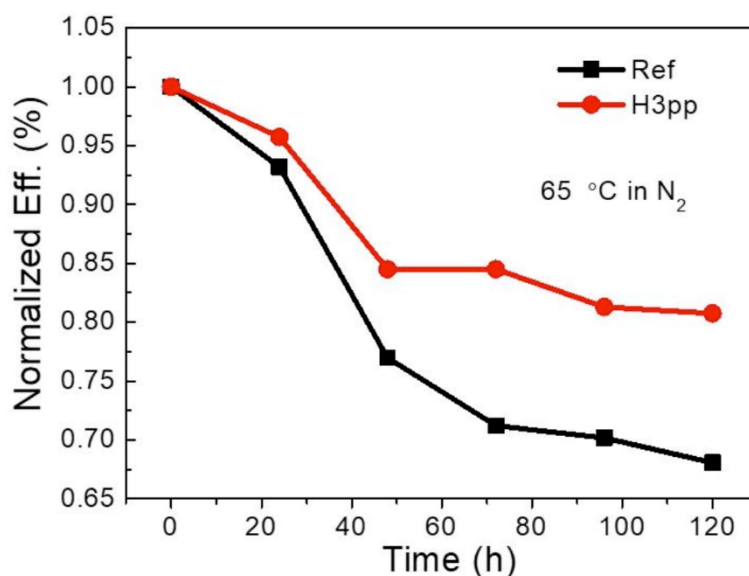


Figure 2.8. Thermal stability analysis carried out to PSCs under  $N_2$  atmosphere at  $65^\circ\text{C}$  for 120 h.

Good results are obtained in the stability studies, and for better understand why this happen in the PSCs with H3pp additives, we carried out measurement of OPTP and PLQE. This test was performed on perovskite films with and without the additive, exposing the samples to long periods of high light intensities (Figure

2.9a and Figure 2.9b). Usually, the high light intensities accelerates sample degradation, but we can predict the lifetime of the device [24]. The OPTP measurements of photoconductivity were made on perovskite with or without H3pp additive thin films under 4 suns for 10 h, and data was collected every 30 minutes. Our measurements showed higher stable photoconductivity on the perovskite film with additive compared to the reference samples with only the perovskite film. The photoconductivity response at determined time and frequency (THz) is proportional to the number of photoexcited electron-hole pairs and the mobility of the charges. Therefore, it presents the process of creating charge and transporting solar cells. These responses obtained under conditions of  $\sim 100$  suns for a period of 10 min in a  $N_2$  atmosphere with the PLQE measurements, show that the samples with additive are more stable than the samples with perovskite alone, which presents almost immediate degradation.

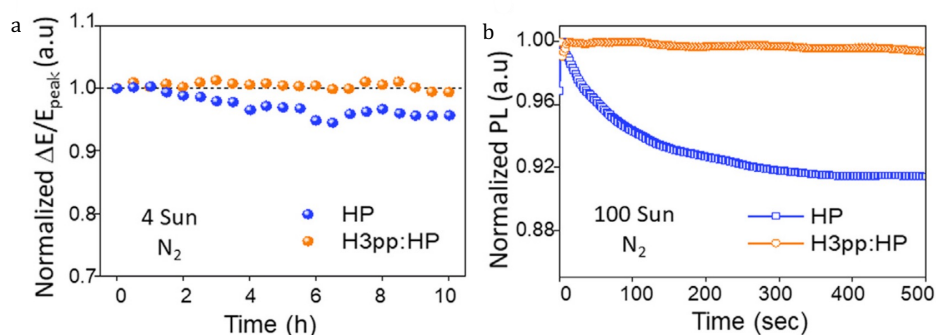


Figure 2.9. a, OPTP analyses of perovskite films on silica, carried out in  $N_2$  under 4 suns for 10 h. and b, PL measurements carried out on perovskite films on glass in  $N_2$  under 100 suns for 500 s.

To further analyse the role that the additive plays in perovskite and mainly in ion migration, electrochemical impedance spectroscopy (EIS) and temperature-dependent dark conductivity measurements were performed on perovskite films without and with additive. Figure 2.10a shows the capacitance results of the PSCs with and without additives, where a low frequency in the range of 1-100 Hz is an order of magnitude lower for the devices with additive, indicating the effective reduction in ion migration and accumulation of charge at the interfaces [42]. The ion migration activation energy ( $E_g$ ) experiment was performed on perovskite samples by measuring the temperature-dependent dark conductivity (Figure 2.10b) according to the Nernst-Einstein equation:

$$\sigma (T) = \frac{\sigma_0}{T e^{\left(\frac{-E_a}{kT}\right)}}$$

, where T is the temperature, k is the Boltzmann constant and  $\sigma_0$  is a constant, and the activation energy  $E_a$  can be extracted from the slope of the  $\ln(\sigma T) \sim 1/KT$  relation. The  $E_a$  for the samples are as follows: for the film with perovskite without additive it is 340 meV and for the sample of perovskite with additive it is 430 meV, that is, it indicates an efficient reduction of the migration of ions.

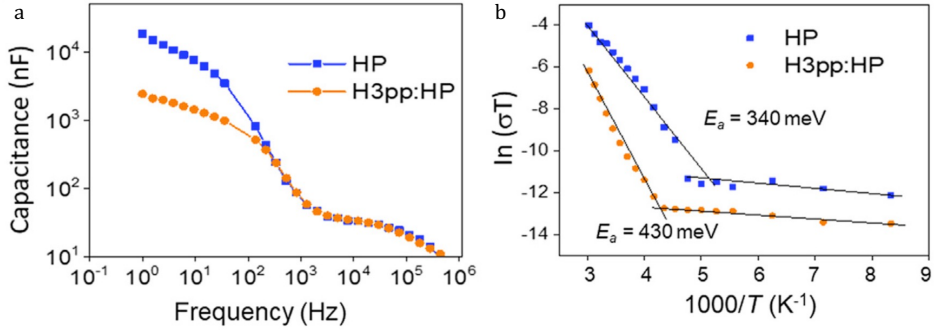
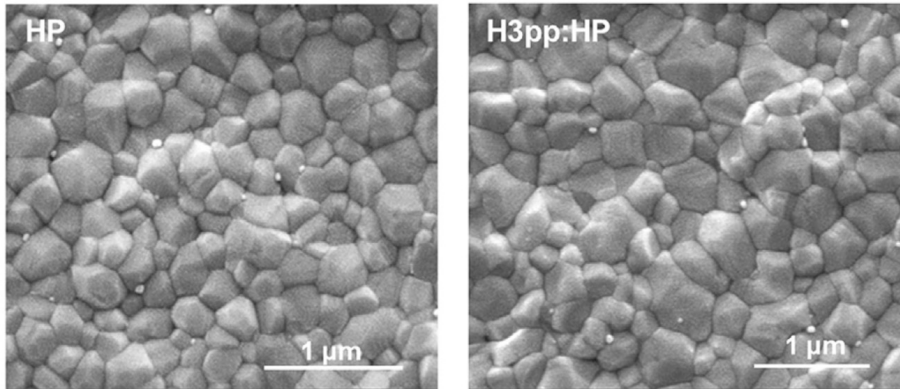


Figure 2.10. **(a)** Frequency-dependent capacitance of PSCs under 1 sun. **(b)** Temperature-dependent dark conductivity of HP thin films on glass.

#### 2.2.4. Effect of H3pp on the perovskite thin film: microstructure and binding mode

The great stability obtained for the perovskite solar cells with the H3pp additive was an excellent result, and the next objective was to understand the effect of the additive on the photovoltaic device. In particular, we want to study the effect of the additive on the structural, morphological, and compositional composition of the perovskite film. The Figure 2.11 correspond to the SEM images of the perovskite film with H3pp additive or without. As represented, the grain size is the same for both conditions, and the H3pp additive does not promote grain growth, so the samples show similar levels of non-radioactive recombination, since grain boundaries have been reported to be factors of defects [43][44].



*Figure 2.11. Top-view SEM image of the HP thin film (left) and the HP with the H3pp additive (right).*

The perovskite thin layer with the H3pp additive were analysed using the annular dark-field scanning transmission electron microscopy (ADF-STEM) equipment. In the Figure 2.12 we can see the cross-sectional view of this perovskite layer with their grain and in the limits of this grain the additive in dark. Also, we can see the additive H3pp highlighted in a blue rectangle. Following ADF-STEM test we want to obtain the chemical composition map of the perovskite with additive of the marked cross-section, electron energy loss spectroscopy (EELS). The maps show that the phosphorus (from  $\text{-PO(OH)}_2$ ) was present in the grain boundaries of the perovskite.



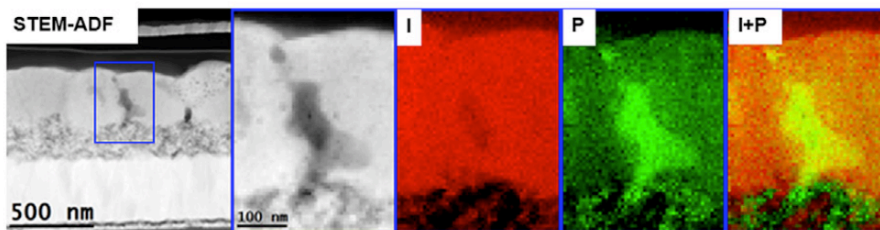


Figure 2.12. ADF-STEM micrograph (lateral view) of the HP:H3pp 1:500 ratio PSC (left), and the corresponding EELS applied for the I, P and I+P analysis in the elemental maps (right).

X-ray Diffraction (XRD) measurements were performed on the RbCsMAFA perovskite films without and with the H3pp additive, where it was observed that there are no peaks and relevant changes in the films (measurements with different concentrations of the H3pp additive) (Figure 2.13). These results prove that the additive H3pp is not being incorporated into the crystal lattice of our perovskite.

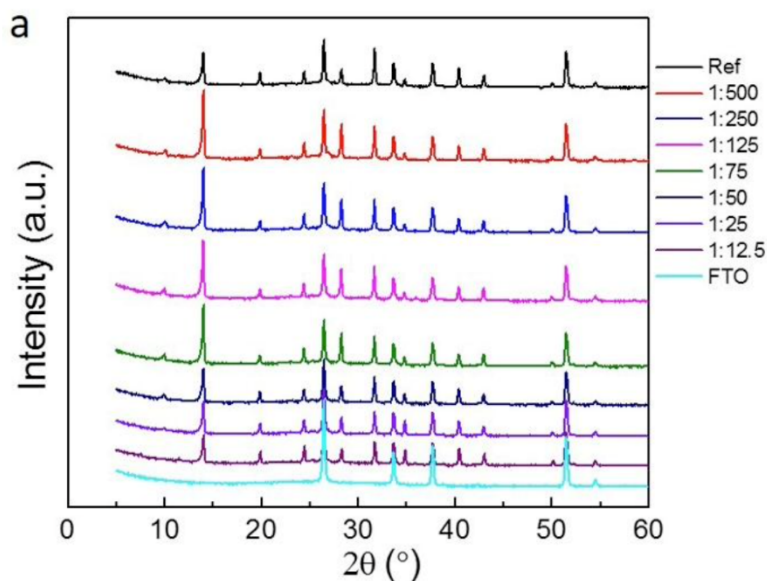


Figure 2.13. XRD patterns of RbCsMAFA perovskite thin films doped with different concentration of H3pp.

The solid-state NMR analyses confirm us that the additive H3pp is not incorporated into the perovskite crystal lattice (Figure 2.14a and b). This reinforces us the idea and the XRD study does not show evidence of significant peaks and changes, and with the ADF-STEM and EELS verified that the additive probably resides at the grain boundaries. Moreover, all this is supported by the band gap of  $\sim 1.56$  eV that did not present significant changes, and this was deduced by the PL and UV-Vis measurements of the perovskite samples with additive (Figure 2.14c and d).

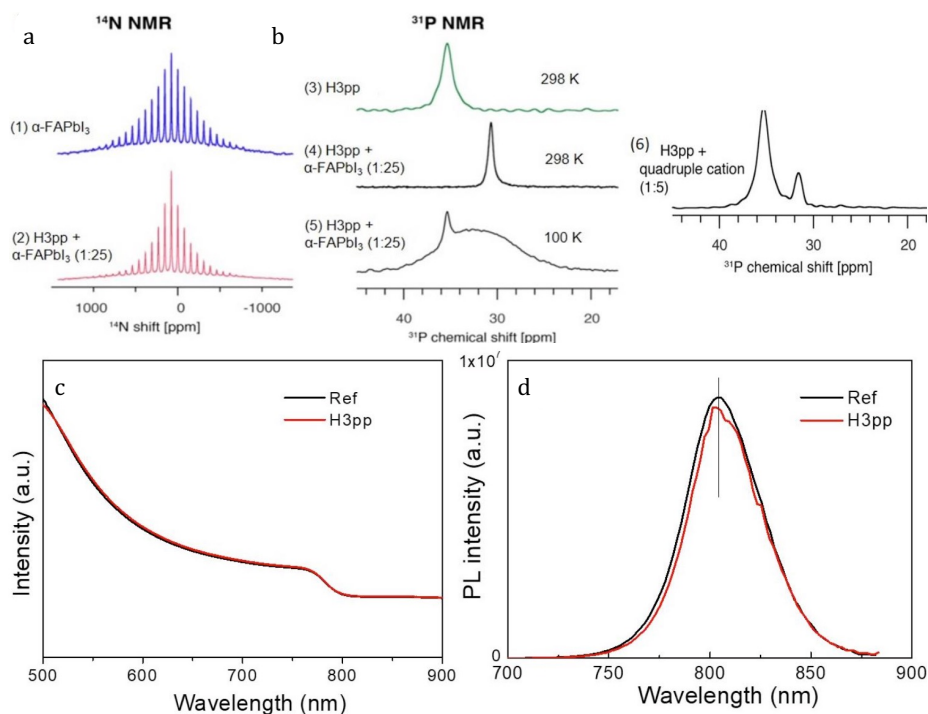


Figure 2.14. Solid-state nuclear magnetic resonance (NMR). (a) Nitrogen-14 solid-state magic angle spinning (MAS) NMR spectra (21.1 T, 298 K and 5 kHz) of (1) bulk mechanochemical  $\alpha\text{-FAPbI}_3$  and (2) H3pp doped bulk mechanochemical  $\alpha\text{-FAPbI}_3$  (1:25 mol/mol). (b) Phosphorus-31 MAS NMR spectra at 21.1 T of (3) neat H3pp (298 K, 12 kHz MAS, echo-detected) and H3pp-doped bulk mechanochemical  $\alpha\text{-FAPbI}_3$  (1:25 mol/mol): (4) at 298 K and 20 kHz MAS (echo-detected) and (5) at 100 K and 12 kHz MAS (1H-31P CP MAS), and (6) H3pp-doped bulk mechanochemical RbCsMAFA perovskite (1:5 mol/mol) at 298 K and 20 kHz MAS (echo-detected). Analyses carried out to the HP and the HP: H3pp. (c) UV-Vis spectra and (d) Photoluminescence spectra.

Fourier transform infrared (FTIR) spectrometer we can study the interaction of the two components the perovskite film and the H3pp additive and we demonstrated an effective interaction between H3pp additive and perovskite (Figure 2.15). Two peaks were found when analysed the perovskite film without additive: a first peak at  $1,71\text{ cm}^{-1}$  and a second peak at  $1,47\text{ cm}^{-1}$ . The first peak corresponds to the antisymmetric C–N stretch, which overlaps with the  $\text{–C=O}$  stretch. The second peak corresponds to the symmetric  $\text{NH}_3^+$  bending. With the addition of the additive H3pp in the perovskite film, a peak change from  $1,26$  to  $1,24\text{ cm}^{-1}$  was found, which corresponds to  $\text{–P=O}$ ; while the peak of  $1,71$  to  $1,70\text{ cm}^{-1}$  remained unchanged. This peak behaviour indicates two types of interaction between the additive H3pp and the perovskite film, a weak interaction through the carboxylate group ( $\text{–C=O}$ ) and a strong interaction through the phosphonate group ( $\text{–P=O}$ ).

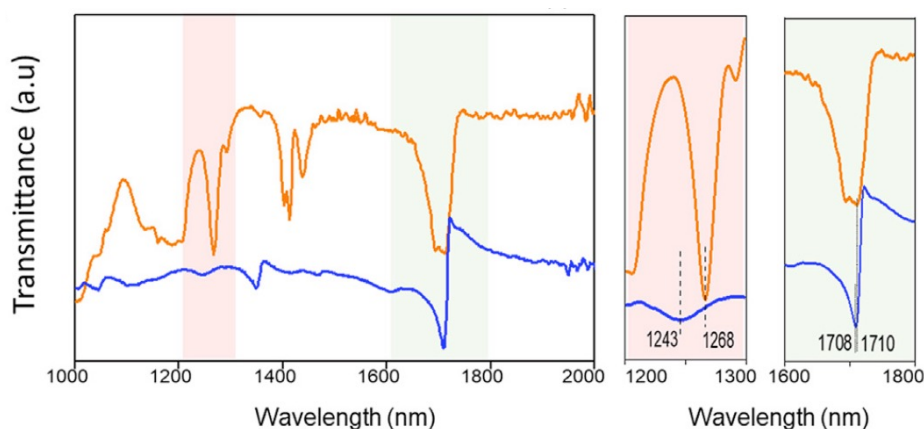


Figure 2.15. FTIR analysis of the HP (orange) and HP:H3pp (blue), indicating the peaks corresponding to the  $\text{P=O}$  stretching mode between  $1,220$  and  $1,300\text{ nm}$  and the  $\text{C=O}$  stretching mode between  $1,600$  and  $1,800\text{ nm}$ .

We have demonstrated two types of interaction into the perovskite film with the H3pp additive, and to delve deeper into this interaction process at the atomic level, its interaction was studied using density functional theory (DFT) calculations.

To perform the DFT calculation, the perovskite of  $\alpha$ -FAPbI<sub>3</sub> is selected as a model. First, the binding energy ( $E_{\text{binding}}$ ) of the additive H3pp on the perovskite surface terminated in Formamidinium (FA) and Lead (Pb) Iodide was calculated according to the following relationship:

$$E_{\text{binding}} = E_{\text{H3pp}} + E_{\text{surface}} - E_{\text{surface-H3pp}}$$

Where  $E_{\text{H3pp}}$ ,  $E_{\text{surface}}$  and  $E_{\text{surface-H3pp}}$  are total energies of the perovskite film with the additive. This give us several interaction models to be considered, since all the models were favourable, and assuming that the binding energies are approximately in the range from 1.6 to 3.1 eV.

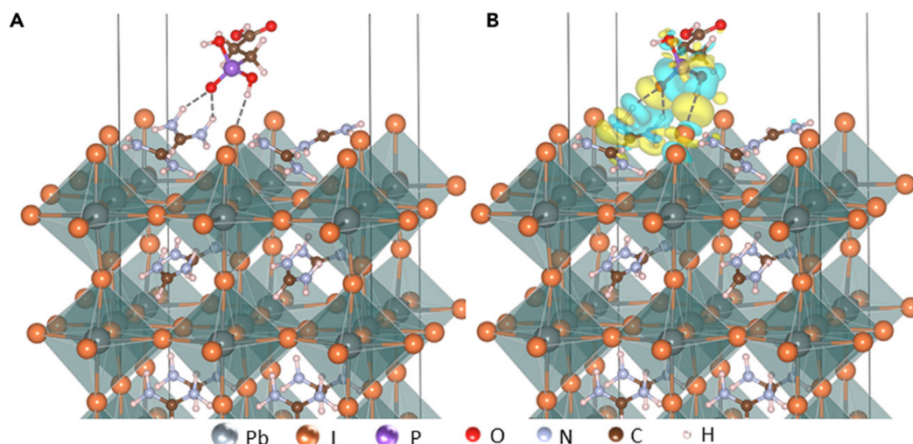


Figure 2.16. Example of one dominant interaction mode, where H3pp binds to the FAI-terminated surface of FAPbI<sub>3</sub>, forming three hydrogen bonds of two different types. (b) Charge redistribution at the H3pp/FAPbI<sub>3</sub> interface upon the adsorption of H3pp, where charge accumulation and depletion are indicated by yellow and cyan, respectively.

Among all the favourable models obtained by DFT calculation, the most favourable model is where the interaction of the H3pp additive with the perovskite occurs, and the FAI and  $\text{-PO(OH)}_2$  terminations are joined by two different types of hydrogen bonds. These two types are formed by three hydrogen bonds in which the hydrogen atom  $\text{-P-OH}$  interacts with I- (HI) or two hydrogen atoms of  $\text{NH}_2$  of  $\text{FA}^+$  (OH) interact with the oxygen atom of  $\text{-P=O}$  (Figure 2.16a). Through a charge density analysis, the presence of the types of hydrogen bonds was verified, due to the depletion of electrons from the hydrogen atoms (H) to the oxygen (O) and iodine (I) atoms. These H atoms present are both from the additive H3pp and from the perovskite, but in both cases the charges are well redistributed, which means that the interfacial interactions are strong. The H bonds that are created with the perovskite could wear out the  $\text{P=O}$  bonds of the H3pp additive. H3pp has an affinity to bind more strongly to FAI-terminated surfaces than to  $\text{PbI}_2$ -terminated ones

(Figure 2.16b). The stretching wave number of the  $-P=O$  bonds, in the calculations carried out with the DFT, range from 1.24 to 1.17  $\text{cm}^{-1}$ , which shows that the bonds show signs of wear.

Relating the previous studies done with DFT and FTIR, it is concluded that the interaction of the additive H3pp and the perovskite are formed by two types of hydrogen bonds:  $-PO(OH)_2$  and the cations  $FA^+$  and  $I^-$  anions. All this backed up with FTIR, XRD and liquid-state NMR measurements (Figure 2.17) with samples made in this liquid.

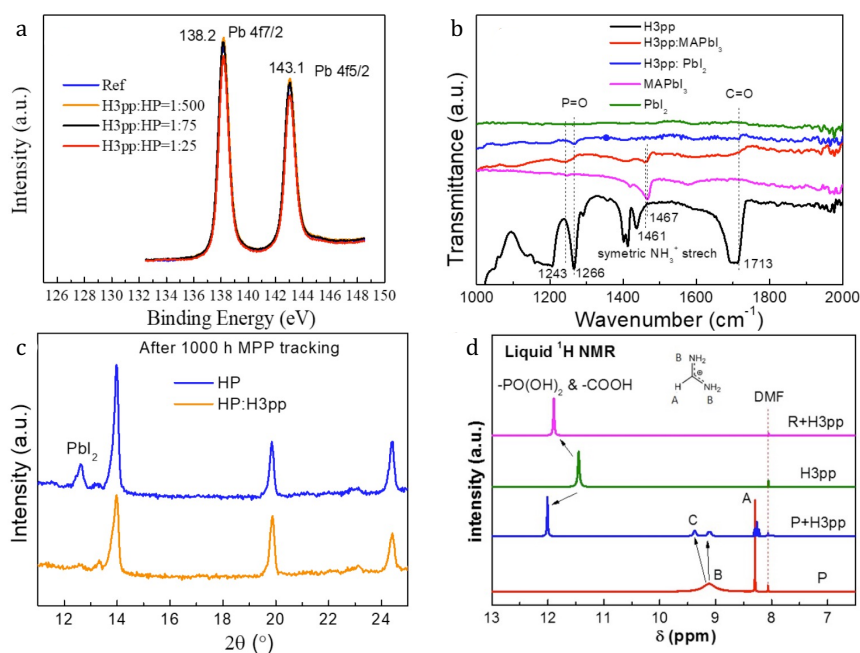


Figure 2.17. XPS and FTIR analysis of the HP and the H3pp:HP: (a) with different concentration of the additive H3pp XPS analysis (b) FTIR analyses of the MAPbI<sub>3</sub> (MAPI), the H3pp, the PbI<sub>2</sub> and the combination of H3pp with MAPI and PbI<sub>2</sub>. XRD and NMR analyses of the HP and the HP:H3pp: (c) XRD analyses of the perovskite samples with and without the H3pp additive, after 1000 h under continuous light irradiation of 1 sun, MPP tracking,  $N_2$  atmosphere, RT. (d) Liquid-state  $^1H$  NMR spectra of the neat H3pp, the RbPbI<sub>3</sub>:H3pp (R+H3pp), perovskite:H3pp (P+H3pp) mixtures and the neat perovskite (P). Here perovskite is RbCsMAFA. To ensure the detection resolution, RbCsMAFA (or RbPbI<sub>3</sub>): H3pp= 2.5:1 was prepared in 0.5 mL DMF- $d_7$  [45].

### 2.2.5. Passivation of shallow point defects in the HP absorber

In the current literature, it is reported that passivation of deep defects, for example Pb-I [12] antisite defects, helps non-radiative losses, having a direct impact on device performance, mainly on VOC and PCE [46][47][48]. But characterization by PLQE and OPTP of the perovskite film with H3pp additive, shows an unexpected result according to literature. Here at a low fluence of  $\sim 1$  suns the perovskite film shows no non-radioactive defects, nevertheless, when fluences were above  $\sim 10$  suns, there were small decreases in the deep traps, providing good stability, but decreasing device performance. These results obtained were unexpected as mentioned because the literature reports that the application of additives in PSCs improve both efficiency and stability [49][50], and defects of these properties are linked often. Perovskites are ion/electron conductors that have shallow traps, which are not generally considered. In this work we suggest that the binding of the phosphonate functional groups of H3pp to the perovskite demonstrates the passivation of shallow grain boundary defects. As an example, the FA and I vacancies [51][52] immobilize the ions in this functional groups. To analyse the shallow defects in our samples, thermal admittance spectroscopy (TAS) measurements [53] were performed varying temperature, with the purpose of studying the energy distribution in the defects of the devices.

The TAS results of the perovskite sample (reference) presented two types of shallower defects at 0,13 eV (D1) and 0,16 eV (D2), while the perovskite samples with additive (H3pp) presented one type of

deeper defect at 0,20 eV (D3). The perovskite samples with additive are absent from defects (D1), the comparison of the two deepest defects (D2 and D3) shows that the addition of H3pp additive to the perovskite passives the D1 defects, and to a lesser extent the deeper defects D2 (Figure 2.18).

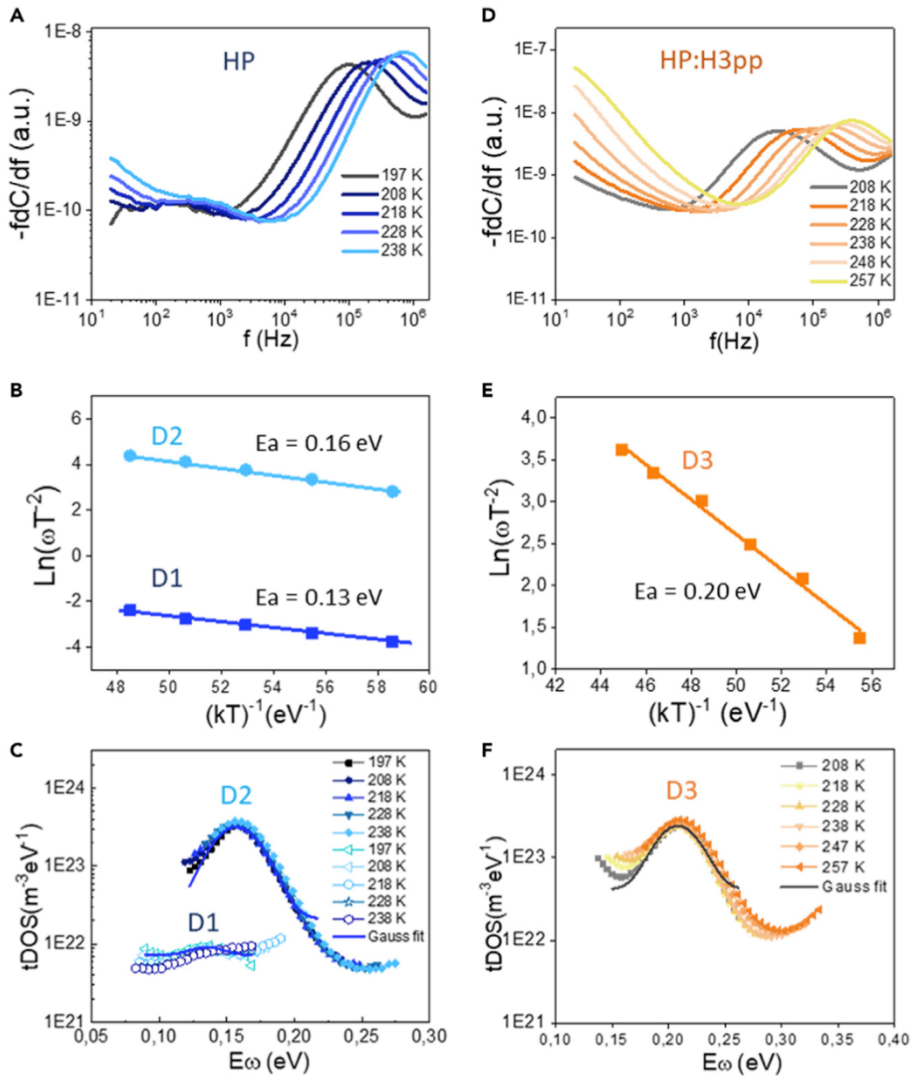


Figure 2.18. (A–F) Differentiated capacitance spectra (A and D), Arrhenius plots of the inflection frequencies determined from the derivative of the admittance spectra (B and E) and trap density of states (tDOS) deduced from temperature-dependent C–F plots (C and F) for the



*perovskite solar cells with (D–F) and without H3pp (A–C). The activation energy ( $E_a$ ) was extracted for each defect and shown inside the figures [54].*

### 2.3. Discussions

The research to improve the stability of PSCs is a trending topic in science, and the addition of organic additives has proven to be beneficial due to their known interaction with perovskite. In this work, PSCs were manufactured by applying additives from the group of phosphonopropionic acids containing phosphates and carboxyls. The optoelectronic properties presented similar results for both devices without and with additives (VOC of  $\sim 1.1$  V and PCE of  $\sim 21\%$ ), for what the PCS with additive did not present values higher than the reference PSC. This is because the additive H3pp has low influence on non-radiative recombination in perovskite. In other words, non-radiative recombination is related to deep defects that act as recombination points, so we believe that our film is not passivated or has little passivity when we use the additive H3pp. But, on the other hand, it presented interesting stability results, retaining almost 100% of the initial PCE after 1000 h under MPP operating conditions and light irradiation. Photoconductivity and carrier recombination studies under illumination supported the good stability of PSCs with additive H3pp, not only under 1 sun but also under intense light irradiation up to 100 suns. Another interesting point presented by the H3pp additive was its use in different perovskite absorbers (CsMAFA and RbCsMAFA), presenting the same stability characteristic. With the PLQE and OPTP studies, any relationship with non-radiative defects is ruled out, but it should be

noted that at more than 10 suns there is a decrease in the density of deep traps, which has an impact on the stability of the PSCs but not on performance. It was also observed that the ion anchors were the mechanism that contributed to the improvement of the stability of the devices with additive. With FTIR and NMR analysis it was found that the interactions between perovskite and the H3pp additive are strongly related. With the DTF calculations it was possible to affirm this relationship and noting that these strong relationships were due particularly to the phosphane groups. Which are two types of hydrogen bonds (H-I and O-H). These interactions prevent the creation of point defects on the perovskite surface and grain boundaries, for example in the FA and I vacancies. This allows ion immobilization and good stabilities in PSCs. With the TAS analysis, it was shown that the H3pp additive reduces the shallow point defects, explaining why the PSCs without and with the H3pp additive present similar electrical characteristics, since the deep defects are related to efficiency and voltage. Putting all these results together, we have shown that H3pp improves the stability of PSCs, so we should continue researching to improve their efficiency and stability, however, we are on the right track.

## 2.4. References

- [1] X. Li *et al.*, "A vacuum flash-assisted solution process for high-efficiency large-area perovskite solar cells," *Science* (80-. ), vol. 353, no. 6294, pp. 58–62, Jul. 2016.
- [2] Q. Jiang *et al.*, "Surface passivation of perovskite film for efficient solar cells," *Nat. Photonics*, pp. 1–25, 2019.
- [3] S. Bai *et al.*, "Planar perovskite solar cells with long-term stability using ionic liquid additives," *Nature*, vol. 571, no. 7764, pp. 245–250, 2019.
- [4] N. K. Noel *et al.*, "Enhanced photoluminescence and solar cell performance via Lewis base passivation of organic-inorganic lead halide perovskites," *ACS Nano*, vol. 8, no. 10, pp. 9815–9821, Oct. 2014.
- [5] D. Bi *et al.*, "Polymer-templated nucleation and crystal growth of perovskite films for solar cells with efficiency greater than 21%," *Nat. Energy*, vol. 1, no. 10, pp. 1–5, Oct. 2016.
- [6] J. Han *et al.*, "Hybrid PbS Quantum-Dot-in-Perovskite for High-Efficiency Perovskite Solar Cell," *Small*, vol. 14, no. 31, p. 1801016, Aug. 2018.
- [7] S. Liu *et al.*, "A Review on Additives for Halide Perovskite Solar Cells," *Advanced Energy Materials*, vol. 10, no. 13. Wiley-VCH Verlag, 01-Apr-2020.
- [8] Y. Wang *et al.*, "Interfacial modification towards highly efficient and stable perovskite solar cells," *Nanoscale*, vol. 12, no. 36, pp. 18563–18575, Sep. 2020.
- [9] J. Peng *et al.*, "A Universal Double-Side Passivation for High Open-Circuit Voltage in Perovskite Solar Cells: Role of Carbonyl Groups in Poly(methyl methacrylate)," *Adv. Energy Mater.*, vol. 8, no. 30, p. 1801208, Oct. 2018.
- [10] L. Guan, N. Jiao, and Y. Guo, "Trap-State Passivation by Nonvolatile Small Molecules with Carboxylic Acid Groups for Efficient Planar Perovskite Solar Cells," *J. Phys. Chem. C*, vol. 123, no. 23, pp. 14223–14228, Jun. 2019.
- [11] M. J. Choi *et al.*, "Functional additives for high-performance inverted planar perovskite solar cells with exceeding 20% efficiency: Selective complexation of organic cations in precursors," *Nano Energy*, vol. 71, p. 104639, May 2020.
- [12] R. Wang *et al.*, "Constructive molecular configurations for surface-defect passivation of perovskite photovoltaics,"

- Science* (80-. ), vol. 366, no. 6472, pp. 1509–1513, 2019.
- [13] I. L. Braly *et al.*, “Hybrid perovskite films approaching the radiative limit with over 90% photoluminescence quantum efficiency,” *Nat. Photonics* 2018 126, vol. 12, no. 6, pp. 355–361, Apr. 2018.
  - [14] X. Li *et al.*, “Improved performance and stability of perovskite solar cells by crystal crosslinking with alkylphosphonic acid  $\omega$ -ammonium chlorides,” *Nat. Chem.*, vol. 7, no. 9, pp. 703–711, 2015.
  - [15] D. W. deQuilettes *et al.*, “Photoluminescence Lifetimes Exceeding 8  $\mu$ s and Quantum Yields Exceeding 30% in Hybrid Perovskite Thin Films by Ligand Passivation,” *ACS Energy Lett.*, vol. 1, no. 2, pp. 438–444, Aug. 2016.
  - [16] A. Faucon *et al.*, “Fluorescent carboxylic and phosphonic acids: comparative photophysics from solution to organic nanoparticles,” *Phys. Chem. Chem. Phys.*, vol. 15, no. 30, pp. 12748–12756, Jul. 2013.
  - [17] G. Guerrero, J. G. Alauzun, M. Granier, D. Laurencin, and P. H. Mutin, “Phosphonate coupling molecules for the control of surface/interface properties and the synthesis of nanomaterials,” *Dalt. Trans.*, vol. 42, no. 35, pp. 12569–12585, Sep. 2013.
  - [18] D. G. Brown, P. A. Schauer, J. Borau-Garcia, B. R. Fancy, and C. P. Berlinguette, “Stabilization of Ruthenium Sensitizers to TiO<sub>2</sub> Surfaces through Cooperative Anchoring Groups,” *J. Am. Chem. Soc.*, vol. 135, no. 5, pp. 1692–1695, Feb. 2013.
  - [19] J. W. Lee, S. G. Kim, J. M. Yang, Y. Yang, and N. G. Park, “Verification and mitigation of ion migration in perovskite solar cells,” *APL Mater.*, vol. 7, no. 4, p. 41111, Apr. 2019.
  - [20] C. Ran, J. Xu, W. Gao, C. Huang, and S. Dou, “Defects in metal triiodide perovskite materials towards high-performance solar cells: origin, impact, characterization, and engineering,” *Chem. Soc. Rev.*, vol. 47, no. 12, pp. 4581–4610, Jun. 2018.
  - [21] A. Rajagopal, K. Yao, and A. K.-Y. Jen, “Toward Perovskite Solar Cell Commercialization: A Perspective and Research Roadmap Based on Interfacial Engineering,” *Adv. Mater.*, vol. 30, no. 32, p. 1800455, Aug. 2018.
  - [22] R. Wang *et al.*, “Constructive molecular configurations for surface-defect passivation of perovskite photovoltaics,” *Science* (80-. ), vol. 366, no. 6472, pp. 1509–1513, Dec. 2019.
  - [23] X. Zheng *et al.*, “Managing grains and interfaces via ligand

- anchoring enables 22.3%-efficiency inverted perovskite solar cells," *Nat. Energy* 2020 52, vol. 5, no. 2, pp. 131–140, Jan. 2020.
- [24] M. V. Khenkin *et al.*, "Consensus statement for stability assessment and reporting for perovskite photovoltaics based on ISOS procedures," *Nat. Energy*, vol. 5, no. 1, pp. 35–49, Jan. 2020.
  - [25] H. Xie and M. Lira-Cantu, "Multi-component engineering to enable long-term operational stability of perovskite solar cells," *J. Phys. Energy*, vol. 2, no. 2, p. 024008, Apr. 2020.
  - [26] C. Pereyra, H. Xie, and M. Lira-Cantu, "Additive engineering for stable halide perovskite solar cells," *J. Energy Chem.*, vol. 60, pp. 599–634, Sep. 2021.
  - [27] Y. Zhao *et al.*, "Mobile-Ion-Induced Degradation of Organic Hole-Selective Layers in Perovskite Solar Cells," *J. Phys. Chem. C*, vol. 121, no. 27, pp. 14517–14523, Jul. 2017.
  - [28] B. Chen, P. N. Rudd, S. Yang, Y. Yuan, and J. Huang, "Imperfections and their passivation in halide perovskite solar cells," *Chem. Soc. Rev.*, vol. 48, no. 14, pp. 3842–3867, Jul. 2019.
  - [29] S. Tan *et al.*, "Shallow Iodine Defects Accelerate the Degradation of  $\alpha$ -Phase Formamidinium Perovskite," *Joule*, vol. 4, no. 11, pp. 2426–2442, Nov. 2020.
  - [30] D. G. Brown, P. A. Schauer, J. Borau-Garcia, B. R. Fancy, and C. P. Berlinguette, "Stabilization of Ruthenium Sensitizers to TiO<sub>2</sub> Surfaces through Cooperative Anchoring Groups," *J. Am. Chem. Soc.*, vol. 135, no. 5, pp. 1692–1695, Feb. 2013.
  - [31] R. Luschtinetz, S. Gemming, and G. Seifert, "Anchoring functional molecules on TiO<sub>2</sub> surfaces: A comparison between the carboxylic and the phosphonic acid group," *Eur. Phys. J. Plus* 2011 12610, vol. 126, no. 10, pp. 1–13, Oct. 2011.
  - [32] L. A. Martini *et al.*, "Modular assembly of high-potential zinc porphyrin photosensitizers attached to TiO<sub>2</sub> with a series of anchoring groups," *J. Phys. Chem. C*, vol. 117, no. 28, pp. 14526–14533, Jul. 2013.
  - [33] W. Tress *et al.*, "Interpretation and evolution of open-circuit voltage, recombination, ideality factor and subgap defect states during reversible light-soaking and irreversible degradation of perovskite solar cells," *Energy Environ. Sci.*, vol. 11, no. 1, pp. 151–165, Jan. 2018.
  - [34] D. Yang *et al.*, "High efficiency planar-type perovskite solar

- cells with negligible hysteresis using EDTA-complexed SnO<sub>2</sub>,” *Nat. Commun.* 2018 91, vol. 9, no. 1, pp. 1–11, Aug. 2018.
- [35] Q. Jiang *et al.*, “Surface passivation of perovskite film for efficient solar cells,” *Nat. Photonics* 2019 137, vol. 13, no. 7, pp. 460–466, Apr. 2019.
  - [36] S. D. Stranks *et al.*, “Electron-hole diffusion lengths exceeding 1 micrometer in an organometal trihalide perovskite absorber,” *Science (80-. )*, vol. 342, no. 6156, pp. 341–344, 2013.
  - [37] M. Stolterfoht *et al.*, “The impact of energy alignment and interfacial recombination on the internal and external open-circuit voltage of perovskite solar cells,” *Energy Environ. Sci.*, vol. 12, no. 9, pp. 2778–2788, Sep. 2019.
  - [38] P. Becker *et al.*, “Low Temperature Synthesis of Stable  $\gamma$ -CsPbI<sub>3</sub> Perovskite Layers for Solar Cells Obtained by High Throughput Experimentation,” *Adv. Energy Mater.*, vol. 9, no. 22, p. 1900555, Jun. 2019.
  - [39] J. S. Manser and P. V. Kamat, “Band filling with free charge carriers in organometal halide perovskites,” *Nat. Photonics* 2014 89, vol. 8, no. 9, pp. 737–743, Aug. 2014.
  - [40] L. Wang *et al.*, “A Eu 3+ -Eu 2+ ion redox shuttle imparts operational durability to Pb-I perovskite solar cells,” *Science (80-. )*, vol. 363, no. 6424, pp. 265–270, Jan. 2019.
  - [41] Z. Liu *et al.*, “A holistic approach to interface stabilization for efficient perovskite solar modules with over 2,000-hour operational stability,” *Nat. Energy* 2020 58, vol. 5, no. 8, pp. 596–604, Jul. 2020.
  - [42] H.-S. Kim *et al.*, “Control of I-V Hysteresis in CH<sub>3</sub>NH<sub>3</sub>PbI<sub>3</sub> Perovskite Solar Cell,” *J. Phys. Chem. Lett.*, vol. 6, no. 22, pp. 4633–4639, Nov. 2015.
  - [43] D. Bi *et al.*, “Multifunctional molecular modulators for perovskite solar cells with over 20% efficiency and high operational stability,” *Nat. Commun.* 2018 91, vol. 9, no. 1, pp. 1–10, Oct. 2018.
  - [44] D. Shi *et al.*, “Low trap-state density and long carrier diffusion in organolead trihalide perovskite single crystals,” *Science (80-. )*, vol. 347, no. 6221, pp. 519–522, Jan. 2015.
  - [45] N. Li *et al.*, “Cation and anion immobilization through chemical bonding enhancement with fluorides for stable halide perovskite solar cells,” *Nat. Energy* 2019 45, vol. 4, no. 5, pp. 408–415, May 2019.

- [46] S. Kumar, G. Hodes, and D. Cahen, "Defects in halide perovskites: The lattice as a boojum?," *MRS Bull.*, vol. 45, no. 6, pp. 478–484, Jun. 2020.
- [47] Z. Peng *et al.*, "Cs<sub>0.15</sub>FA<sub>0.85</sub>PbI<sub>3</sub>/CsxFA<sub>1-x</sub>PbI<sub>3</sub> Core/Shell Heterostructure for Highly Stable and Efficient Perovskite Solar Cells," *Cell Reports Phys. Sci.*, vol. 1, no. 10, p. 100224, Oct. 2020.
- [48] C.-J. Tong, L. Li, L.-M. Liu, and O. V. Prezhdo, "Synergy between Ion Migration and Charge Carrier Recombination in Metal-Halide Perovskites," *J. Am. Chem. Soc.*, vol. 142, no. 6, pp. 3060–3068, Feb. 2020.
- [49] Y.-H. Lin *et al.*, "A piperidinium salt stabilizes efficient metal-halide perovskite solar cells," *Science (80-. )*, vol. 369, no. 6499, pp. 96–102, Jul. 2020.
- [50] S. Yang *et al.*, "Stabilizing halide perovskite surfaces for solar cell operation with wide-bandgap lead oxysalts," *Science (80-. )*, vol. 365, no. 6452, pp. 473–478, 2019.
- [51] J. M. Ball and A. Petrozza, "Defects in perovskite-halides and their effects in solar cells," *Nat. Energy* 2016 111, vol. 1, no. 11, pp. 1–13, Oct. 2016.
- [52] W. J. Yin, T. Shi, and Y. Yan, "Unique properties of halide perovskites as possible origins of the superior solar cell performance," *Adv. Mater.*, vol. 26, no. 27, pp. 4653–4658, 2014.
- [53] X. Zheng *et al.*, "Managing grains and interfaces via ligand anchoring enables 22.3%-efficiency inverted perovskite solar cells," *Nat. Energy*, vol. 5, no. 2, pp. 131–140, 2020.
- [54] B. Chen, P. N. Rudd, S. Yang, Y. Yuan, and J. Huang, "Imperfections and their passivation in halide perovskite solar cells," *Chemical Society Reviews*, vol. 48, no. 14. Royal Society of Chemistry, pp. 3842–3867, 21-Jul-2019.

# Chapter 3: Carbon-based Perovskite Solar Cells

---

## 3.1. Introduction

The goal of this chapter is to study the stability in carbon-based HTL-free PSCs as an improvement strategy, known as one of the most stable architectures [1]. Typical PSCs use metallic electrodes, such as gold and silver, along with expensive hole transporting layer (HTL), such as spiro-OMeTAD. This causes that the long-term stability of PSCs is limited, due to the low thermal stability and high reactivity of these materials. In contrast, HTL-free carbon-based PSCs provide better stability [2]. The drawback of the C-PSCs is their low PCE, an efficiency of around 16% in current reports [3][4][5][6][7]. After several investigations and tireless efforts of research groups the scientific community have proposed carbon materials as the cost-effective option of HTL introduced in PSCs to address the above problems. Considering the proper working function of 5.0 eV close to that of Au (5.1 eV) makes carbon an ideal candidate for the PSC back electrode. Table 3-1 shows a summary of the research works that use carbon as a counter electrode. As represented, carbon-based perovskite solar cells (C-PSCs) have many factors to solving the problems of instability, fabrication



complexity and high costs faced by record-breaking metal/HTL-based PSCs [9].

*Table 3-1. Summary of the solar cell configuration and the corresponding photovoltaic parameters obtained from different groups applying the doctor blade technique for the fabrication of carbon electrodes in perovskite solar cells.*

FF (%)	Voc (V)	Jsc (mA/cm <sup>2</sup> )	PCE (%)	Device structure	Method	Ref.
0.57	1.08	22.19	13.64	ITO/SnO <sub>2</sub> /Perovskite/Carbon	Doctor blade coating	[10]
0.66	1.08	20.40	14.60	FTO/SnO <sub>2</sub> /Perovskite/CuSCN/Carbon	Doctor blade coating	[11]
0.65	0.89	20.30	11.9	FTO/TiO <sub>2</sub> /SiO <sub>2</sub> /Perovskite/Carbon	Doctor blade coating	[12]
0.68	1.05	20.92	15.18	PET/IZO/PTAA/Perovskite/PCBM:PMMA/Carbon	Doctor blade coating	[13]
0.77	0.94	21.45	15.60	FTO/TiO <sub>2</sub> /ZrO <sub>2</sub> /Perovskite/Carbon	Doctor blade coating	[14]

For these reasons, carbon-based PSCs have a unique potential to reach the sweet spot for disruptive and revolutionary photovoltaic energy: low cost, high stability, high efficiency, and sustainability (Figure 3.1).



*Figure 3.1. Diagram of improvements when using carbon as hole transport layer in perovskite solar cells.*

Interestingly, carbon nanomaterials have been used in other types of solar cells and have shown excellent performance. The hydrophobic nature of carbon promotes less moisture absorption in the carbon-based cell, which improves cell lifetime [15][16]. On the other hand, the use of carbon electrodes has demonstrated the ability to extract photogenerated holes by themselves, which allows PSCs to be fabricated without the need for an HTL, which are expensive and unstable, promoting HTL-free monolithic PSCs [17].

The different crystal structures with very different chemical and physical properties of carbons (Figure 3.2.) are not ideal for C-PSCs. Especially, graphite and carbon black have accessibility features; controllable porosity, chemical stability and conductivity, as well as a high surface-to-volume ratio [18], leading to clearly distinguishable charge transport behaviours [19]. The C-PSCs with better stability and efficiencies presented use carbon black and graphite as counter electrodes.

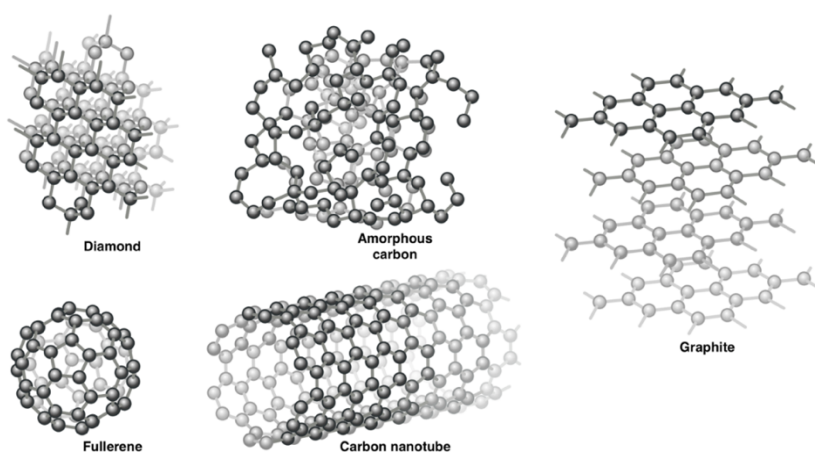


*Figure 3.2. Allotropes of Carbon*

## 3.2. Results

### 3.2.1. Photovoltaic performance

In this work we fabricate C-PSCs with a planar p-i-n architecture. Our goal is to understand the effect of carbon-based HTL-free structure in PSCs. A schematic representation of the C-PSC applied in this work is shown in Figure 3.3a, and the energy level diagram of the corresponding device is presented in Figure 3.3b. The cell is prepared fully at low temperature. As described in section 5.2 (methodology), complete solar cells were fabricated with the configuration FTO/c-TiO<sub>2</sub>/m-TiO<sub>2</sub>/perovskite/carbon.

Figure 3.3c shows the SEM cross-sectional image of our C-PSC. The thickness of the carbon electrode is observed to be approximately 11  $\mu\text{m}$ . Figure 3.3d is an enlarged image of the highlighted area in Figure 3.3c. The device has a configuration of glass/FTO/c-TiO<sub>2</sub>/m-TiO<sub>2</sub>/perovskite/carbon, where carbon functions as the counter electrode layer. The thicknesses of c-TiO<sub>2</sub>, m-TiO<sub>2</sub>, perovskite are 50 nm, 110 nm, and 450 nm, respectively.

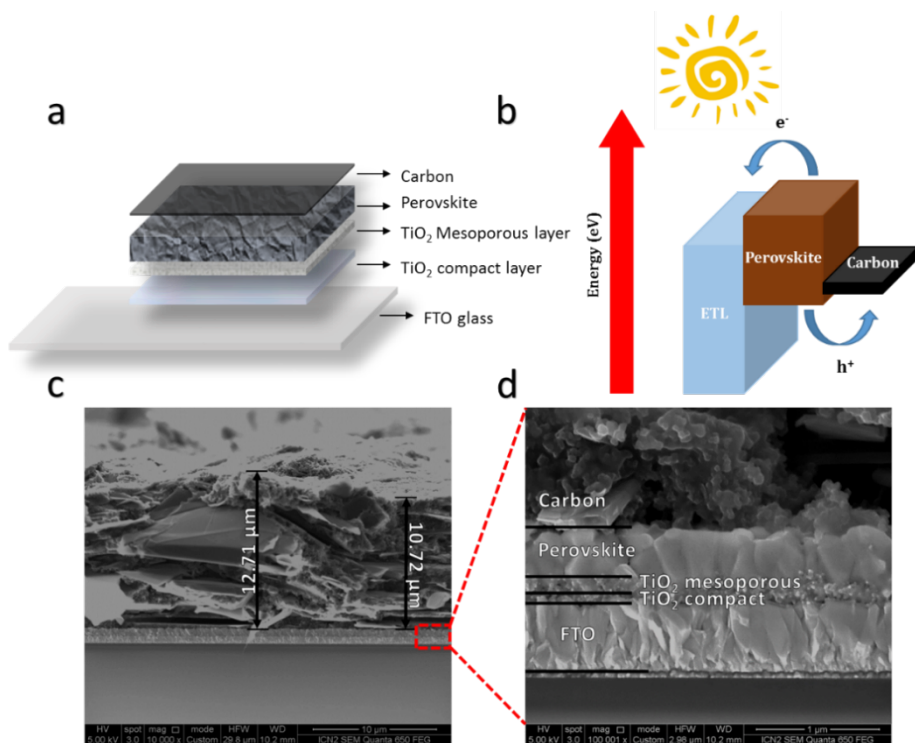


Figure 3.3. Schematics of (a) device and (b) the corresponding energy level diagram (c) The cross-sectional SEM image of the perovskite solar cell. (d) Magnification image of the highlighted rectangle area in figure (c).

We demonstrate the efficient use of carbon as a back contact electrode material in PSCs of planar p-i-n architecture (back contact electron harvesting). This architecture can be fabricated into highly crystalline perovskite films, as used here, and has great potential to achieve good stabilities [20][21]. Therefore, HTL-free PSCs become popular as they abandon the superfluous use of additional p-type material to transport positively charged carriers and also greatly simplify the structure of the devices.

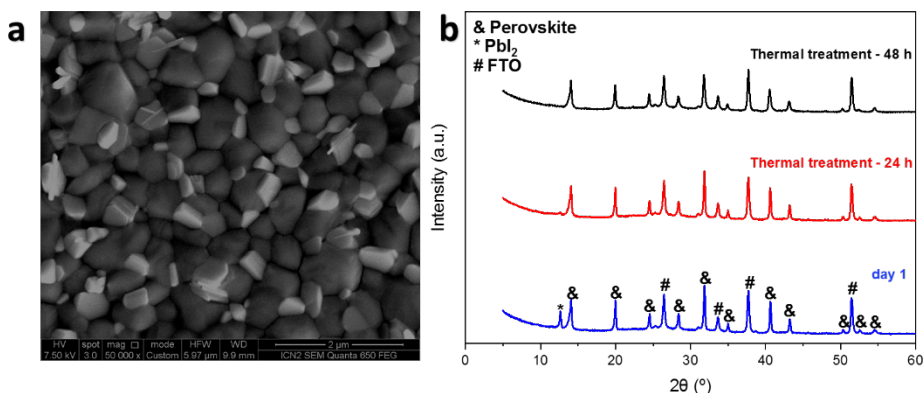


Figure 3.4. SEM images of top-view of (a) perovskite film, (b) X-ray diffraction patterns of perovskite films before and after thermal treatment.

As shown in Figure 3.4a, the grain size of the perovskite film varies between 300 and 400 nm. The Figure 3.4b shows the X-ray diffraction analysis of the samples showing good crystallinity. The variations of the structural properties of the perovskite of the PSCs because of the thermal stability test over time were sampled, acquiring XRD patterns after various stages of aging. The strong reflections on  $14.15^\circ$ ,  $20.02^\circ$ ,  $24.09^\circ$ ,  $28.46^\circ$ ,  $31.88^\circ$  and  $42.02^\circ$  are assigned to (110), (112), (202) (220), (310), and (224)/(400) respectively [22][23][24]. However, a weak diffraction peak of PbI<sub>2</sub> was observed at  $12.69^\circ$ , PbI<sub>2</sub> showed a slightly lower concentration as the samples continued to heat treatment [25].

To fabricate a carbon-based PSC, compact TiO<sub>2</sub>, mesoporous TiO<sub>2</sub>, and perovskite layers were processed using conventional methods that employ spiro-OMeTAD and Au, with the only difference that these last two films were replaced by carbon film. Here we used a commercial carbon paste (Dyename DN-CP01) that exhibits 10 ohms/square as sheet resistance even if treated at low temperature.

Carbon conductive paste, composed of graphite and carbon black, was deposited on the glass/FTO/c-TiO<sub>2</sub>/m-TiO<sub>2</sub>/perovskite film using a screen-printing method to form a 11 μm-thick carbon electrode Figure 3.3a. The first test that was carried out was to find the optimum temperature for annealing the carbon to eliminate the solvents from the paste, they worked with four different temperatures at 120 °C, recommended by the technical data sheet of the carbon paste [13][1], the rest of 130 °C, 140 °C and 150 °C, respectively. Figure 3.5 shows the photovoltaic results of the different temperatures used for the annealing of the carbon paste. For the temperature of 140 °C, the PCE of the devices decreases in comparison of the devices below temperatures of 130 °C, where it can be observed that the maximum efficiency is presented, obtaining an average of ~12% (See Figure 3.5d). The carbon layer leads to a decrease in the short circuit current density ( $J_{sc}$ ) of the device as the carbon annealing temperature increases (See Figure 3.5c). However, it has little effect on the open circuit voltage ( $V_{oc}$ ) of the device as can be seen in Figure 3.5b. Therefore, the temperature with the best results is 130 °C, the performance of the device can reach the optimum level. The device exhibits  $J_{sc}$  of 19.78 mA·cm<sup>2</sup>,  $V_{oc}$  of 1,009 V and fill factor (FF) of 61.71%, resulting in a PCE of 12.32%. In other words, high temperatures are not optimal for devices, since perovskite could be presenting changes in its structure, with the appearance of a pinholes.

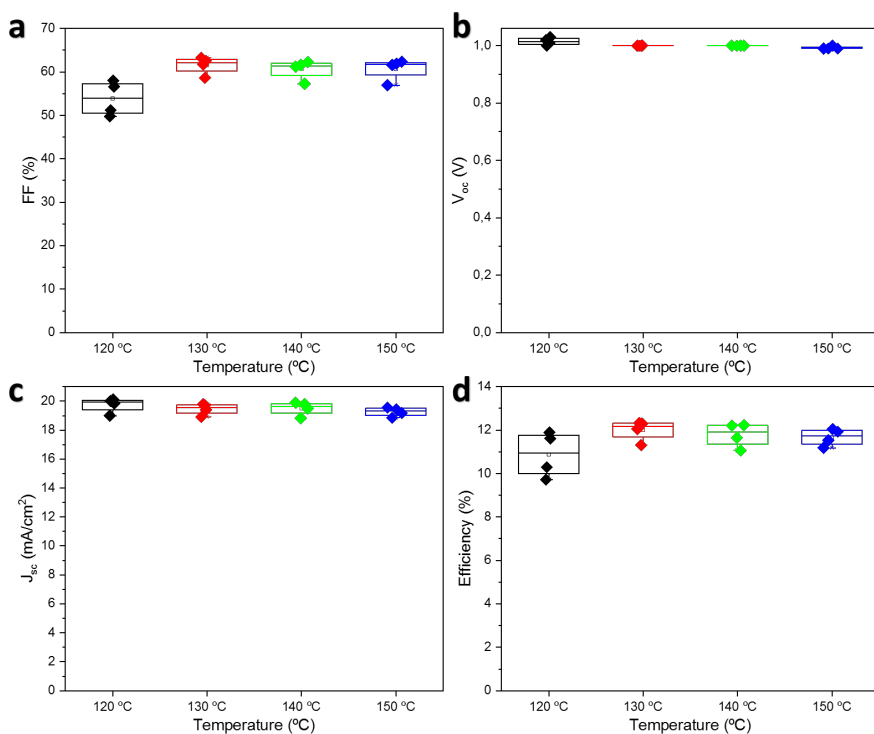


Figure 3.5. Statistics of the optoelectronic properties of the thermally treated PSCs: a, FF b,  $V_{oc}$ , c,  $J_{sc}$ , and d, efficiency.

### 3.2.2. Device stability

Next, we study the effect of thermal and humidity stress. The C-PSC devices were prepared with carbon annealing at 130 °C, to have devices with the best efficiencies. The C-PSC were kept in the dark at 45°C with a constant low RH. Samples were analysed without encapsulation. These devices were compared with samples without and with thermal treatment, and the untreated samples were kept at room temperature (25 °C). Figure 3.6a presents the comparison of the efficiency observed for the C-PSCs devices with and without treatment. The results revealed a notable improvement in thermal stability when the devices are stored at controlled temperature and

humidity. The extracted parameters of the cells with the best results are shown in Table 3-2. For the temperature-treated device,  $V_{OC}$  of 1.04 V,  $J_{SC}$  of 20.37 mA/cm<sup>2</sup> and FF of 66.70% are achieved, which results in a PCE of 14.15%. However, the untreated device only exhibits the  $J_{SC}$  of 18.91mA/cm<sup>2</sup>,  $V_{OC}$  of 1.02 V and FF of 64.23% and PCE of 12.30% is achieved. Obviously, treated devices lead to substantial increases in  $J_{SC}$ ,  $V_{OC}$  and FF. As shown in Figure 3.6b the device with the heat treatment obviously shows good stability after 8 days. The PCE of the device without treatment did not show considerable improvement, maintaining stable efficiency, otherwise, the treated device increased and remained considerably higher compared to the non-treated device.

Table 3-2. Photovoltaic parameters derived from J–V measurements of devices with and without treatment.

Champion device	PCE (%)	Jsc(mA/cm <sup>2</sup> )	Voc(V)	FF (%)
Without-treatment	12.62	18.91	1.01	65.73
With-treatment	14.15	20.37	1.04	66.70

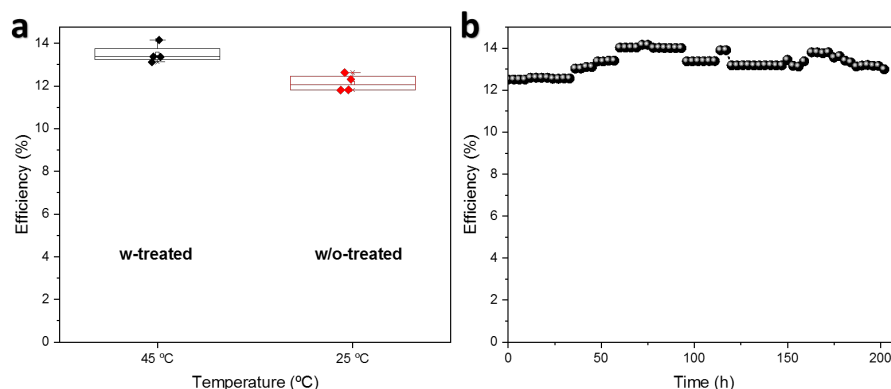


Figure 3.6. (a) PCE measured at different temperatures for PSCs with and without treatment and (b) Stability test carried out to the best device at 45 °C in the Dark for 100 h.



Therefore, the use of carbon as a back electrode is a feasible strategy for obtaining high-efficiency and stable PSCs. To study the impact mechanism of temperature and humidity on the performance of PSCs, devices without and with HTL were compared, keeping the devices under thermal and humidity stress of 45 °C and 65%, respectively. The initial PV parameters of the HTL and HTL-free devices are shown in Table 3-3. The treated C-PSC and PSC presented a PCE of 14.05% and 12,50%, respectively (Figure 3.7a), both compositions present considerable efficiency changes, being the sample without HTL the one with the highest PCE achieved under forward scanning. On the other hand, FF is quite low compared to standard PSCs using HTL and Au back electrode. The use of interlayers is a possible way to improve proper charge extraction from the carbon electrode [26][27][28].

*Table 3-3. Photovoltaic parameters derived from J - V measurements of devices with and without HTL, measurements before treatment.*

<b>Champion device</b>	<b>PCE (%)</b>	<b>Jsc(mA/cm<sup>2</sup>)</b>	<b>Voc(V)</b>	<b>FF (%)</b>
<b>With HTL</b>	17.99	21.98	1.04	78.13
<b>Without HTL</b>	12.30	18.77	1.02	64.23

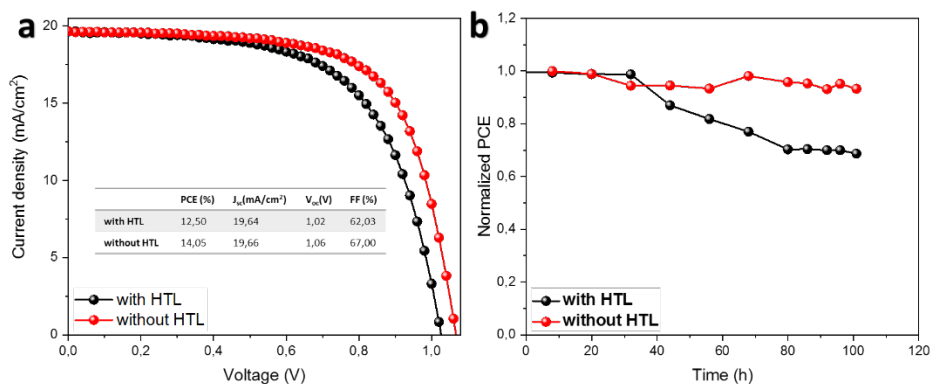


Figure 3.7. (a) J-V curves acquired under reverse polarization scanning of the best devices without HTL and with HTL after thermal treatment and (b) Thermal stress test performed on HTL-free PSC compared to device with HTL, structures without encapsulation.

The highlight of the comparison did not focus on the efficiencies, the thermal stability test has been carried out following the same experimental conditions reported previously, to compare the performance of the devices with and without HTL. Clearly the device without HTL shows a superior stability while the device with HTL shows a low stability, Figure 3.7b shows the trends of the PCE of the devices exposed to 45 °C with 65% humidity and in the dark. Devices without HTL remained approximately 90% after 100 h, on the contrary, the device with HTL after approximately 30 h, the performance was less than 60%, revealing a crucial instability factor in PSC technology operating at temperatures high levels that are related to the Au of the counter electrode that migrates through the entire structure of the solar cell and interacts with perovskite and the degradation of Spiro-OMeTAD, causing a drastic loss of solar cell performance [29][30].

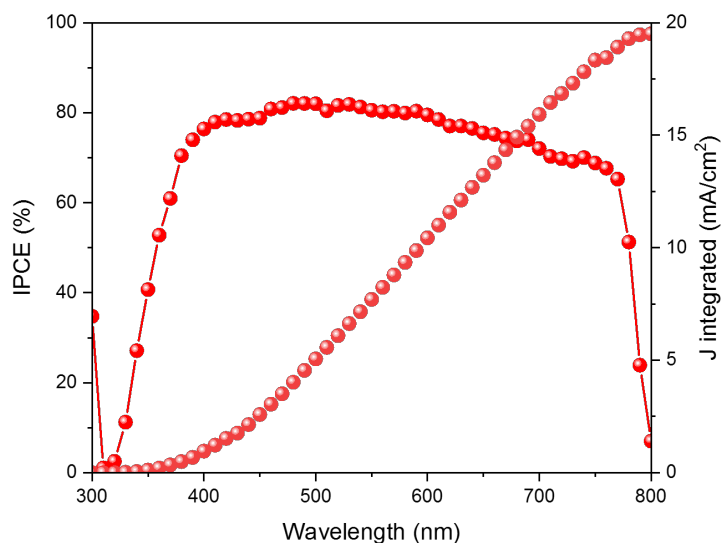


Figure 3.8. Incident photon-to-electron conversion efficiency (IPCE) spectra of C-PSCs.

We also measure the IPCE analysis. The spectra of the champion device without HTL is shown in Figure 3.8. We integrated the current density in a spectral range from 300 to 800 nm, obtaining 20,37 mA/cm<sup>2</sup> from the device. The integrated value from IPCE were comparable to the current densities obtained from the J-V curves, 20.09 mA/cm<sup>2</sup> for the cell. We obtained good reproducibility of photovoltaic parameters, with an average efficiency close to 13%. Photovoltaic parameters of the devices are shown in Figure 3.9.

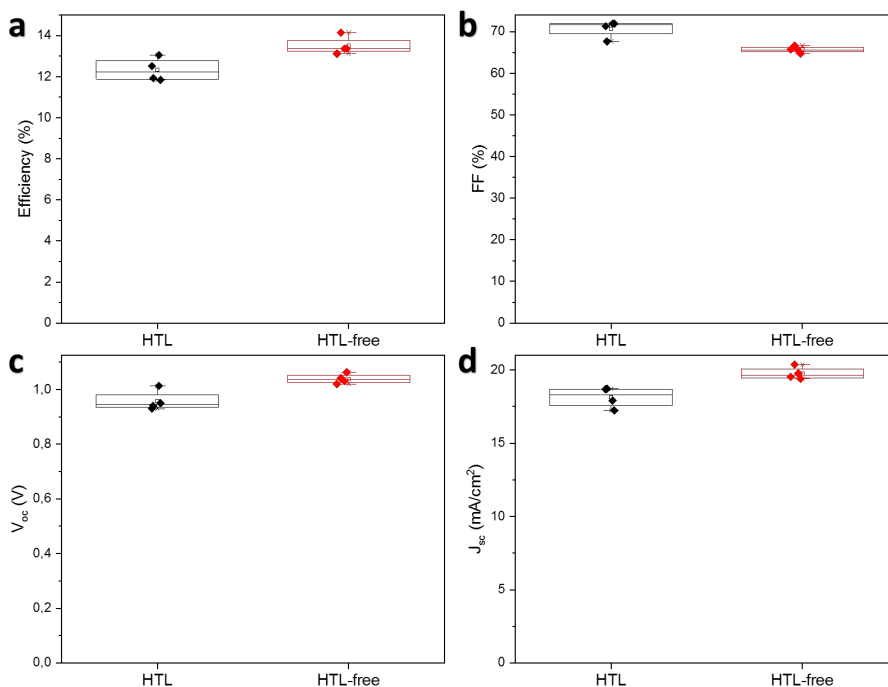


Figure 3.9. Statistics of the optoelectronic properties of PSCs with and without thermally treated HTL: a, FF b,  $V_{OC}$ . c,  $J_{SC}$ . and d, efficiency.

In particular, all PSCs exposed to the same extrinsic factors under thermal tests in terms of temperature and humidity. Based on the presented results, we can formulate an evolution of the time scale of the intrinsic factors in progress that affect performance under temperature (45 °C) and exposure to moisture. Two degradation stages can be proposed, the first part is dominated by the diffusion of I<sup>-</sup> and Au, and the second occurs during a time scale of only 30 h in which the diffusion of gold and the degradation of Spiro-OMeTAD were avoided by using a non-metallic hydrophobic top contact, like printable carbon. Therefore, in this region the degradation is dominated by iodide diffusion. This approach allows reaching a maximum temperature of 45 °C for about 60-100 hours. For a

temperature longer than 45 °C, iodide diffusion is limited or even prevented by passivating the boundaries of the perovskite grains. Of course, this degradation time scale can be extended by completely removing the presence of moisture during heat stress. In this case, the stability test should be performed in a N<sub>2</sub> environment or by applying an effective sealing procedure against moisture and oxygen permeability. However, mixed compositions, chemical doping and crystal crosslinking have been shown to be strategies that have shown promise for improving device stability [31][32].

### 3.3. Discussions

In this work a hole transport layer free structure is described in which we affirm that the elimination of the use of an HTM could improve stability, reduce costs, and increase the fabrication reproducibility of perovskite solar cells. A depletion region was observed in these perovskite solar cells without an HTL, shedding light on its mechanism, and a high open-circuit voltage was demonstrated even without an HTL. However, it is still necessary to improve the PCEs of the C-PSCs to maintain or improve their competitiveness. The effect of introducing the devices in thermal and humidity stress was investigated by analysing the performance and stability of PV. Improvements in hysteresis suppression have been found, leading to increased production of stabilized PSCs and the perovskite adsorbent exhibited properties that improve stability under temperature and humidity stress. These results based on the electrical characterizations and morphologies in devices. In fact, after 100 h of thermal testing the devices retained 90% compared to

the standard structure which had a loss of 60% after 30 h. From a technological point of view, this structure of C-PSCs has an even greater potential long-term impact than the "standard" configuration implied by the HTM. The possibility of fabrication solar cells without HTL and achieving a high photovoltaic effect, the performance is interesting and important. C-PSCs have potential to be explored, promoting carbon film innovation strategies such as interfaces, additive engineering, passivation, stability, etc., which would make C-PSCs more valuable potential and serious rival for the PSCs that employ HTL and the counter electrode.

### 3.4. References

- [1] E. Calabrò *et al.*, “Easy Strategy to Enhance Thermal Stability of Planar PSCs by Perovskite Defect Passivation and Low-Temperature Carbon-Based Electrode,” *ACS Appl. Mater. Interfaces*, vol. 12, no. 29, pp. 32536–32547, Jul. 2020.
- [2] H. Chen and S. Yang, “Carbon-Based Perovskite Solar Cells without Hole Transport Materials: The Front Runner to the Market?,” *Advanced Materials*, vol. 29, no. 24. Wiley-VCH Verlag, p. 1603994, Jun-2017.
- [3] M. Lira-Cantu, “The future of semiconductor oxides in next-generation solar cells,” *Met. Oxides Ser.*, 2018.
- [4] Q.-Q. Chu *et al.*, “Highly stable carbon-based perovskite solar cell with a record efficiency of over 18% via hole transport engineering,” *J. Mater. Sci. Technol.*, vol. 35, no. 6, pp. 987–993, 2019.
- [5] B. Saparov and D. B. Mitzi, “Organic–Inorganic Perovskites: Structural Versatility for Functional Materials Design,” *Chem. Rev.*, vol. 116, no. 7, pp. 4558–4596, Apr. 2016.
- [6] Nrel, “National Renewable Energy Laboratory (NREL) Home Page,” 2006. [Online]. Available: <https://www.nrel.gov/>. [Accessed: 28-Aug-2018].
- [7] K. Domanski *et al.*, “Not All That Glitters Is Gold: Metal-Migration-Induced Degradation in Perovskite Solar Cells,” *ACS Nano*, vol. 10, no. 6, pp. 6306–6314, Jun. 2016.
- [8] T. Leijtens, G. E. Eperon, S. Pathak, A. Abate, M. M. Lee, and H. J. Snaith, “Overcoming ultraviolet light instability of sensitized TiO<sub>2</sub> with meso-superstructured organometal tri-halide perovskite solar cells,” *Nat. Commun.* 2013 41, vol. 4, no. 1, pp. 1–8, Dec. 2013.
- [9] Z. Ku, Y. Rong, M. Xu, T. Liu, and H. Han, “Full Printable Processed Mesoscopic CH<sub>3</sub>NH<sub>3</sub>PbI<sub>3</sub>/TiO<sub>2</sub> Heterojunction Solar Cells with Carbon Counter Electrode,” *Sci. Reports* 2013 31, vol. 3, no. 1, pp. 1–5, Nov. 2013.
- [10] S. N. Vijayaraghavan, J. Wall, L. Li, G. Xing, Q. Zhang, and F. Yan, “Low-temperature processed highly efficient hole transport layer free carbon-based planar perovskite solar cells with SnO<sub>2</sub> quantum dot electron transport layer,” *Mater. Today Phys.*, vol. 13, p. 100204, Jun. 2020.
- [11] Y. Yang *et al.*, “High performance carbon-based planar

- perovskite solar cells by hot-pressing approach," *Sol. Energy Mater. Sol. Cells*, vol. 210, p. 110517, Jun. 2020.
- [12] N. Cheng *et al.*, "Application of mesoporous SiO<sub>2</sub> layer as an insulating layer in high performance hole transport material free CH<sub>3</sub>NH<sub>3</sub>PbI<sub>3</sub> perovskite solar cells," *J. Power Sources*, vol. 321, pp. 71–75, Jul. 2016.
  - [13] V. Babu *et al.*, "Improved Stability of Inverted and Flexible Perovskite Solar Cells with Carbon Electrode," *ACS Appl. Energy Mater.*, vol. 3, no. 6, pp. 5126–5134, Jun. 2020.
  - [14] Y. Rong *et al.*, "ARTICLE Synergy of ammonium chloride and moisture on perovskite crystallization for efficient printable mesoscopic solar cells," *Nat. Publ. Gr.*, 2017.
  - [15] F. Meng *et al.*, "Current progress in interfacial engineering of carbon-based perovskite solar cells," *J. Mater. Chem. A*, vol. 7, no. 15, pp. 8690–8699, Apr. 2019.
  - [16] Q. Wang, N. Phung, D. Di Girolamo, P. Vivo, and A. Abate, "Enhancement in lifespan of halide perovskite solar cells," *Energy Environ. Sci.*, vol. 12, no. 3, pp. 865–886, Mar. 2019.
  - [17] A. Mei *et al.*, "A hole-conductor-free, fully printable mesoscopic perovskite solar cell with high stability," *Science (80-. )*, vol. 345, no. 6194, pp. 295–298, 2014.
  - [18] H. Wang, X. Hu, and H. Chen, "The effect of carbon black in carbon counter electrode for CH<sub>3</sub>NH<sub>3</sub>PbI<sub>3</sub>/TiO<sub>2</sub> heterojunction solar cells," *RSC Adv.*, vol. 5, no. 38, pp. 30192–30196, Mar. 2015.
  - [19] R. Hu, L. Chu, J. Zhang, X. Li, and W. Huang, "Carbon materials for enhancing charge transport in the advancements of perovskite solar cells," *J. Power Sources*, vol. 361, pp. 259–275, Sep. 2017.
  - [20] H. Ye *et al.*, "17.78% efficient low-temperature carbon-based planar perovskite solar cells using Zn-doped SnO<sub>2</sub> electron transport layer," *Appl. Surf. Sci.*, vol. 478, pp. 417–425, Jun. 2019.
  - [21] V. Ferguson, S. R. P. Silva, and W. Zhang, "Carbon Materials in Perovskite Solar Cells: Prospects and Future Challenges," *Energy Environ. Mater.*, vol. 2, no. 2, pp. 107–118, Jun. 2019.
  - [22] W. Zhang *et al.*, "Thermal Stability-Enhanced and High-Efficiency Planar Perovskite Solar Cells with Interface Passivation," *ACS Appl. Mater. Interfaces*, vol. 9, no. 44, pp. 38467–38476, Nov. 2017.
  - [23] J. J. Jin *et al.*, "Efficient and stable flexible perovskite solar cells



- based on graphene-AgNWs substrate and carbon electrode without hole transport materials,” *J. Power Sources*, vol. 482, p. 228953, Jan. 2021.
- [24] X. Guo, C. McCleese, C. Kolodziej, A. C. S. Samia, Y. Zhao, and C. Burda, “Identification and characterization of the intermediate phase in hybrid organic–inorganic MAPbI<sub>3</sub> perovskite,” *Dalt. Trans.*, vol. 45, no. 9, pp. 3806–3813, Feb. 2016.
  - [25] Z. Liu, J. Li, and F. Yan, “Package-Free Flexible Organic Solar Cells with Graphene top Electrodes,” *Adv. Mater.*, vol. 25, no. 31, pp. 4296–4301, Aug. 2013.
  - [26] Z. Liu *et al.*, “15% efficient carbon based planar-heterojunction perovskite solar cells using a TiO<sub>2</sub>/SnO<sub>2</sub> bilayer as the electron transport layer,” *J. Mater. Chem. A*, vol. 6, no. 17, pp. 7409–7419, May 2018.
  - [27] T. Zhang *et al.*, “Stable and Efficient 3D-2D Perovskite-Perovskite Planar Heterojunction Solar Cell without Organic Hole Transport Layer,” *Joule*, vol. 2, no. 12, pp. 2706–2721, Dec. 2018.
  - [28] S. Bhandari, A. Roy, A. Ghosh, T. K. Mallick, and S. Sundaram, “Performance of WO<sub>3</sub>-Incorporated Carbon Electrodes for Ambient Mesoscopic Perovskite Solar Cells,” *ACS Omega*, vol. 5, no. 1, pp. 422–429, Jan. 2019.
  - [29] S. Maniarasu, T. B. Korukonda, V. Manjunath, E. Ramasamy, M. Ramesh, and G. Veerappan, “Recent advancement in metal cathode and hole-conductor-free perovskite solar cells for low-cost and high stability: A route towards commercialization,” *Renew. Sustain. Energy Rev.*, vol. 82, pp. 845–857, Feb. 2018.
  - [30] R. He, X. Huang, M. Chee, F. Hao, and P. Dong, “Carbon-based perovskite solar cells: From single-junction to modules,” *Carbon Energy*, vol. 1, no. 1, pp. 109–123, Sep. 2019.
  - [31] H. SN, L. T, E. GE, S. SD, N. RJ, and S. HJ, “Enhanced Hole Extraction in Perovskite Solar Cells Through Carbon Nanotubes,” *J. Phys. Chem. Lett.*, vol. 5, no. 23, pp. 4207–4212, Dec. 2014.
  - [32] S. N. Habisreutinger, R. J. Nicholas, and H. J. Snaith, “Carbon Nanotubes in Perovskite Solar Cells,” *Adv. Energy Mater.*, vol. 7, no. 10, p. 1601839, May 2017.

# Chapter 4: Ferroelectric oxide/Halide Perovskite Solar Cells

---

## 4.1. Introduction

Oxides have played a key role in the development of emerging photovoltaic technologies in various capacities such as selective charge transport layers, interfacial layers, or photoabsorbers. In the previous decade, interest in transition metal oxides grew enormously for their application in photovoltaic energy due to their properties and high stability if compared to classical organic semiconductors [1][2][3][4][5][6]. However, defects in these oxides, such as oxygen vacancies ( $O_{vac}$ ), act as recombination centers and, in air and ultraviolet light, reduce the stability of the solar cell. Among these oxides, ferroelectric oxides attract the most interest due to their ability to utilize spontaneous polarization in a process called polarization-assisted charge separation [7], in addition to their likely role in improving the stability of solar cells [8]. Most technologically important ferroelectrics are oxides with a perovskite structure. The magnitude of the built-in electric field in a ferroelectric material is about one to two orders of magnitude greater than in a semiconductor p-n junction [9][7], and the width of the field spans the entire ferroelectric material and not just the junction [7][10], which facilitates the separation of e-h pairs. It has

been recently demonstrated that the build-in electric field at the oxide-active layer junction can be enhanced by ferroelectric oxides causing more charges to separate in solar cells, significantly improving the PCE of the device [7][11]. Indeed, many perovskite materials have good ferroelectricity, among them oxides like  $\text{BaTiO}_3$  [12],  $\text{BiFeO}_3$  [13]. Ferroelectric materials exhibit spontaneous polarization due to the non-centimetry of the crystallographic unit cell, and have been widely employed in fields including field-effect transistors [15][16], non-volatile memories [17][18][19], memristors, and synapse [20][21][22]. The coupling of ferroelectricity and the photovoltaic effect was envisioned 41 years ago by Fridkin, who studied a "photoferroelectric crystal" for a potential solar cell [23]. Since then, photoferroelectric devices have attracted the attention of researchers. Subsequently, photoferroelectric devices were developed using mainly perovskite materials. Nowadays, oxide perovskites with a band gap of  $<3$  eV, such as  $\text{BiFeO}_3$  [24],  $\text{BiMnO}_3$  [24] and  $\text{Bi}_2\text{FeCrO}_6$  [25], have attracted much more attention for the development of new and stable PSCs; In particular,  $\text{BiFeO}_3$ -based materials have been widely investigated due to their toxic-free components. Out of these large number of oxides, Bismuth Ferrite  $\text{BiFeO}_3$  (BFO) has always attracted greater attention due to its multifunctional properties [26][27][28]. BFO is one of the few single-phase multiferroic materials that has (anti)ferromagnetic and ferroelectric properties at room temperature. Therefore, it has had a major impact on the field of multiferroics [29][30][31]. There exists several studies on compositional engineering, architecture of devices which use BFO as their focus of the study as transport layer or main absorber in solar

cells [32][33][34]. On the other hand, Halide Perovskite Solar Cells (PSCs) research has taken a great leap and is almost competing monocrystalline Silicon with a record efficiency of 25.2% [35]. However, in studies where BFO has been combined with halide perovskites it did not seem to be a suitable match, evident from the performance parameters in existing literatures [36][37][38]. For example, Shirahata et. al. demonstrated a maximum PCE of 0.112% with a  $J_{sc}$  of 0.483 mA/cm<sup>2</sup>,  $V_{oc}$  of 0.621 V and 37.4% fill factor. Bismuth Ferrite, is a room temperature multiferroic oxide with a perovskite (ABX<sub>3</sub>) crystal structure belonging to the space group of R3c, which is the rhombohedral phase (See Figure 4.1a) [39]. It has high Curie temperature (TC) of 1100K. The ferroelectric polarisation has been demonstrated before to occur along the pseudocubic direction (111) with a polarisation value of 90-95  $\mu\text{C}/\text{cm}^2$ , which is typically a high value of polarisation compared to other ferroelectrics [40][41]. However, this value is not a constant and it varies depending upon the preparation methods, exact chemical composition, processing conditions etc. BFO is also different from conventional non-centrosymmetric ferroelectrics because of the origin of the ferroelectricity. "Stereo active ferroelectricity" in BFO is a result of polarization caused by the lone pair ( $s^2$  orbital) of Bi<sup>3+</sup>, so that the polarization comes mostly from the A site while the magnetization comes from the B site (Fe<sup>3+</sup>). On the contrary, in conventional non-centrosymmetric ferroelectrics the polarisation is mainly rooted to the off centering of the B site cation leading to the shift of charge centre. The optical bandgap of BFO normally lies in the range of 2.4-2.8 eV, considering the theoretical and experimental values [42][43]. Thus BFO exhibits both photoconductivity and

photovoltaic effects [24][44]. Owing to these multifunctional properties, combined with the stability, inherent property of these oxides to get photodoped and with an aim to improve the existing efficiency and stability in the literature, we considered to pursue the experiments.

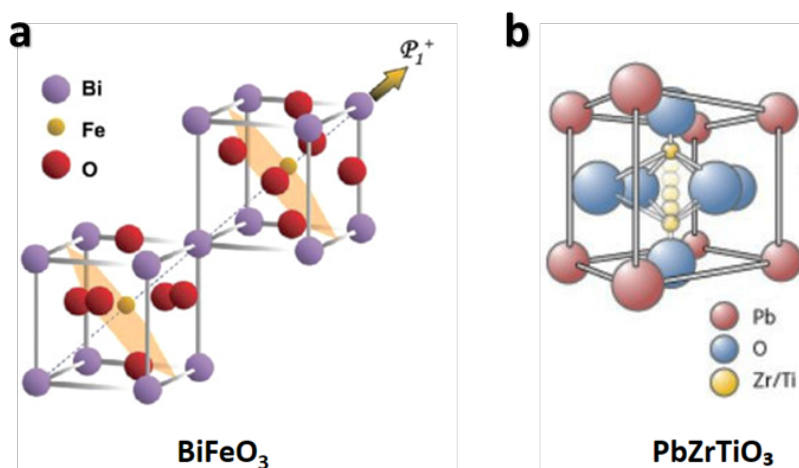


Figure 4.1. (a) Structure of the PZT and (b) Rhombohedral ( $R3c$ ) structure of  $\text{BiFeO}_3$ .

In our laboratory, we have applied ferroelectric oxides such as  $\text{Pb}(\text{Zr}_x\text{Ti}_{1-x})\text{O}_3$  ( $x = 0.6$ ), PZT (See Figure 4.1b) as the electron transport layer with the aim of eliminating the detrimental photocatalytic effect that classic semiconductor oxides, such as  $\text{TiO}_2$  or  $\text{SnO}_2$ , show under UV light. This photocatalytic effect is excellent for these materials working as photocatalysts; however, it has been shown to be detrimental for solar cells due to the degradation of the absorber material deposited on them. Our initial results have shown that PZT can indeed work as a transport layer after poling under UV light and external bias (See Figure 4.2b and c). Most important, PZT-based PSCs has shown to sustain harsh conditions of UV light, and

continuous light irradiation in air in comparison to PSCs applying  $\text{SnO}_2$  where PSC degradation is observed almost immediately as shown in Figure 4.2d.

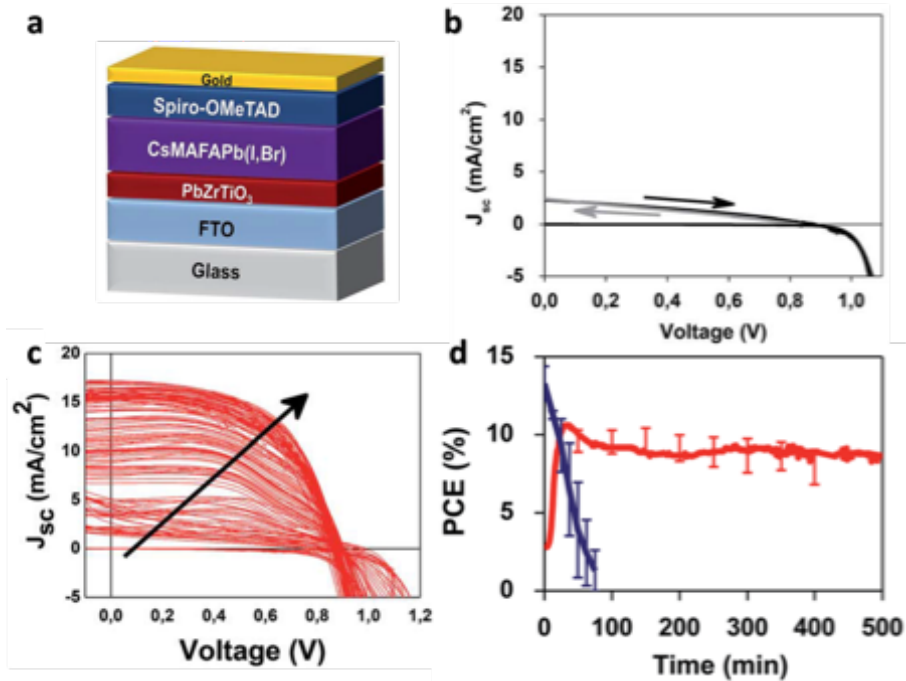


Figure 4.2. PZT-based perovskite solar cell. (a) schematics of the solar cells; (b) IV curves in reverse (black line) and forward (gray line) of the solar cell right after fabrication; (c) IV curves of the solar cell during poling under UV light and (d) stability.

The mentioned effect seems to be related to the relation between the ferroelectric properties of these oxides and  $O_{vac}$ . The low photoactivity shown by ferroelectric oxides under ultraviolet light makes them very attractive to improve the stability of PSCs. UV light can photoinduce remanent polarization enhancement, as recently reported for PbZrTiO<sub>3</sub> (PZT) films [45]. The formation of defect dipoles, responsible for charge separation and current transport, depends on the presence of defect charges ( $O_{vac}$ ). That is, instead of

acting as photoreactive sites as in  $\text{SnO}_2$  or  $\text{TiO}_2$ , the  $\text{O}_{\text{vac}}$  in PZT are removed after polarizing under ultraviolet light, increasing their transport properties [45], suggesting a different working mechanism favouring the stability of cells (See Figure 4.3).

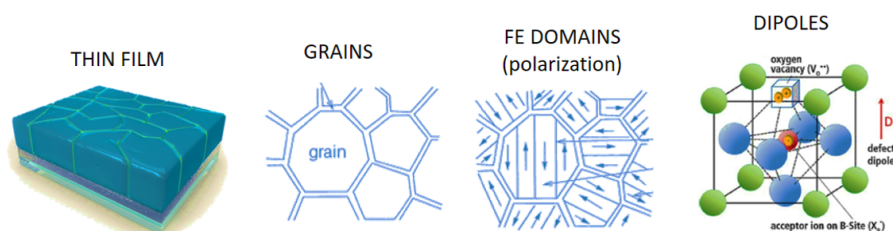


Figure 4.3. Relation between  $\text{O}_{\text{vac}}$  and ferroelectricity in PZT.

In this chapter, we study the effect of a BFO dense thin film acting as an ETL as a bilayer with a perovskite halide (HP) thin film absorber and investigate their effect on PSC performance and stability.

Evidence has shown that perovskite materials have photovoltaic properties, but also ferroelectric properties, offering a special system called photoferroelectric materials. A built-in electric field established in these materials due to the ferroelectric property is more useful for the separation of e-h pairs, improving the efficiency of energy conversion of the photovoltaic process in solar cells. As described in section device fabrication, complete solar cells were fabricated with the FTO/BFO/perovskite/Spiro-OMeTAD/Au configuration based on the multicational perovskite absorber with the nominal formula  $\text{Rb}_{0.05}\text{Cs}_{0.05}\text{MA}_{0.15}\text{FA}_{0.75}\text{Pb}_{1.05}(\text{I}_{0.95}\text{Br}_{0.05})_3$  ( $\text{RbCsMAFA}$ ). The BFO was prepared by solution processing applying different concentration of the BFO precursors. After giving a brief description of the structure and property of

photoferroelectric perovskite materials, the device structure, operating principles, and device characterization are introduced. Finally, a hypothesis of the operating mechanism of the oxide in conjugation with the perovskite halide was proposed.

## 4.2. Results

### 4.2.1. Synthesis and characterization of BFO

The synthesis of BFO was done by a simple sol-gel process (The synthesis is explained in detail in Materials and Methodology section; Chapter 5). The final solution extracted, as mentioned in chapter 5, was then further used for making the BFO transport layer and characterisation. The formation of the BFO was confirmed by XRD patterns, showing consistent peaks for the reflections that predominantly come from the (012), (110) and (024) planes for temperature and concentration optimization experiments. When using a fast-annealing technique for crystallization of the films between 475 °C and 625 °C in air, the reflections correspond to the BiFeO<sub>3</sub> perovskite, without noticeable second phases as shown in the XRD patterns in Figure 4.4a. Rapid heating in air to a temperature where the rhombohedral BFO is thermodynamically stable, between 447 °C and 767 °C, can prevent stabilization of the secondary phases in the film. This has been well established in the literature before [42]. The variation in the crystallization temperature, as shown in Figure 4.4a, does not show significant impacts on the crystallinity of the film, if it crystallizes in the range detailed above. Therefore, a temperature towards the lower limit of 500 °C, was chosen for our



experiments. The concentration of the precursor solution directly affects the phase and crystallinity of the BFO thin film. The BFO phase is not detected with concentrations of 0.05 M or below, as shown in Figure 4.4b. The BFO thin films were characterized in detail using atomic force microscopy (AFM) and SEM to study their surface morphology. The average surface roughness values were found to be around 4.5 nm when scanning multiple lines through the AFM image, while using SEM we ensured that we obtained smooth, non-porous, thin films. The AFM and SEM images are shown in Figure 4.4c and Figure 4.4d respectively.

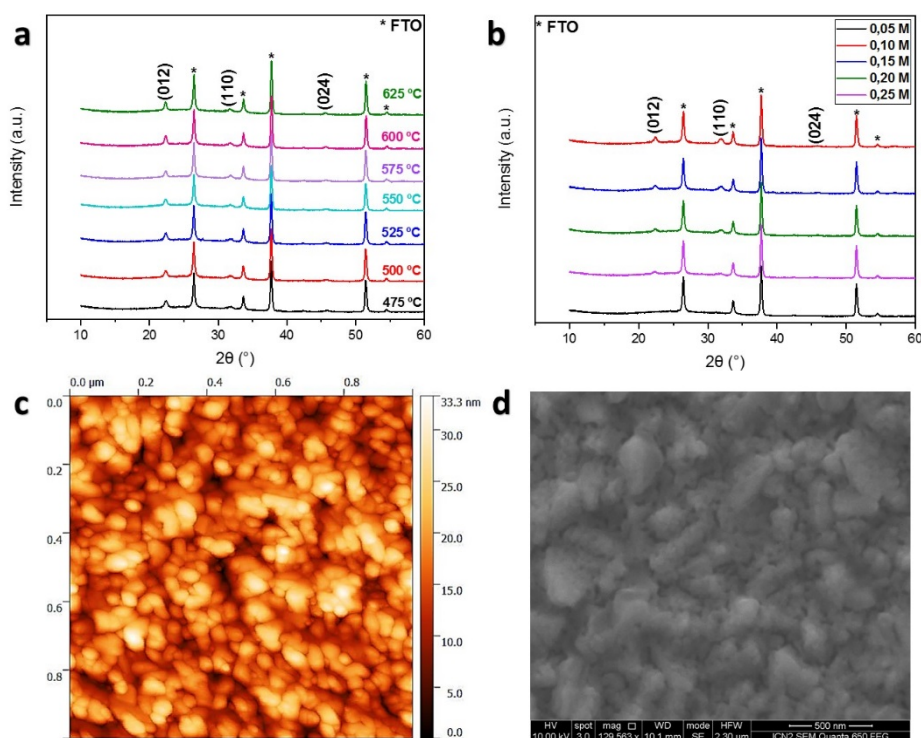


Figure 4.4. X-ray diffraction patterns for BFO thin films synthesized: a) at different temperatures (indicated above each pattern in units of Celsius); b) with different concentration of precursor solution. c) AFM image of a BFO thin film surface. d) surface SEM image of a BFO thin film.

To study the ferroelectric properties, BFO thin films grown on Platinum (Pt) substrates were subjected to a series of photo-response tests and hysteresis loop measurements under varying conditions such as dark or with illumination at room temperature or at 127K. The BFO thin films exhibited an  $V_{OC}$  and  $J_{SC}$  of -0.454 V and 0.03  $\mu A$  respectively at room temperature (RT) under illumination of a 408 nm laser without poling, while in the dark the film was unresponsive. The plots for room temperature and 124K conditions can be found in Figure 4.5a. The photo-response when the films were positively polarized with a bias of 11 V at room temperature under the same illumination as above, this photovoltaic output was calculated to be around 0.622%, with  $V_{OC}$  of -0.63V and  $J_{SC}$  of 1.53  $\mu A$ . The I-V curves for the sample are shown in the Figure 4.5b. The Low-temperature measurements of the BFO thin films showed better open-circuit voltages and much lesser short-circuit current, as expected due to lesser carrier mobility. The details are given in the Figure 4.5c.

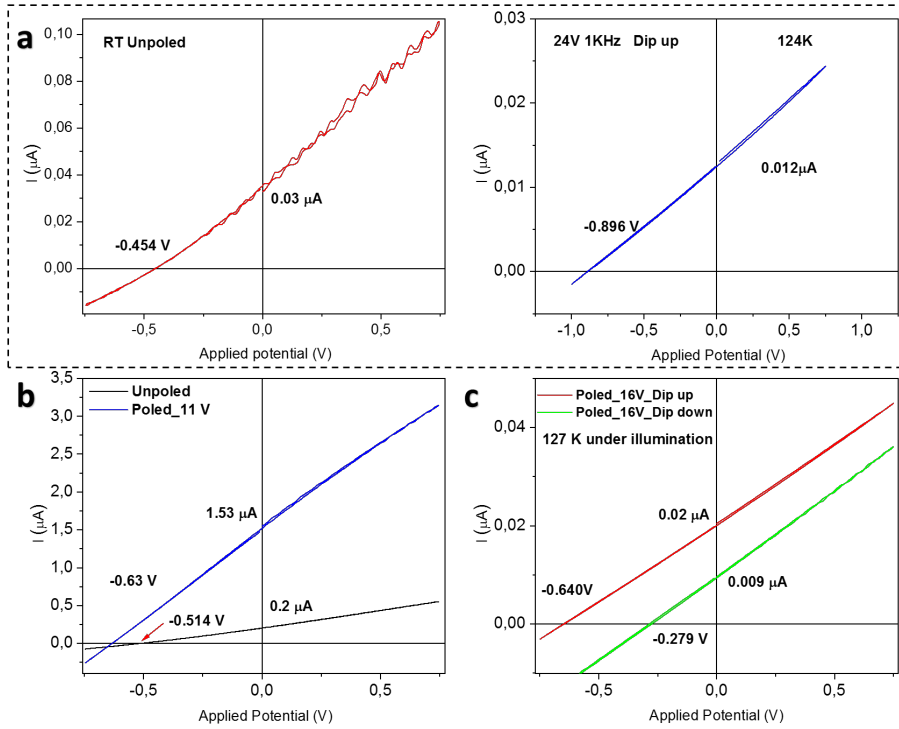


Figure 4.5. a) I-V curves of BFO in capacitor configuration unpoled at room temperature denoted by the red plot. The blue plot represents the I-V curve for the same capacitor at 124K and poled with 24 V. b) I-V curves of the capacitor configuration of BFO with Platinum under room temperature and illumination with and without poling, c) I-V curves of the same configuration at 127K under illumination.

Figure 4.6a and 4.6b show measurements of ferroelectric polarization vs. electric field (P-E) hysteresis loop of BFO thin film was measured at 1 kHz with sinusoidal voltage pulses at 125K. The remnant polarisation was found to be around  $43 \mu\text{C}/\text{cm}^2$ . The value is of the similar order as reported for epitaxial thin films [46]. The differences observed have been attributed to the differences in preparation methods, measurement conditions and thin film stoichiometry. The symmetry and shape of the hysteresis loop are indicators of the quality of the ferroelectric material [47]. Given those ferroelectric oxides are true insulators, the application of a

ferroelectric oxide (dielectric material) in a solar cell requires the film to be sufficiently thin enough, so it does not pose large series resistance and ensure that we get the desired ferroelectric properties in the film. The 0.1 M precursor concentration gave the optimum results when the BFO/Perovskite heterojunctions were illuminated with AM 1.5G irradiation and poling.

The direct bandgap of the synthesised BFO was found around 2.66 eV as evident from the Tauc plot in Figure 4.6c. Interestingly, when the thin films were put in a sandwiched capacitor configuration as, FTO/BFO/Au and four-point conductivity was measured under AM 1.5G solar irradiation, the conductivity almost tripled when compared to its conductivity in dark, while it almost increases 1.5 times when compared to its initial value under irradiation and bias as evident from Figure 4.6d. It is noteworthy that the increasing conductivity saturates as we keep on increasing the bias.

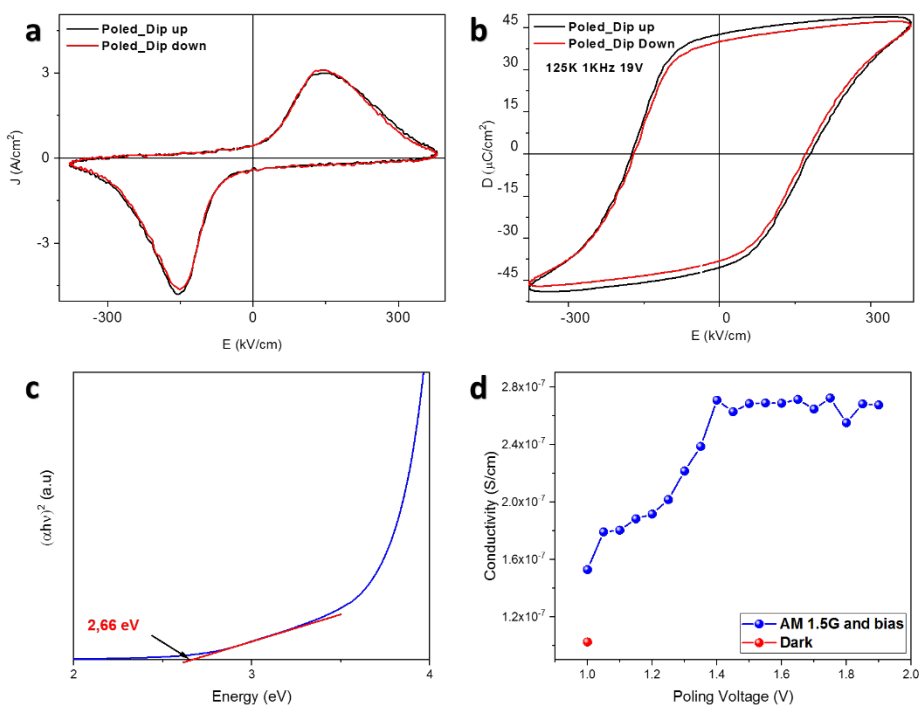


Figure 4.6. a) Experimental charge current hysteresis  $J$  vs.  $E$ , loops measured in the film without (black) and with illumination (red) at 125 K. d) Polarization hysteresis  $P$  vs.  $E$  loops calculated by the integration of the  $J$ - $E$  loops. c) Tauc plot showing the direct bandgap of BFO. d) Conductivity changes of BFO thin film under AM 1.5G solar irradiation and increasing poling bias

For a detailed insight into the actual chemical composition, X-ray photoelectron spectroscopy (XPS) was performed on BFO thin films on top of FTO substrate. The XPS survey scan and scans for Bi4f, Fe2p, O1s are shown in Figure 4.7. The core level scans (carbon correction of 0.6eV for C at 285.4 eV) for Bi4f shows peaks at 159 eV for Bi4f<sub>7/2</sub> which hints a +3 oxidation state. The relatively difficult to confirm Fe2p showed clear indications of an expected +3 state. The +2 and +3 oxidation states are characterised by their satellite peak features. Fe(III) compounds are always high-spin species, leading to complex multiplet-split Fe2p spectra, similar to the ones reported here and also in the literature [48]. Additionally, the O1s spectra

corresponds to the  $-2$  state of Oxygen for metal oxides with a negligible percentage of carbonate formation, evident from a little hump near the 531.5-532 eV range. Correlating these findings with the XRD patterns, it is conclusive that we get the desired BFO phase and not a mixture of phases, which is essential for our application in solar cell.

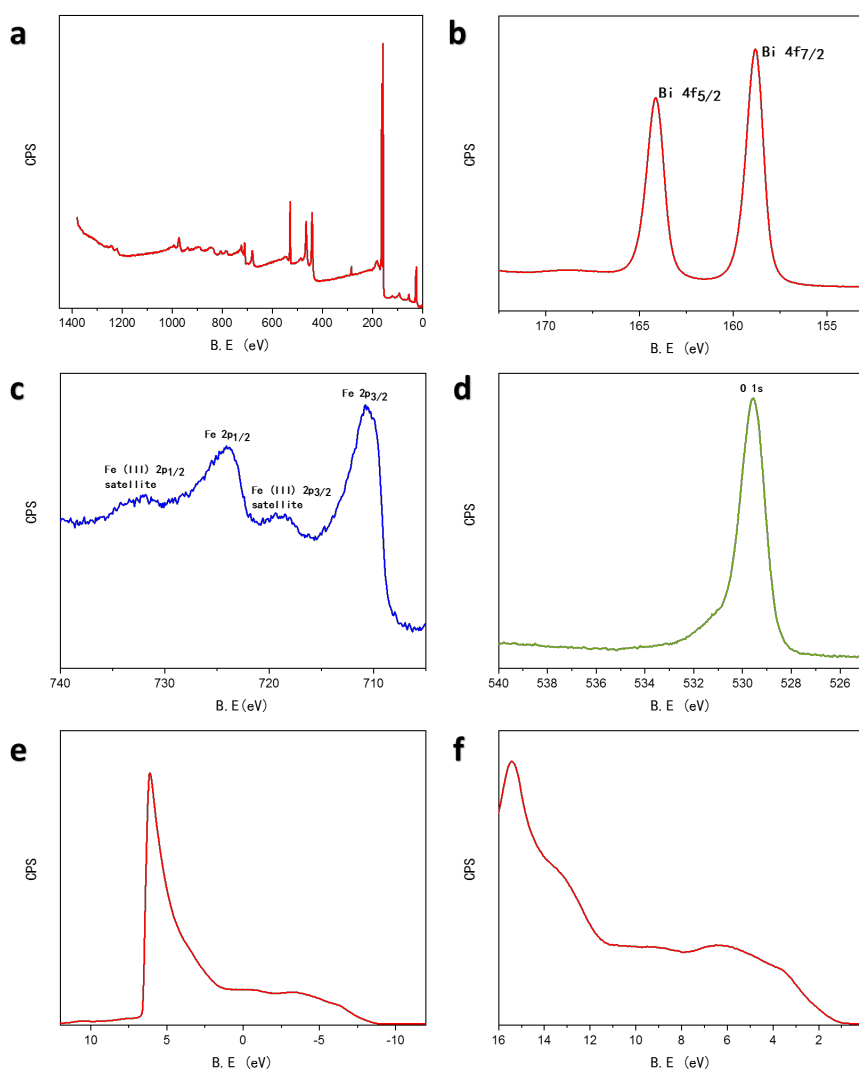


Figure 4.7. XPS and UPS of BFO thin films on FTO substrate, a) Survey Scan, b) Bismuth peaks, c) Iron peaks, d) Oxygen peak, e) Work Function Spectra, f) Valence Band spectra.

#### 4.2.2. Photovoltaic response of PSCs with BFO as ETL

The solar cells were manufactured with the architecture (FTO/BFO/perovskite/spiro-OMeTAD/Au) shown in Figure 4.8a. The devices were manufactured with different concentrations of BFO to see the photovoltaic performance, presenting a higher efficiency the device with a concentration of 0.1 M of BFO compared to the rest of the devices, as can be seen in the Figure 4.8b.

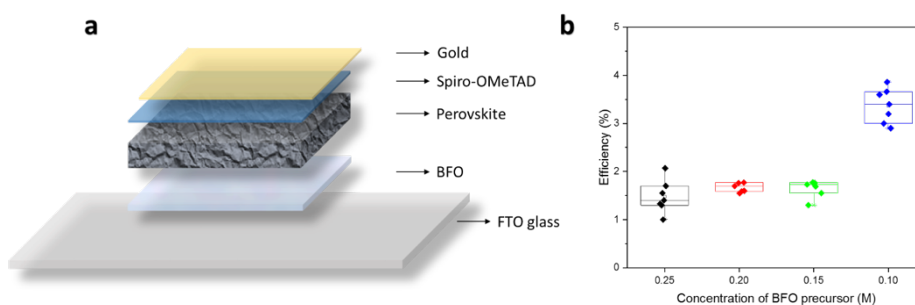


Figure 4.8. a) Schematic diagram of the solar cell. b) Corresponding statistics for each concentration for 7 devices of each concentration.

Figure 4.9(a-d) shows cross-sectional SEM images of typical BFO solar cells, where the thickness of the BFO layers can be seen at different concentrations. The mean thickness of the BFO layer with a BFO precursor concentration of 0.1 M was calculated at  $41.2 \pm 5$  nm, presenting the lowest thickness compared to the rest of the samples, concluding that the thickness plays a crucial role. In the rest of the devices, the thickness of the BFO film increases, causing the efficiencies to decrease considerably, as shown in the previous Figure 4.8b.

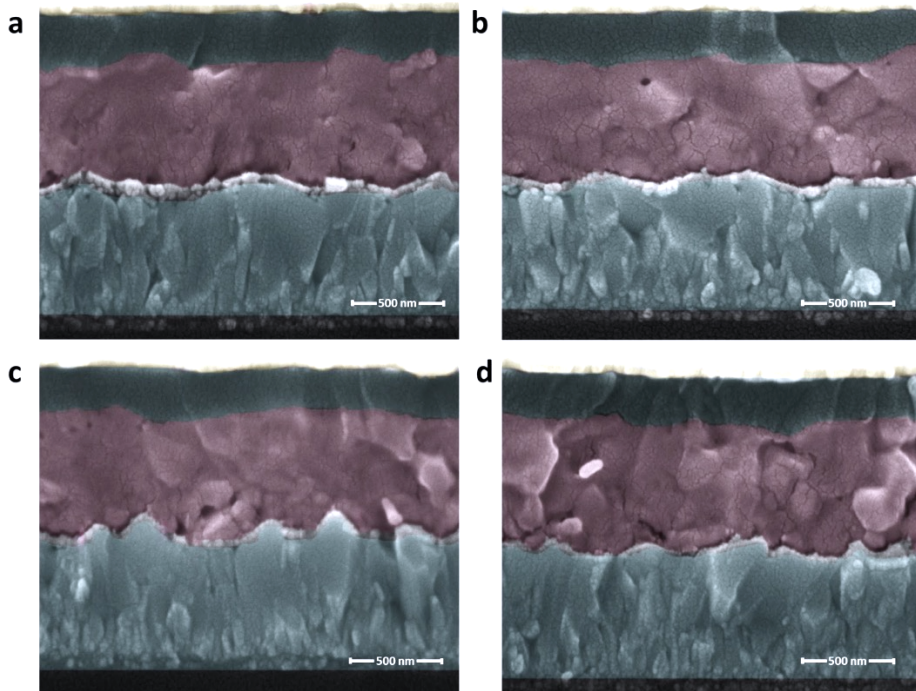


Figure 4.9. Cross Sectional Image of BFO solar cells having various concentration and thickness. a) 0.25 M b) 0.20 M, c) 0.15 M and d) 0.10 M.

BFO being a ferroelectric material, tends to orient its electric dipoles in a direction parallel to that of the applied electric field. The manipulation of orientation of the dipoles enables exploiting to our advantage the property called polarisation assisted charge separation; wherein the polarisation field in addition to the built-in field helps in electron hole separation which is evident from the poling curves depicted in Figure 4.10. As the poling bias is increased gradually in steps of 20 mV, the short circuit current increases accordingly, although the correlation is not exactly linear.



### 4.2.3. Poling Method

The poling of the cells was performed using a 0.158 cm<sup>2</sup> active area mask, using a Keithley 2601 sourcemeter connected to a computer and software. Poling was carried out at 1 sun A.M. 1.5 G in Nitrogen (including UV light) without encapsulation and UV filter through the careful measurement of IV-curves up to 2.5 V maximum, in reverse mode and applying scan rate of 20 mV/s. The reverse IV curves, with a starting voltage 5-10 mV higher than the initial  $V_{OC}$ , were iterated until the photovoltaic parameters stabilized. Then, the reverse IV curves were performed with starting voltages successively increasing by 20 mV until the optimum efficiency (usually around 2 V) was reached. Forward and dark-current curves were taken at various points throughout the poling process, and after maximum efficiency had been achieved.

*Table 4-1. Biasing process used for bias dependent stability test.*

Poling	Scan Rate	Scan Direction	$V_{max}$	$V_{min}$	$V_i$	$\Delta V_i$	$V_f$	$\Delta V_f$
A	20 mV/s	Reverse	+2.5 V	-0.1 V	+1.1 V	0.02 V	-0.1 V	0
B	20 mV/s	Reverse	+2.5 V	-2.5 V	+2.5 V	0	-0.1 V	0.02
C	20 mV/s	Reverse	+2.5 V	-3.2 V	+2.5 V	0	-2.5 V	0.02

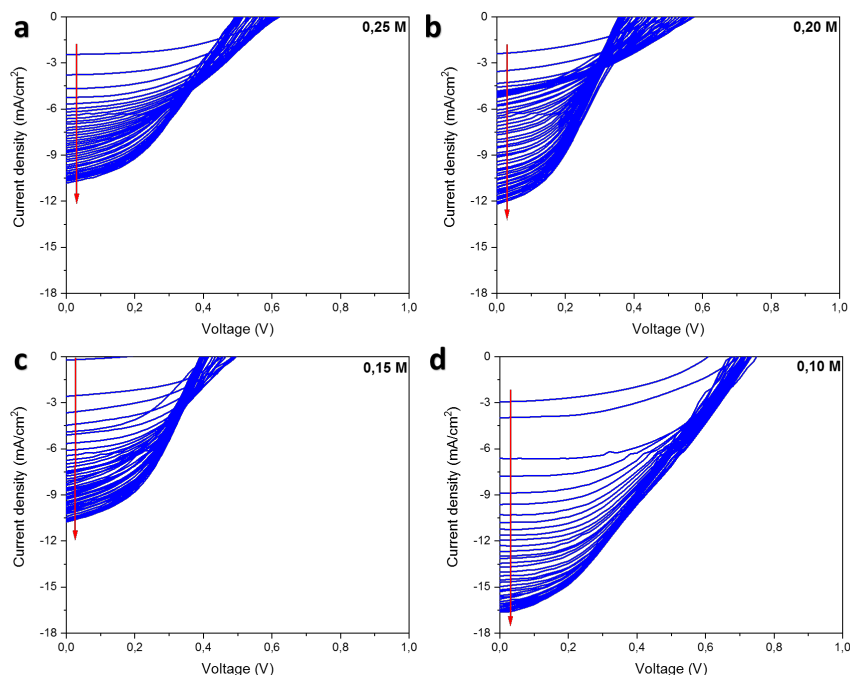


Figure 4.10. I-V poling curves with increasing bias and AM 1.5G irradiation for different concentrations. a) 0.25 M, b) 0.20 M, c) 0.15 M and d) 0.10 M.

However, as stated earlier these devices originally gives very low efficiencies mostly around  $0.6\% \pm 0.2$  owing to the insulating nature and randomly aligned dipoles of the oxide layer. The best performing batch of devices were the ones having 0.1 M BFO precursor concentration as observed in Figure 4.8b. Devices prepared with precursor concentrations other than 0.1 M always fetched lesser efficiency. The best device demonstrated an efficiency of  $\sim 3.9\%$  after poling compared to its  $0.59\%$  efficiency before poling. The reverse I-V curve of the best device is shown in Figure 4.11a while the performance statistics of the optimised BFO concentration batch before and after poling are shown in Figure 4.11b. The poling curves in Figure 4.10d correspond to the best performing device. It is noteworthy, that the devices made from

precursor concentration of 0.05 M failed to form a working device due to numerous pinholes resulting in a short circuit.

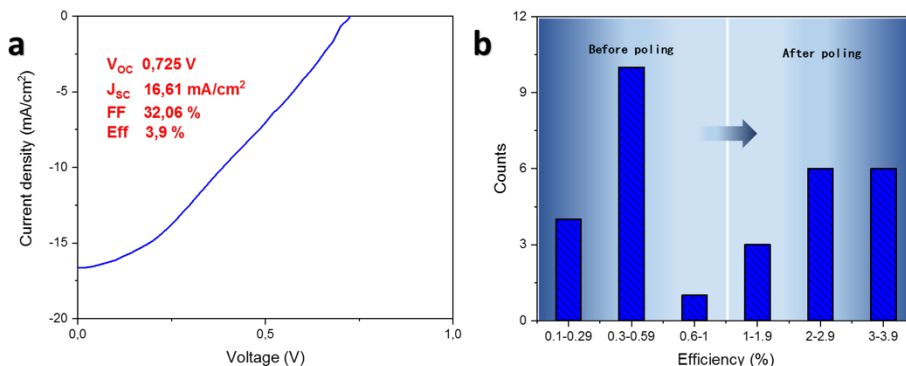


Figure 4.11. a) I-V curve for the champion cell. b) performance statistics of the optimised BFO concentration batch before and after poling.

The EQE in Figure 4.12a, accounts for a photocurrent of only 12.08 mA/cm² while the J-V reads out a value of 16.61 mA/cm². We attribute this difference to a loss of dielectric polarisation in BFO thin film in between the time required to change from the I-V measurement setup to the EQE setup. The differences in the values are demonstrated in Figure 4.12b for the best device.

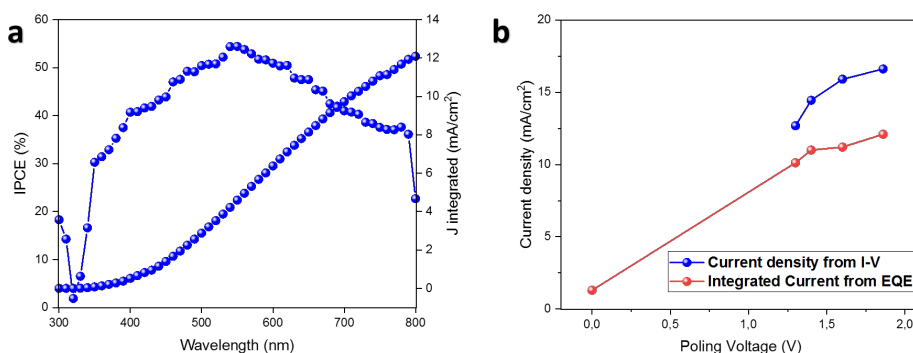


Figure 4.12. a) The EQE and integrated current for the best device. b) A comparison of current density of a device while poling acquired from I-V and IPCE.

This phenomenon is consistent with every solar cell prepared irrespective of its concentration or any other environmental variable. In the literature there are very few examples where these solar cells have EQE > 50%. The first instance of such higher EQE was for an all-oxide solar cell (multi layered BFCO) reported by Nechache et al [33], by application of much higher bias across the cell. It is noteworthy that external quantum efficiencies of our solar cells exceeded 50%. It should also be mentioned that the scanning in the forward direction essentially means reversing the electric field and thus countering the existing dipole moment. Hence, we do not have a forward curve for the J-V plot in Figure 4.11a. The problem of hysteresis which is well-known for classical perovskite solar cells is not of much significance since these cells are always operating in reverse bias condition. Mostly, the hysteresis in PSCs has been attributed to factors like ion migration/undesirable mobile charge as interstitial defects, charge accumulation at interfaces of perovskites and transport layers, very large defect density within or near the surface of the material or specifically generated interface states or the controversial ferroelectric properties leading to slow polarisation of the material [49]. However, apart from these inherent reasons cited in literature, we believe the ferroelectric BFO itself leads to spontaneous polarisation upon applying bias resulting in locked charges/ions in the perovskite bulk (proximal to the BFO layer) a hint which we also note from the impedance curve in Figure 4.13. After poling the capacitance of the device increases which hints more charges/ions locked near the junction compared to a non-polarised cell. This can be visualised as perovskite spin-coated over

a parallel plate capacitor, results in induced charges due to the dielectric and mostly locked ions/charges near the junction.

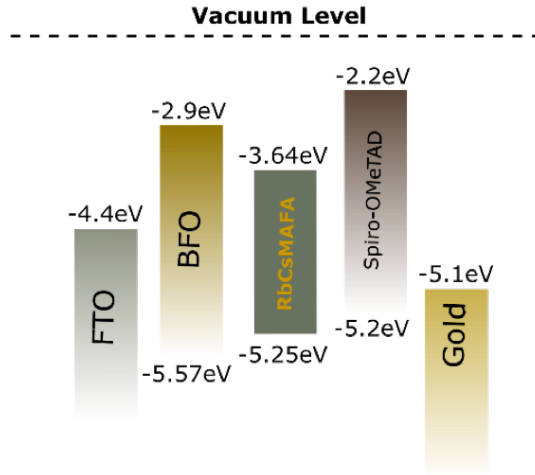


Figure 4.13. Energy levels of the components derived from UPS.

An interesting observation was low fill factor of the solar cells. Fill factor is primarily dependent upon the ratio of charge extraction and charge recombination. As evident from the energy level diagram (obtained from the Ultraviolet Photoelectron Spectroscopy measurements, Figure 4.7), BFO and  $\text{Rb}_{0.05}\text{Cs}_{0.10}\text{MAFAPb}(\text{I},\text{Br})_3$  perovskite forms a straddling type I heterojunction, which is a major barrier for charge transport processes. A schematic energy level diagram is depicted Figure 4.13. By poling the solar cell, we aim to reduce the mismatch between the energy levels by orienting the dipoles in the BFO layer. However, the knowledge of final energy levels after poling could not be determined due to technical limitations. We hypothesise that the band offsets are such that it allows tunnelling to occur which could describe the increase of

current in these solar cells. On the contrary, normal perovskite solar cells behave the opposite with increasing poling voltage. To support this, we perform load extraction and impedance measurement using an all-in-one measurement system on the PAIOS equipment. In charge extraction analysis, the solar cell is illuminated, and an open circuit voltage ( $V_{OC}$ ) is induced, so that no current flows. In this state, the light-generated charge carriers recombine. At  $t = 0$ , the light turns off, and at the same time the voltage goes to zero (or reverse bias). The charge carriers are extracted by the built-in field and give rise to a current. Integration of the extraction current over time yields the extracted charge. The charge carrier density  $n_{CE}$  is then calculated from the equation,

$$n_{CE} = \frac{1}{d \cdot q} \left\{ \int_0^{t_e} j(t) \cdot dt - (V_A - V_E) \cdot C_{geom} \right\}$$

, where  $d$  is the device thickness, then  $q$  is the unit charge,  $t_e$  is the extraction time (usually 1 ms is enough),  $j(t)$  is the transient current density, also  $C_{geom}$  is the geometric capacitance,  $V_A$  the voltage applied prior extraction (in most cases  $V_{OC}$ ), and finally,  $V_E$  is the extraction voltage. The charge on the capacitance is subtracted, because we only care about the density of the charge carrier within the bulk [50][51]. The results as shown in Figure 4.14 depicts the distinct differences in the charge extraction values before and after poling the solar cells at different light intensities. Poling the solar cell results in much superior charge extraction owing to the increase in conductivity of the BFO layer which is one of the logical explanations that can be inferred from the experiments.

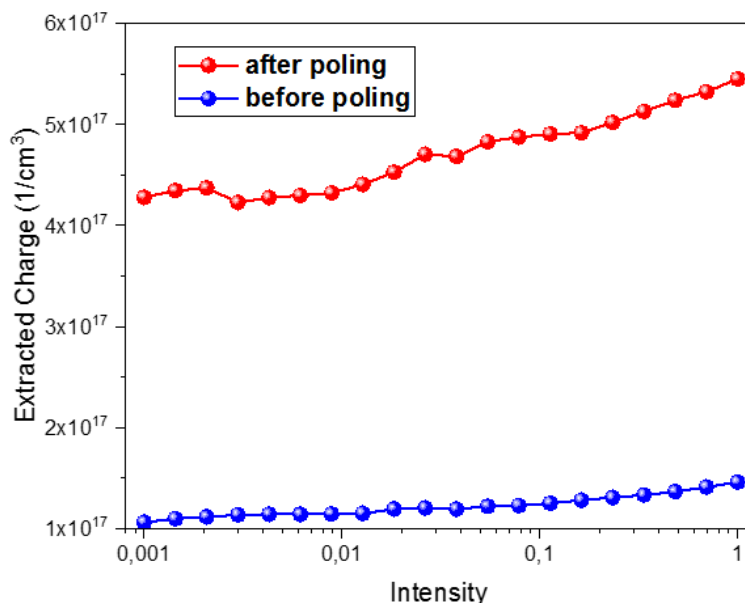


Figure 4.14. A comparison of extracted charge for a solar cell before and after poling.

Impedance spectroscopy data, in Figure 4.15a hints towards higher charge accumulation after poling, not to neglect the low frequency response which points out the slow defects or ion migration processes. We also performed Transient Photocurrent spectroscopy on these solar cells to verify the findings of the charge extraction study. The normalized photocurrent decay curves before and after poling are shown in Figure 4.15b. The overshoots in the graph before poling points to extraction barriers (from poor alignment) as can be seen from the energy level diagram. Before poling, at 1 sun illumination, the carrier transit time is 2.18  $\mu\text{s}$  while after poling under same conditions the transit time reduces to 1.80  $\mu\text{s}$ . Thus, facilitating the extraction of charges after poling which perfectly corroborates with the findings of charge extraction.

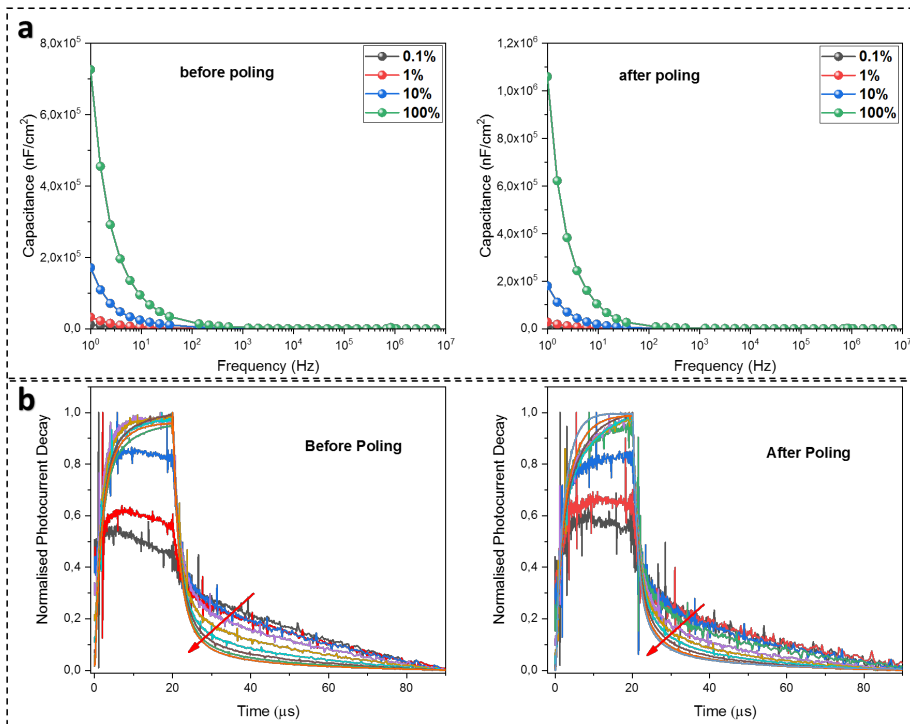


Figure 4.15. a) A comparison of Capacitance vs. Frequency curves under light sweep of a solar cell before and after poling. b) Normalised Transient Photocurrent Decays before and after poling.

#### 4.2.4. Grain Size in BFO/Perovskite heterojunctions, charge transport and efficiency

In this section, we analysed the effect of halide perovskite grain size on the poling and final device efficiency. To modify the grain size of the halide perovskite, a series of experiments were planned where the time and temperature were modified. In summary, grain size modulation was performed by varying the annealing time of the perovskite used in BFO, where it was observed that temperature plays an important role in grain size, which is closely related to the behaviour of the device efficiency. In Figure 4.16a it can be seen that



the smaller the grain size, the current density increases, in the same way the voltage increases, on the other hand, the larger the grain size, the inverse effect occurs, the current density and voltage decrease (See Figure 4.16b), it can also be seen that the perovskite film begins to present holes due to degradation, which could be a factor affecting its efficiency.

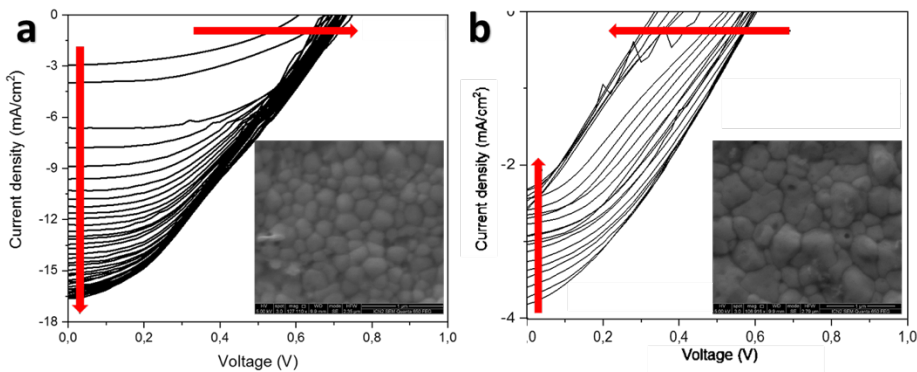


Figure 4.16. BFO-based PSC. Evolution of IV curves during poling depending on the halide perovskite grain size (a) small grain and (b) big grain.

In Figure 4.17a and 4.17b we can observe the SEM images of the same behaviour with a different ferroelectric, in this case PZT. A statistic of the effect of the grain size and its relationship with the efficiency of the devices is presented. In the graph of Figure 4.17c we observe that the initial efficiency of the devices is higher in large grains, but this changes after the devices were subjected to polarization, that is, the final efficiency for small grains is much better compared to the of big grains. In Figure 4.17d we appreciate the difference between the initial and final efficiency, where we verify that the smaller the grain size, the better the efficiency and as the grain size increases, the efficiency decreases.

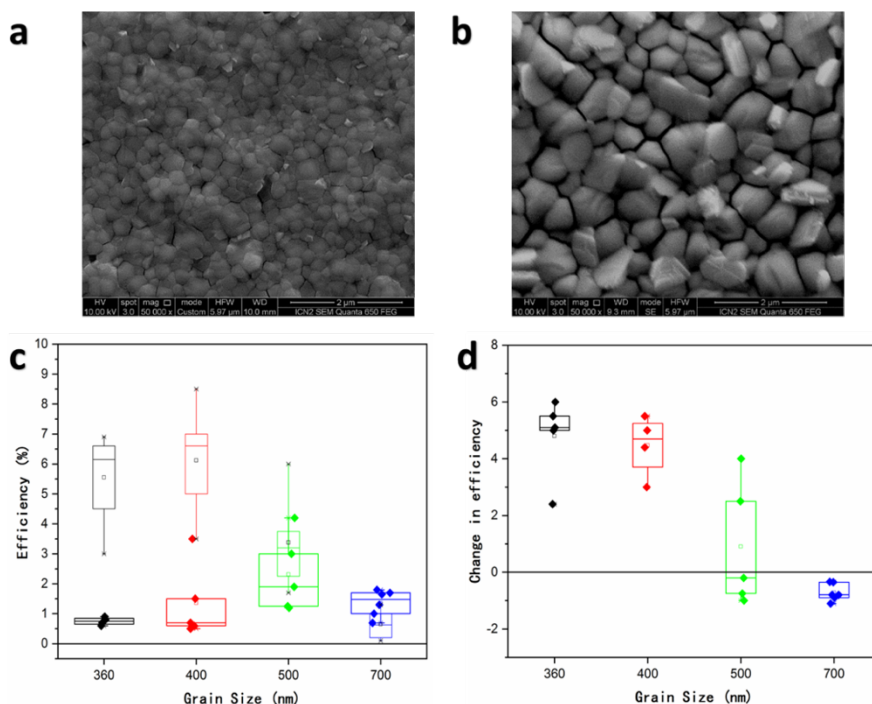


Figure 4.17. SEM image of PZT film with small (a) and big (b) grain size, (c) Statistics of initial efficiency and after poling depending on grain size of perovskite in PSCs, (d) Difference of initial efficiency and end of PSCs with different grain size.

Reason for this behaviour is due to horizontal charge transport in large halide perovskite grains Vs vertical charge transport in small grains (See Figure 4.18). Probably due to transport through grain boundaries. The (110) oriented grains show an in-plane ferroelectric polarization that, according to earlier simulations of the Alessandro Pecchia i.e. group, facilitates the charge carrier separation in solar cells [52][53].

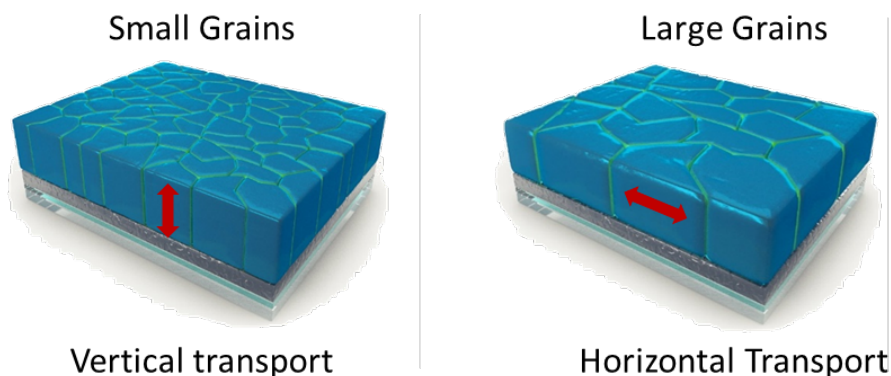


Figure 4.18. Horizontal charge transport in large perovskite grains and vertical charge transport in small perovskite grains.

To determine the ferroelectric polarization of the perovskite material, positive and negative poling processes were sequentially applied and measured. In Figure 4.19, the topography observed in the light and with polarization, revealed a higher current for the samples with the smallest grain size 360, 400, 500 and 700 nm, respectively, decreasing the current of the sample as the grain was larger, where the sample that had the largest grain size shows conductivity only near the limits of grain, also presented a crystalline structure that protrudes from the surface. Therefore, grain size is a critical factor for effective ferroelectric polarization manipulation rather than crystal morphology. In short, the small grain perovskites probably have out of plane polarization while large grain perovskites have in-plane polarization, therefore it presents a better current and could be an important factor in the operation of the device. However, careful interpretation is still needed because the perovskite crystals with different grain size simultaneously generate different thickness.

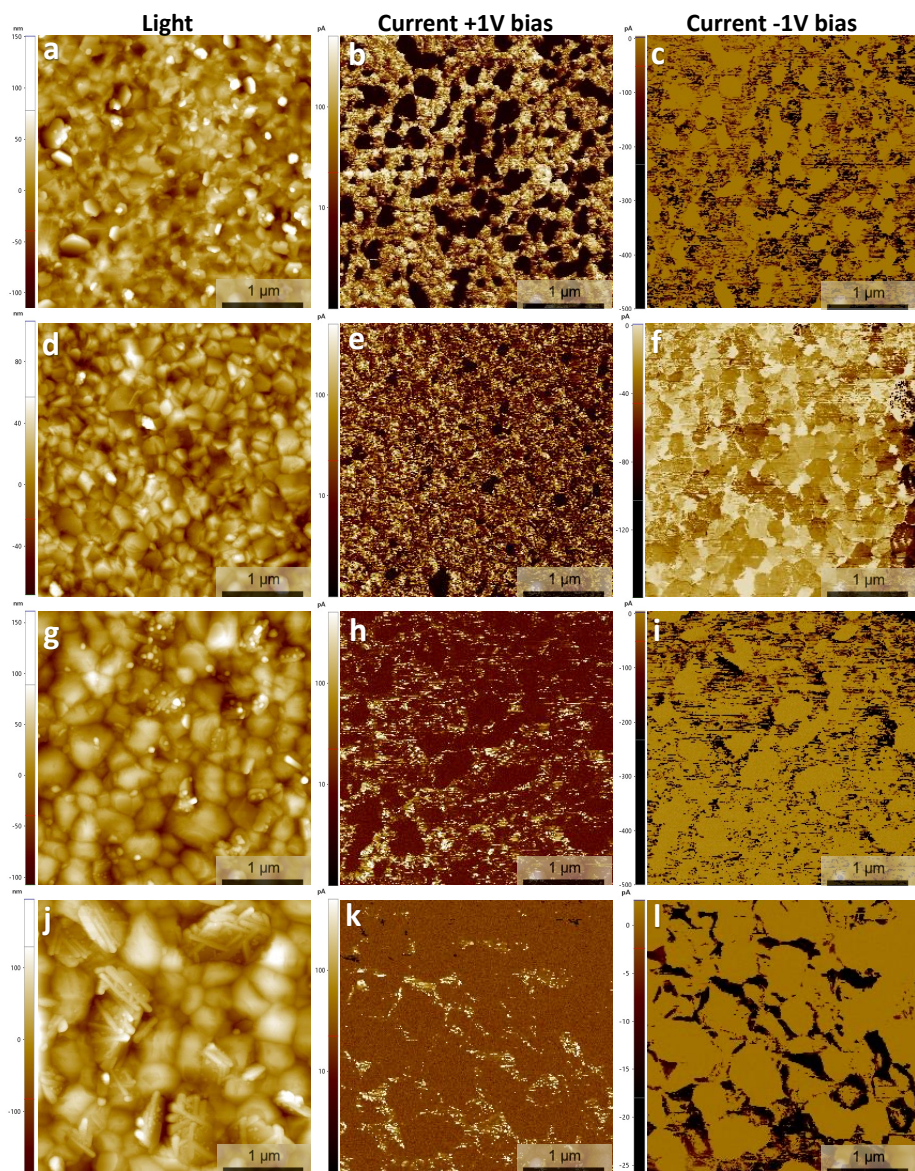


Figure 4.19. AFM topographic images and conductivity maps images measured in the light for the with size of (a-d) 360 nm, (f-h) 400 nm, (i-k) 500 nm and (l-n) 700 nm. Measured areas were  $5\ \mu\text{m} \times 5\ \mu\text{m}$ .

#### 4.2.5. Switching properties

Stability of a device is of immense significance standing at this stage of development of the technology. Two different kinds of tests were performed to investigate the effects of bias and illumination conditions. The data of both the experiments are compiled in Figure 4.20a and 20b. For the test under various biasing conditions the cell was kept under continuous solar irradiation while the three different phases of bias were applied. The section A represents the main positive poling section (resultant positive), the section B represents the neutralising bias section while section C represents the resultant negative biasing condition.

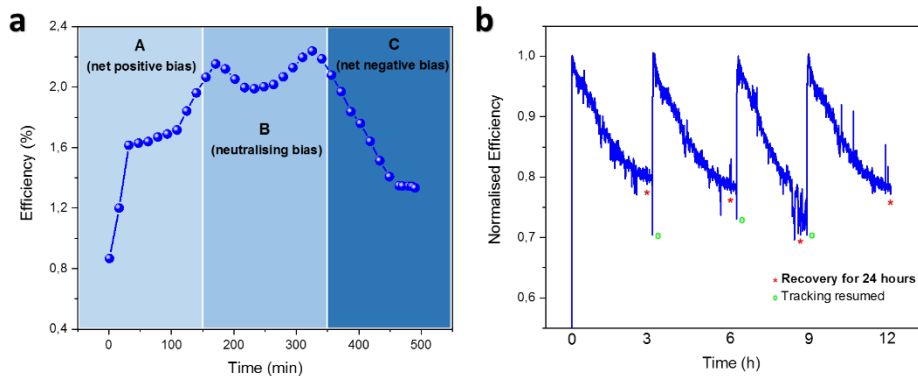


Figure 4.20. a) Bias dependent operation characteristics of the BFO solar cells. b) Standard stability test in Nitrogen atmosphere under AM 1.5 G irradiation at 45 °C without UV filter.

This experiment proves the role of reverse scans and net positive poling for the functioning of the solar cell. As the poling increased in the phase A, randomly ordered domains in the BFO layers started orienting themselves in the direction of the field, facilitating vertical charge transport (the physics being the favourable band bending).

Thereafter, as the effect of positive poling was started to neutralise the solar cell resisted the change owing to the remnant polarisation of the BFO layer. As we further increased the negative poling, the domains started reordering in the direction of the field, which was now reversed, thus leading to a trend in decreasing efficiency. Importantly, the cells recovered after sufficient time to reverse the molecular changes taken place during the experiments. This points out to another venue of application of these solar cells as “solaristors” or other multifunctional areas of Internet of Things (IoT), which will be investigated in future experiments. Extending the stability tests, we continuously tracked I-V curves every minute in order to maintain the poling effect and study the stability. As we see from Figure 4.20b, the  $T_{80}$  for one cycle of continuous I-V tracking was around 3 hours on an average. Interestingly the cells recovered after sufficient rest in the dark (preferably 24 hours or more). This certainly hints to some reversible degradation from bias and light which may indicate ion migration in perovskite or defect dipole formation/annihilation in BFO [54]. Moreover, which process plays a more dominant role, or the exact functioning of these reversible processes still needs to be studied in greater detail. Additionally, we believe that a part of this response could also be rooted to fatigued perovskite thin films [55]. When compared to the behaviour of solar cells that use PZT, we see that the oxides BFO and PZT do not function similarly. For example, PZT solar cells works well under ambient atmosphere while BFO solar cells work best in inert atmosphere. This open a new question to study what is fundamentally different in these oxides which impacts their role in solar cell so differently.



#### 4.2.6. Stability

The graph in Figure 4.21 represents the evolution of the photovoltaic parameters of a cell with poling and constant AM 1.5G irradiation. A trend to be noted, that the efficiency primarily follows the current density curve, which is also the primary factor we are trying to manipulate.

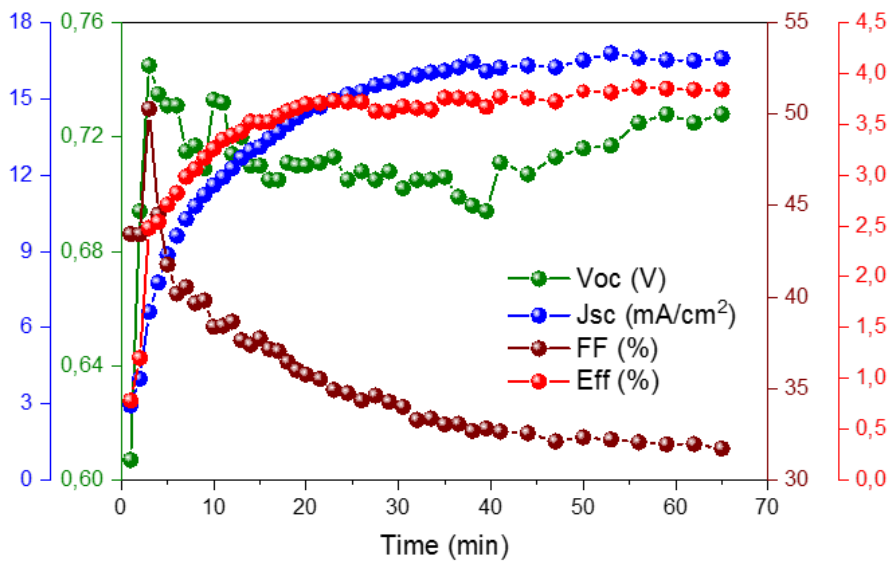


Figure 4.21. The photovoltaic parameter evolution with increasing poling bias and increasing time, depicting the dependency of efficiency on other parameters.  $J_{sc}$  (blue),  $V_{oc}$  (green), FF (brown), Efficiency (red).

The solar cells were subjected a series of operational conditions: in air with UV filter, in air without UV filter, in Nitrogen with UV filter, in Nitrogen without UV filter. The graph in Figure 4.22 proves that the cells performed the best when operated in nitrogen without UV filter. These tests were performed after a full course of poling the samples till their maximum efficiency point and then applying the

optimum bias every time a measurement was taken in intervals of 1 min for the first 5 readings, 2 minutes for the next 5 measurements, 5 minutes for the next 5 measurements, 10 minutes for the next 5 measurements until 90 minutes. The cell was kept under continuous solar irradiation during the process.

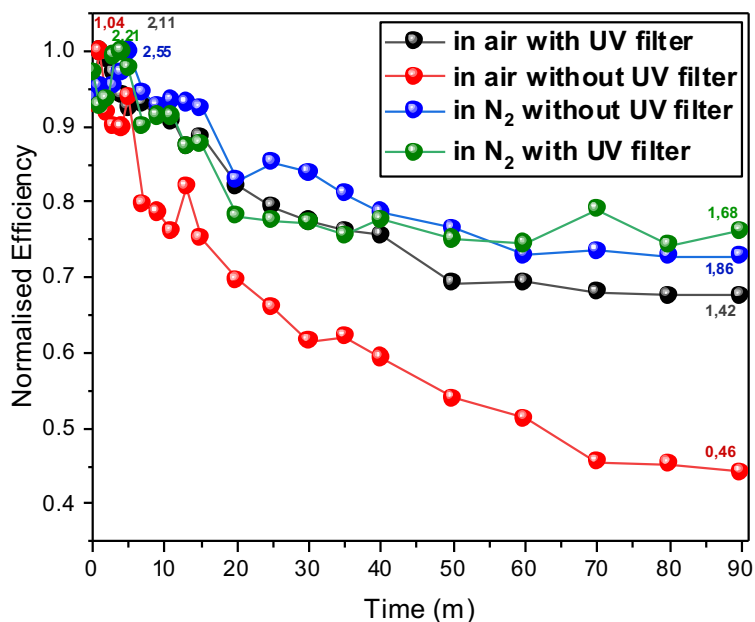


Figure 4.22. Dependency of efficiency with respect to the conditions exposed under air/N<sub>2</sub> or with or without UV filter.

On poling, the phenomenon of increasing photocurrent has been previously reported by Perez-Tomas et. al where they found a direct dependence on conductivity of Lead Zirconate Titanate (PZT) thin films and UV irradiation and bias [5]. We report a similar behaviour, although the role and functioning of oxygen vacancies are not very clear for BFO. As mentioned before, we observe almost three-fold increase in conductivity when compared to BFO conductivity in dark, which we also propose as the cause of increasing photocurrent



with poling. The values of the photocurrent and open photovoltage reported here for solar cells using BFO with halide perovskites exceeds any of the existing reports [38][36] except for the report of Zhao et al [37], where they reported an open circuit voltage of 1.62 V, however the photocurrent and efficiency were much lower than ones reported here. We demonstrate a  $V_{OC}$  of 0.725 V and a  $J_{SC}$  of 16.61 mA/cm<sup>2</sup> for the best device.

### 4.3. Discussions

We have prepared PSCs applying ferroelectric oxides as ETL. The oxide BFO was synthesized by sol gel solution and applied by spin coating on top of the FTO electrode. The FBO thin film was applied as a dense thin layer and a coating of the halide perovskite was deposited on top in a perovskite oxide/halide perovskite heterojunction. The as-prepared PSC observed almost null photovoltaic response with  $V_{OC}$  in the range of 0.6 V and  $J_{SC}$  in the range of 3 mA/cm<sup>2</sup>. The application of poling (bias voltage) to the PSC allowed the slow but constant enhancement of the photovoltaic properties with time reaching values of 0.9 V for  $V_{OC}$  and 16.61 mA/cm<sup>2</sup> for  $J_{SC}$ . The poling was carried out under light irradiation at room temperature. Conductivity measurements performed to the BFO thin film confirmed the change in conductivity of the BFO in agreement with the improvement of PCE of the solar cell. This indicates that the initial ferroelectric oxide modifies its transport properties from insulator to conductor in detrimental to its ferroelectric properties. The latter was already observed in other ferroelectric oxides like the PZT.

We have also observed a dependency of the halide perovskite grain size on the final photovoltaic properties of the devices. In general, for halide perovskites with small grain sizes (below xxx nm), the photovoltaic properties of the PSC improve with poling under light irradiation. On the contrary, large grain sizes results in detrimental effect of the photovoltaic properties of the solar cells with time. We initially attributed this effect to a difference in transport properties of the halide perovskite. Published reports indicate a possible horizontal and vertical transport of electrons observed for large and small grain sizes, respectively. However, although our PFM studies confirm higher conductivity and transport properties for the sample with small grains, we believe the grain boundaries play an important role. The smaller grain sizes allow for large amount of grain boundaries which are better electron paths for conductivity. The later is still under evaluation in our group.

Finally, we carried out stability analysis of the solar cells under different testing conditions with variation of atmosphere and UV light irradiation. The devices were analysed under constant irradiation for different periods of time. Our results demonstrate that the devices show good photovoltaic properties even under conditions of UV light irradiation which confirms that the BFO provides enhanced stability to the solar cells.

#### 4.4. References

- [1] I. Grinberg *et al.*, “Perovskite oxides for visible-light-absorbing ferroelectric and photovoltaic materials,” *Nature*, vol. 503, no. 7477, pp. 509–512, 2013.
- [2] H. Matsuo, Y. Noguchi, and M. Miyayama, “Gap-state engineering of visible-light-active ferroelectrics for photovoltaic applications,” *Nat. Commun.* 2017 81, vol. 8, no. 1, pp. 1–8, Aug. 2017.
- [3] H. S. Kim *et al.*, “Effect of cs-incorporated NiOx on the performance of perovskite solar cells,” *ACS Omega*, vol. 2, no. 12, pp. 9074–9079, Dec. 2017.
- [4] G. Zhang *et al.*, “New high Tc multiferroics KBiFe2O5 with narrow band gap and promising photovoltaic effect,” *Sci. Reports* 2013 31, vol. 3, no. 1, pp. 1–9, Feb. 2013.
- [5] A. Pérez-Tomas *et al.*, “PbZrTiO3 ferroelectric oxide as an electron extraction material for stable halide perovskite solar cells,” *Sustain. Energy Fuels*, vol. 3, no. 2, pp. 382–389, Jan. 2019.
- [6] A. Perez, “Solution processable semiconductor oxides in Organic and perovskite solar cells: from binary to complex oxide materials,” *Futur. Semicond. Oxides Next-Generation Sol. Cells*, pp. 282–283, 2017.
- [7] H. Li *et al.*, “Photoferroelectric perovskite solar cells: Principles, advances and insights,” *Nano Today*, vol. 37, p. 101062, Apr. 2021.
- [8] S. Sidhik, C. Rosiles Pérez, M. A. Serrano Estrada, T. López-Luke, A. Torres, and E. De la Rosa, “Improving the stability of perovskite solar cells under harsh environmental conditions,” *Sol. Energy*, vol. 202, pp. 438–445, May 2020.
- [9] H.-Y. Ye, Y. Zhang, D.-W. Fu, and R.-G. Xiong, “An Above-Room-Temperature Ferroelectric Organo-Metal Halide Perovskite: (3-Pyrrolinium)(CdCl<sub>3</sub>),” *Angew. Chemie*, vol. 126, no. 42, pp. 11424–11429, Oct. 2014.
- [10] G. Chen *et al.*, “Bismuth ferrite materials for solar cells: Current status and prospects,” *Mater. Res. Bull.*, vol. 110, pp. 39–49, Feb. 2019.
- [11] T. Kumari *et al.*, “A built-in electric field induced by ferroelectrics increases halogen-free organic solar cell efficiency in various device types,” *Nano Energy*, vol. 68, p.

- 104327, Feb. 2020.
- [12] M. R. Morris, S. R. Pendlebury, J. Hong, S. Dunn, and J. R. Durrant, "Effect of Internal Electric Fields on Charge Carrier Dynamics in a Ferroelectric Material for Solar Energy Conversion," *Adv. Mater.*, vol. 28, no. 33, pp. 7123–7128, Sep. 2016.
  - [13] L. You *et al.*, "Enhancing ferroelectric photovoltaic effect by polar order engineering," *Sci. Adv.*, vol. 4, no. 7, Jul. 2018.
  - [14] H. Röhm, T. Leonhard, M. J. Hoffmann, and A. Colsmann, "Ferroelectric domains in methylammonium lead iodide perovskite thin-films," *Energy Environ. Sci.*, vol. 10, no. 4, pp. 950–955, Apr. 2017.
  - [15] A. Lipatov, A. Fursina, T. H. Vo, P. Sharma, A. Gruverman, and A. Sinitskii, "Polarization-Dependent Electronic Transport in Graphene/Pb(Zr,Ti)O<sub>3</sub> Ferroelectric Field-Effect Transistors," *Adv. Electron. Mater.*, vol. 3, no. 7, p. 1700020, Jul. 2017.
  - [16] Y. Liu *et al.*, "Magnetic-Induced-Piezopotential Gated MoS<sub>2</sub> Field-Effect Transistor at Room Temperature," *Adv. Mater.*, vol. 30, no. 8, p. 1704524, Feb. 2018.
  - [17] J. Jiang *et al.*, "Temporary formation of highly conducting domain walls for non-destructive read-out of ferroelectric domain-wall resistance switching memories," *Nat. Mater.* 2017 171, vol. 17, no. 1, pp. 49–56, Nov. 2017.
  - [18] R. Xu *et al.*, "Kinetic control of tunable multi-state switching in ferroelectric thin films," *Nat. Commun.* 2019 101, vol. 10, no. 1, pp. 1–10, Mar. 2019.
  - [19] W. J. Hu, Z. Wang, W. Yu, and T. Wu, "Optically controlled electroresistance and electrically controlled photovoltage in ferroelectric tunnel junctions," *Nat. Commun.* 2016 71, vol. 7, no. 1, pp. 1–9, Feb. 2016.
  - [20] Z. Wen, C. Li, D. Wu, A. Li, and N. Ming, "Ferroelectric-field-effect-enhanced electroresistance in metal/ferroelectric/semiconductor tunnel junctions," *Nat. Mater.* 2013 127, vol. 12, no. 7, pp. 617–621, May 2013.
  - [21] A. Chanthbouala *et al.*, "A ferroelectric memristor," *Nat. Mater.*, vol. 11, no. 10, pp. 860–864, 2012.
  - [22] R. Guo *et al.*, "Interface-engineered electron and hole tunneling," *Sci. Adv.*, vol. 7, no. 13, Mar. 2021.
  - [23] "Photoferroelectrics - Vladimir M. Fridkin - Google Libros." [Online]. Available:

[https://books.google.es/books?hl=es&lr=&id=MIP0CAAAQB  
AJ&oi=fnd&pg=PA3&ots=8FWYvfDkr0&sig=6OmQDRbIWKj  
WghxwLyrsCLiNZbk&redir\\_esc=y#v=onepage&q&f=false](https://books.google.es/books?hl=es&lr=&id=MIP0CAAAQB<br/>AJ&oi=fnd&pg=PA3&ots=8FWYvfDkr0&sig=6OmQDRbIWKj<br/>WghxwLyrsCLiNZbk&redir_esc=y#v=onepage&q&f=false).  
[Accessed: 15-Dec-2021].

- [24] S. R. Basu *et al.*, "Photoconductivity in BiFeO<sub>3</sub> thin films," *Appl. Phys. Lett.*, vol. 92, no. 9, p. 091905, Mar. 2008.
- [25] R. Nechache *et al.*, "Bandgap tuning of multiferroic oxide solar cells," *Nat. Photonics* 2014 91, vol. 9, no. 1, pp. 61–67, Nov. 2014.
- [26] T. Choi, S. Lee, Y. J. Choi, V. Kiryukhin, and S. W. Cheong, "Switchable ferroelectric diode and photovoltaic effect in BiFeO<sub>3</sub>," *Science*, vol. 324, no. 5923, pp. 63–66, Apr. 2009.
- [27] M. Alexe and D. Hesse, "Tip-enhanced photovoltaic effects in bismuth ferrite," *Nat. Commun.* 2011 21, vol. 2, no. 1, pp. 1–5, Mar. 2011.
- [28] S. Y. Yang *et al.*, "Above-bandgap voltages from ferroelectric photovoltaic devices," *Nat. Nanotechnol.*, vol. 5, no. 2, pp. 143–147, 2010.
- [29] R. Guo *et al.*, "Non-volatile memory based on the ferroelectric photovoltaic effect," *Nat. Commun.* 2013 41, vol. 4, no. 1, pp. 1–5, Jun. 2013.
- [30] J. Qi, N. Ma, Y. Yang, J. Qi, N. Ma, and Y. Yang, "Photovoltaic–Pyroelectric Coupled Effect Based Nanogenerators for Self-Powered Photodetector System," *Adv. Mater. Interfaces*, vol. 5, no. 3, p. 1701189, Feb. 2018.
- [31] J. Qi, N. Ma, X. Ma, R. Adelung, and Y. Yang, "Enhanced Photocurrent in BiFeO<sub>3</sub> Materials by Coupling Temperature and Thermo-Phototronic Effects for Self-Powered Ultraviolet Photodetector System," *ACS Appl. Mater. Interfaces*, vol. 10, no. 16, pp. 13712–13719, Apr. 2018.
- [32] H. Mai *et al.*, "Photovoltaic Effect of a Ferroelectric-Luminescent Heterostructure under Infrared Light Illumination," *ACS Appl. Mater. Interfaces*, vol. 10, no. 35, pp. 29786–29794, Sep. 2018.
- [33] R. Nechache *et al.*, "Bandgap tuning of multiferroic oxide solar cells," *Nat. Photonics* 2014 91, vol. 9, no. 1, pp. 61–67, Nov. 2014.
- [34] V. Keskin, A. Gupta, and G. Szulczewski, "Solution processed TiO<sub>2</sub>/BiFeO<sub>3</sub>/poly(3-hexylthiophene) solar cells," *Mater. Lett.*, vol. 159, pp. 305–308, Nov. 2015.
- [35] Nrel, "National Renewable Energy Laboratory (NREL) Home

- Page,” 2006. [Online]. Available: <https://www.nrel.gov/>. [Accessed: 28-Aug-2018].
- [36] Y. Shirahata, A. Suzuki, and T. Oku, “Fabrication and characterization of bismuth ferrite as an electron transport layer in perovskite photovoltaic devices,” *J. Ceram. Soc. Japan*, vol. 124, no. 5, pp. 602–605, May 2016.
  - [37] P. Zhao, L. Bian, L. Wang, J. Xu, and A. Chang, “Enhanced open voltage of BiFeO<sub>3</sub> polycrystalline film by surface modification of organolead halide perovskite,” *Appl. Phys. Lett.*, vol. 105, no. 1, p. 013901, Jul. 2014.
  - [38] Y. Shirahata and T. Oku, “Characterization and Photovoltaic Properties of BiFeO<sub>3</sub> Thin Films,” *Coatings 2016, Vol. 6, Page 68*, vol. 6, no. 4, p. 68, Dec. 2016.
  - [39] G. Catalan and J. F. Scott, “Physics and Applications of Bismuth Ferrite,” *Adv. Mater.*, vol. 21, no. 24, pp. 2463–2485, Jun. 2009.
  - [40] Y. H. Chu, L. W. Martin, M. B. Holcomb, and R. Ramesh, “Controlling magnetism with multiferroics,” *Mater. Today*, vol. 10, no. 10, pp. 16–23, Oct. 2007.
  - [41] J. Seidel *et al.*, “Conduction at domain walls in oxide multiferroics,” *Nat. Mater.*, vol. 8, no. 3, pp. 229–234, 2009.
  - [42] C. Gutiérrez-Lázaro *et al.*, “Solution Synthesis of BiFeO<sub>3</sub> Thin Films onto Silicon Substrates with Ferroelectric, Magnetic, and Optical Functionalities,” *J. Am. Ceram. Soc.*, vol. 96, no. 10, pp. 3061–3069, Oct. 2013.
  - [43] D. Huang, H. Deng, P. Yang, and J. Chu, “Optical and electrical properties of multiferroic bismuth ferrite thin films fabricated by sol-gel technique,” *Mater. Lett.*, vol. 64, no. 20, pp. 2233–2235, Oct. 2010.
  - [44] S. Y. Yang *et al.*, “Photovoltaic effects in BiFeO<sub>3</sub>,” *Appl. Phys. Lett.*, vol. 95, no. 6, p. 062909, Aug. 2009.
  - [45] D. Cao, C. Wang, F. Zheng, L. Fang, W. Dong, and M. Shen, “Understanding the nature of remnant polarization enhancement, coercive voltage offset and time-dependent photocurrent in ferroelectric films irradiated by ultraviolet light,” *J. Mater. Chem.*, vol. 22, no. 25, pp. 12592–12598, Jun. 2012.
  - [46] J. Wang *et al.*, “Epitaxial BiFeO<sub>3</sub> multiferroic thin film heterostructures,” *Science*, vol. 299, no. 5613, pp. 1719–1722, Mar. 2003.
  - [47] “Strain Mechanisms in Lead-Free Ferroelectrics for Actuators - Matias Acosta - Google Libros.” [Online]. Available:

- <https://books.google.es/books?id=cJx6CwAAQBAJ&pg=PA37&lpg=PA37&dq=L.+Jin,+F.+Li,+S.+Zhang,+J.+Am.+Ceram.+Soc.+2014,+97,+1.&source=bl&ots=feapOpSHuq&sig=ACfU3U11hGBxSXYWJJRoEHNdYgSax6SA&hl=es&sa=X&ved=2ahUKEwjH3d2rmKf1AhUtC2MBHei5CL8Q6AF6BAGKEAM#v=onepage&q=L. Jin%2C F. Li%2C S. Zhang%2C J. Am. Ceram. Soc. 2014%2C 97%2C 1.&f=false>. [Accessed: 10-Jan-2022].
- [48] M. C. Biesinger, B. P. Payne, A. P. Grosvenor, L. W. M. Lau, A. R. Gerson, and R. S. C. Smart, "Resolving surface chemical states in XPS analysis of first row transition metals, oxides and hydroxides: Cr, Mn, Fe, Co and Ni," *Appl. Surf. Sci.*, vol. 257, no. 7, pp. 2717–2730, Jan. 2011.
  - [49] H. J. Snaith *et al.*, "Anomalous hysteresis in perovskite solar cells," *J. Phys. Chem. Lett.*, vol. 5, no. 9, pp. 1511–1515, May 2014.
  - [50] B. Wright *et al.*, "Quantifying Recombination Losses during Charge Extraction in Bulk Heterojunction Solar Cells Using a Modified Charge Extraction Technique," *Adv. Energy Mater.*, vol. 7, no. 11, p. 1602026, Jun. 2017.
  - [51] I. Lange *et al.*, "Correlation between the open circuit voltage and the energetics of organic bulk heterojunction solar cells," *J. Phys. Chem. Lett.*, vol. 4, no. 22, pp. 3865–3871, Nov. 2013.
  - [52] T. Leonhard *et al.*, "Probing the Microstructure of Methylammonium Lead Iodide Perovskite Solar Cells," *Energy Technol.*, vol. 7, no. 3, Mar. 2019.
  - [53] A. Pecchia, D. Gentilini, D. Rossi, M. Auf Der Maur, and A. Di Carlo, "Role of Ferroelectric Nanodomains in the Transport Properties of Perovskite Solar Cells," *Nano Lett.*, vol. 16, no. 2, pp. 988–992, Feb. 2016.
  - [54] K. Domanski *et al.*, "Migration of cations induces reversible performance losses over day/night cycling in perovskite solar cells," *Energy Environ. Sci.*, vol. 10, no. 2, pp. 604–613, Feb. 2017.
  - [55] F. Huang *et al.*, "Fatigue behavior of planar CH<sub>3</sub>NH<sub>3</sub>PbI<sub>3</sub> perovskite solar cells revealed by light on/off diurnal cycling," *Nano Energy*, vol. 27, pp. 509–514, Sep. 2016.

# Chapter 5: Material and Methodology

---

This chapter detailed the materials and the fabrication process of the devices, followed by the characterization, including a brief description of the equipment used for the characterization.

## 5.1. Materials

### 5.1.1. Chemical and solvents

All chemical reagents and solvents were commercially available and were used without further modification.

Ethanol (99.5% Panreac), isopropanol (99.5% Sigma-Aldrich), acetone (99.5% Panreac), Hellmanex III (Hellma™), Zn powder (Fluka Analytical); hydrochloric acid HCl (37%, Panreac), gamma-butyrolactone (GBL) (99% Sigma Aldrich), PbI<sub>2</sub> (TCI, >98%), PbBr<sub>2</sub> (TCI, >98%), FAI (Greatcell), MAI (Greatcell), MABr (Greatcell), CsI (ABCR, 99.998%), RbI (ABCR, 99.998%), dimethylformamide (DMF) (Acros Organics, 99.8%, extra dry), dimethyl sulfoxide (DMSO) (Acros Organics, 99.8%, extra dry), 2,20,7,70-tetrakis(N,N-di-p-methoxyphenyl-amine)9,90-spirobifluorene (spiro-OMeTAD) (Merck), 4-tert-butylpyridine (TBP) (Sigma Aldrich), lithium bis(trifluoromethanesulfonyl) imide (Li-TFSI) (Sigma Aldrich), titanium diisopropoxide bis (acetylacetonate) (Sigma Aldrich), acetylacetone (Sigma Aldrich), titania paste (Greatcell), chlorobenzene (Sigma Aldrich), 3-phosphonopropionic acid (Sigma



Aldrich), and acetonitrile (Sigma Aldrich), Bismuth Nitrate Pentahydrate (99.99+%, Sigma Aldrich), Iron Acetylacetonate (99.9%, Sigma Aldrich), 1,3-Propanediol (98%, Sigma Aldrich) and Glacial Acetic Acid (100%, Merck).

## 5.2. Methodology

### 5.2.1. Device fabrication

#### **Transparent conductive oxide (TCO) substrates:**

FTO substrates (Nippon Sheet Glass 10  $\Omega$ /sq) were etched with Zn powder and 4 M HCl, and then subjected to a four-stage cleaning protocol. First, they are washed using a Hellmanex® solution, deionized water, ethanol, and 2-propanol for 15 minutes with each one in the ultrasound to later be dried with compressed air.

#### **Electron Transport Layer (ETL)**

A compact solution of TiO<sub>2</sub> (c-TiO<sub>2</sub>) was prepared with titanium diisopropoxide bis(acetylacetonate):acetylacetonone:ethanol = 0.6:0.4:9 (v:v) and deposited on the conductive side of the substrates by the spray pyrolysis method. To do this, the substrates are placed on a heating plate at 450 °C and sprayed with the solution and kept for 30 minutes at 450 °C, then allowed to cool to room temperature. This technique allows the mixture to be deposited in a thin film in a homogeneous manner. The mesoporous TiO<sub>2</sub> layers were deposited using the spin-coating technique at 5,000 rpm for 20 seconds using a TiO<sub>2</sub> paste diluted in ethanol (1:6 w:w). After maintaining the substrates at 80 °C for 10 min, they are heated at 450 °C for 30 min

and allowed to cool to room temperature. (no post-treatments were conducted for the substrates before deposition).

### **BFO Synthesis**

The synthesis of BFO was done by a simple sol-gel process. 0.25 M Bismuth Nitrate Pentahydrate and Iron Acetylacetonate were dissolved separately in glass vials by stirring for 45 min. The solvent was a 1:4 mixtures of 1,3-Propanediol and Glacial Acetic Acid. After dissolution, the Bismuth precursor was mixed into the Iron precursor and was let to stir for 30 min. Finally, the solution was filtered and diluted as per requirement for spin coating.

### **Electron Transport Layer (ETL)**

**BFO Thin Film:** The resultant 0.25 M solution was filtered using a 0.2  $\mu$ . The resultant 0.25 M solution was filtered using a 0.2 ccess. 0.25 M Bismuth amount of solvent. 50  $\mu$ L of the solution was spin coated on top of cleaned and etched FTO substrate in static condition for 40 seconds, with 3000 rpm and acceleration of 1000 rpm/s. Before spin coating a part of the FTO was covered with tape to avoid deposition of BFO. After spin coating, the film was first dried in a hot plate at 150 °C and later transferred to another hotplate at preheated to 250 °C. After 5 min, the film was put in a furnace preheated to 500 °C for 10 min and then allowed to cool down rapidly in ambient atmosphere.

### **Halide Perovskite solutions (quadruple cation)**

The quadruple cation halide perovskite  $\text{Rb}_{0.05}\text{Cs}_{0.05}\text{MA}_{0.15}\text{FA}_{0.75}\text{Pb}_{1.05}(\text{I}_{0.95}\text{Br}_{0.05})_3$  was prepared as follows.

Briefly, first 1.5 M stock solution of (1) CsI (DMSO), (2) RbI (DMSO), and (3)  $\text{PbI}_2$  (DMSO:DMF = 1:4) were prepared, respectively. Then 1.5 M (4)  $(\text{MABr})_{0.9}(\text{PbI}_2)$  (DMSO:DMF = 1:4), and (5)  $(\text{FAI})_{0.9}(\text{PbI}_2)$  (DMSO:DMF = 1:4) were freshly prepared by dissolving MABr or FAI power in solution (3), respectively. Next, the solutions were mixed in the ratio of (4) (5) (1) (2) (3) = 190:950:60:60:60 (v:v) in sequence. The triple cation halide perovskite  $\text{Cs}_{0.05}\text{MA}_{0.15}\text{FA}_{0.80}\text{Pb}_{1.05}(\text{I}_{0.85}\text{Br}_{0.15})_3$  was prepared as follows. Briefly, first 1.5 M stock solution of 1 CsI (DMSO), (2)  $\text{PbBr}_2$  (DMSO:DMF=1:4), and (3)  $\text{PbI}_2$  (DMSO:DMF=1:4) were prepared, respectively. Then 1.5 M (4)  $(\text{MABr})(\text{PbBr}_2)$  (DMSO:DMF=1:4) and (5)  $(\text{FAI})(\text{PbI}_2)$  (DMSO:DMF=1:4) were freshly prepared by dissolving MABr or FAI power in solution 2 and solution (3), respectively. The perovskite spin-coating process was carried out at 2,000 rpm for 30 seconds. Initially, 50 mL of perovskite solution was dropped onto an FTO/c-TiO<sub>2</sub>/m-TiO<sub>2</sub> substrate. During the second spin coating step, 100 mL of chlorobenzene was dropped 15 s before completion. The samples were annealed at 100 °C for 1 h on a hot plate for crystallization. It is important to mention that the perovskite solution and its deposit were carried out in a glovebox, with an inert atmosphere and negligible humidity. (<5ppm of H<sub>2</sub>O and <1ppm of O<sub>2</sub>).

### **Halide Perovskite solutions (double cation)**

The double cation halide perovskite CsFA was prepared as follows. The precursor solution is comprised of 56 mg of CsI, 193 mg of FAI, 464 mg of  $\text{PbI}_2$ , 126 mg of  $\text{PbBr}_2$  in 1 mL of DMF and DMSO (4:1, v/v). The perovskite spin-coating process was carried out at 2,000

rpm for 30 seconds. Initially, 50 mL of perovskite solution was dropped onto an FTO/c-TiO<sub>2</sub>/m-TiO<sub>2</sub> substrate. During the second spin coating step, 100 mL of chlorobenzene was dropped 15 s before completion. The samples were annealed at 100 °C for 20 min on a hot plate for crystallization (the entire process was worked inside a glovebox).

### **Hole Transport Layer (HTL and Electrode)**

Carbon layer was blade-coated on top of the FTO/c-TiO<sub>2</sub>/m-TiO<sub>2</sub>/perovskite layer and annealed at 130 °C for 10 min on a hot plate.

### **Additive**

Next, the solutions were mixed in the ratio of (4) (5) (1) (3) = 150:800: 50: 100 (v:v) in sequence. The perovskite solution was doped with the additive 3-phosphonopropionic acid (H3pp), this procedure mixed the additive and the perovskite, and allowed it to dissolve without the need for heating or stirring.

### **Hole Transport Layer (HTL)**

Spiro-MeOTAD was deposited as HTL by dissolving 0.12 g of it in 1,130 mL of chlorobenzene, 23.5 mL of LiTFSI solution (1.8 M in acetonitrile), and 47.3 mL of TBP. These are dopants that are added to give the Spiro more conductivity. The resulting HTM solution is spin-coated at 4,000 rpm for 20 seconds. The finished devices were placed inside a dry air box for 12 h to fully oxidize the spiro-OMeTAD.

# Electrode

Finally, 80 nm of gold is deposited by thermal evaporation at high vacuum, the evaporation rate was controlled in different stages to limit the damage to the spiro-OMeTAD layer, which will act as metallic contact.

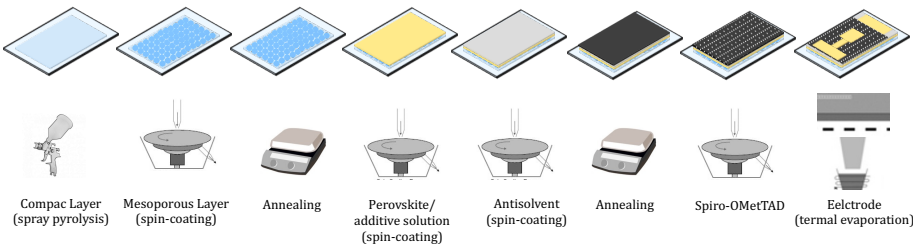


Figure 5.1. General device fabrication scheme (PSCs).

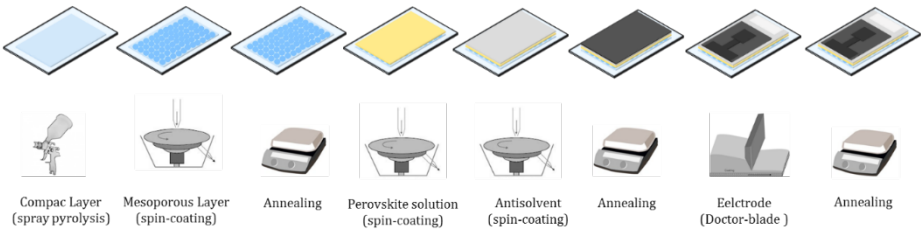


Figure 5.2. General device fabrication scheme (carbon-based PSCs).

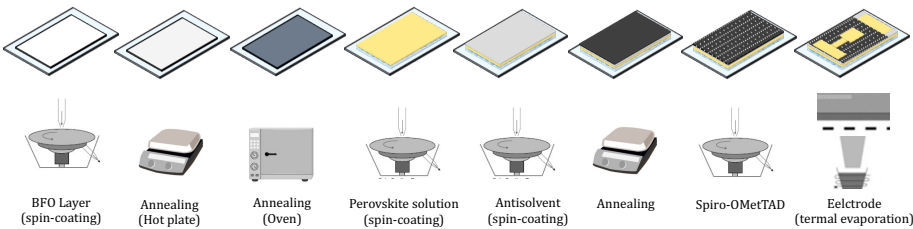


Figure 5.3. General device fabrication scheme (BFO-PSCs)

## **Spin coating technique**

The spin-coating technique is intended to deposit thin homogeneous films on flat substrates. For this, the solution to be used is deposited on the substrate either while the substrate rotates or is stationary to distribute the layer to the edge of the substrate by centrifugal force. Depending on the settings in the rotation program and the volume of solution used, a certain thickness is achieved. Another determining factor is the type of atmosphere in which the deposition occurs, since for certain reagents it is necessary to avoid the absorption of moisture. For this purpose, N<sub>2</sub> is normally used as carrier and inert gas. Figure 5.4 shows the spin coater equipment from Laurell Technologies model WS-650MZ-23NPP/LITE used in this thesis.



*Figure 5.4. Image of a spin coater used in this thesis.*

### Doctor-blade technique

The technique uses a doctor blade to remove excess paste from the smooth, non-engraved portions of the blade and the flat areas of the film walls. Doctor-blading technique was used here in order to save gold electron costs and because the use of this technique makes the process eco-friendlier.

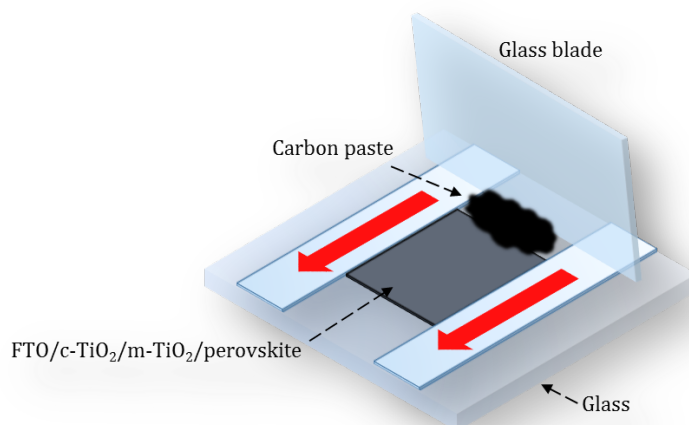


*Figure 5.5. Carbon deposition according to the doctor-blade technique.*

### Thermal evaporation technique

Thermal evaporation technique is a high vacuum technique for thin film deposition. The equipment used for this technique consists mainly of high vacuum pumps, and a chamber inside which a support is inserted to place the substrate on which the layer will be deposited. It also consists of a system to heat and evaporate the deposited material. In the equipment used, the substrate is placed inverted on top of the chamber. A filament or a pot was used as a container for the material to be evaporated, which is heated by

passing current through it. The filament and the pot are commonly made of tungsten or molybdenum and the material to be deposited is placed inside. The purpose of passing the current flow is to heat the material until its melting point is exceeded and thus, the vapor of the material is deposited on the surface of the substrate (See Figure 5.6).

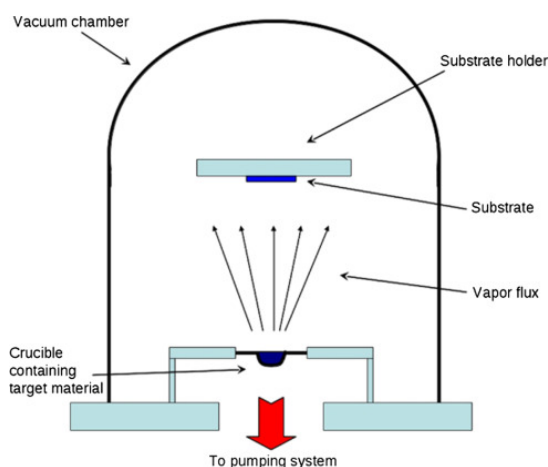


Figure 5.6. Thermal evaporation equipment.

### 5.2.2. Characterization

#### **Electron energy loss spectroscopy (EELS)**

The EELS (Electron Energy Loss Spectroscopy) analytical technique is based on the measurement of the energy distribution of an electron beam after passing through a thin sample to analyse its physical-chemical properties. The EELS detector is usually placed at the end of the column of a TEM (Transmission Electron Microscope) or STEM (Scanning TEM) microscope. In these microscopes, a high-energy electron beam (60 – 300 kV) is generated to analyse the



sample. As its name suggests, the electrons must be "transmitted" through the sample, which implies that the sample is extremely fine. Electrons can be scattered by the sample either elastically (without energy exchange) or in elastically, the latter being the ones used in EELS to extract information from the sample. A focused ion beam (the samples were deposited with a Pt/carbon film on Au, in order to protect the sample in the process) (FIB, Zeiss Crossbeam 1560XB) was applied to prepare the HRTEM measurements.

### **Scanning electron microscopy (SEM)**

The interaction between an electron beam with a very high acceleration potential (50-30 Kv) produces a response of the sample that translates into secondary electrons (SE), backscattered electrons (BSE), X-radiation and others. Collecting the information provided by the SE and BSE electrons allows us to obtain a topographical image (three-dimensional) produced by tracing the electron beam over the sample, while in the case of X-radiation it will help us to know the elemental composition of the sample. Figure 5.7 shows the SEM equipment used in this present work.

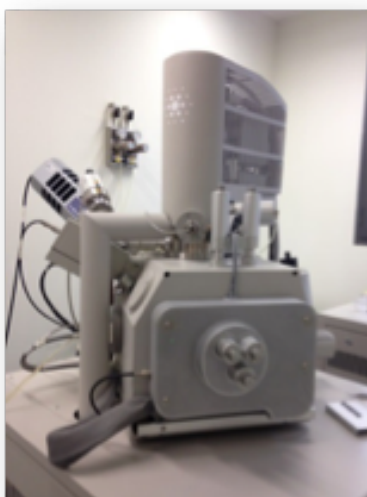


*Figure 5.7. Image of the SEM equipment used in this thesis.*

### **X-ray diffraction (XRD)**

The X-ray diffraction (XRD) technique is based on the diffraction phenomenon which consists of the interaction of electromagnetic waves with a material that has dimensions comparable to the wavelength of the radiation used. The first person to discover X-rays was W.C. Röntgen in 1895. He observed that these rays passed through the human body, but he did not know their nature, so he called them X-rays, zhu et al. 2011.

X-rays are generated when a certain material is bombarded with electrons at high speeds, which are used to remove electrons from the inner orbitals of atoms in the material, removing the stability of atoms, causing electrons in higher orbitals to fall, filling the empty internal orbitals, emitting the energy released in the form of an X-

ray photon. The material commonly used for X-ray generation is copper, Zhu et al. 2011.

The X-rays generated are incident at an angle  $\theta$  on the material and are diffracted by the atoms; such diffracted rays will have constructive interference if their optical path difference is an integer multiple,  $n$ , of the wavelength of the light. In the geometry of Figure 5.8, where atoms in crystalline planes separated by a distance  $d$  are considered, the constructive interference is fulfilled when the so-called Bragg's Law is fulfilled:

$$n\lambda = 2d * \sin (\theta)$$

where  $n$  is an integer,  $\lambda$  is the wavelength of the X-rays,  $d$  is the plane distance between the crystal lattice, and  $\theta$  is the angle between the incident rays and the scattering planes.

The X-rays that fall on the crystal surface and are diffracted at a certain angle and that are in phase are analyzed, thus forming constructive interference. The interference is constructive when the phase difference between the radiation emitted by different atoms is proportional to  $2\pi$ .

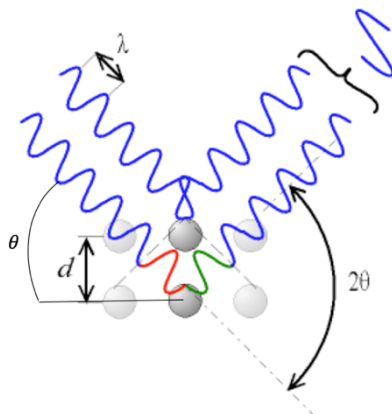


Figure 5.8. Two-wave diffraction with constructive interference.

The intensity of the diffracted beams is recorded by a detector moving through the angle  $2\theta$ . In such a way that it is possible to have a graph, called a diffractogram, of the recorded intensity with respect to the angle  $2\theta$ . By means of Bragg's Law, the values of the angle in which there are diffraction maxima can be related to the distance between planes, and with this the crystalline structure of the material is determined. Depending on the configuration of the equipment it is possible to analyze both powders and thin films, Pauling et al. 2016. Figure 5.9 shows the XRD equipment used for the samples of this present work. The XRD is the Empyrean (PANalytical) equipment with a ceramic tube (Cu anode,  $\lambda = 1.54060 \text{ \AA}$ ), pixel1D detector (PANalytical).



*Figure 5.9. Image of the X-Ray diffraction equipment used in this thesis.*

### **Atomic Force Microscopy (AFM)**

This technique, known as atomic force microscopy (AFM), makes it possible to obtain, like the SEM technique, topography images at the micrometric and nanometric scale, in a simple way and in both conductive and insulating samples, in the form of films, solids and liquids. The AFM consists of a peak placed on a cantilever; when the peak, ideally ending in an atom, approaches the surface of the material, it experiences a repulsion due to Van Der Waals forces with the surface atoms, causing the cantilever to deflect. Such deflection will cause a laser reflected in the cantilever to hit a photodetector at different positions, so that in areas of the sample where the height is greater, the cantilever will flex, generating a change in the position of the laser with respect to the photodetector. The displacement of the laser in the photodetector will then be related to the height at

which the atoms are found in the sample. Thus, by scanning the sample with the cantilever and recording the position of the laser in the photodetector, it is possible to form a topography image.

### **Electrochemical impedance spectroscopy (EIS)**

By using the PAIOS Fluxim equipment, we can perform all-in-one electrical measurement for the solar devices and measure the capacitance-frequency measurements of PSCs devices. All samples were performed under white LED illumination with a light intensity close to one sun.

### **Light intensity dependent $V_{oc}$ , transient photocurrent (TPC) and open circuit voltage decay (OCVD)**

These tests were used for analysing PSCs devices by PAIOS Fluxim equipment, in which we can perform all-in-one electrical measurements of the devices. TPC, Light intensity dependent  $V_{oc}$ , and OCVD measurements should be done under white LED illumination and ranging intensity from 0.3 to 1 sun for  $V_{oc}$ . For TPC and OCVD measurements, the intensity will be 1 sun.

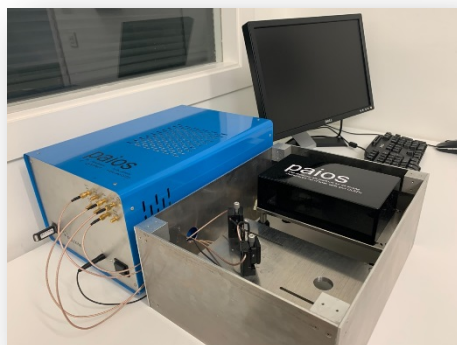


*Figure 5.10. Image of the PAIOS equipment used in this thesis.*

### **Photoluminescence quantum efficiency (PLQE), steady-state photoluminescence (PL) and time-resolved photoluminescence (TRPL)**

PLQE and PL measurements require the use of an integrating sphere and a continuous wave laser ( $60 \text{ mW/cm}^2$ ) for photoexcite the film at 532 nm. On literature we can find the main protocols for perform and calculate the PLQE measurements [1], so we are not going to describe it in this thesis. However, for TRPL measurements, we use a 509 nm pulsed semiconductor laser (1 MHz repetition rate). It's important to remark, that all these measurements should be done in a  $\text{N}_2$  ambient, in order to prevent fast degradation of the samples prior to device characterization.

### **Optical pump-THz probe (OPTP) spectroscopy**

All the photoconductivity tests performed in this thesis carry through an optical pump THz probe (OPTP) spectroscopy. Also, like

in previous tests, the OPTP recordings must be done in a N<sub>2</sub> atmosphere to avoid THz absorption in the air [2][3][4].

### **UV-Visible (UV-Vis)**

UV-Vis spectroscopy uses electromagnetic radiation from the visible and ultraviolet regions of the electromagnetic spectrum. This radiation, which falls on the sample, is partially absorbed, generating a transition between the energy levels of the sample. The rest of the radiation is initially transmitted or reflected. In this work, ultraviolet-visible absorption spectroscopy was used in different thin films. To determine the wavelength, range of the applied HTL and ETL, to analyse which were capable of absorbing maximum intensity and to evaluate their transparency. Figure 5.11 shows the UV-visible absorption equipment used in this work.

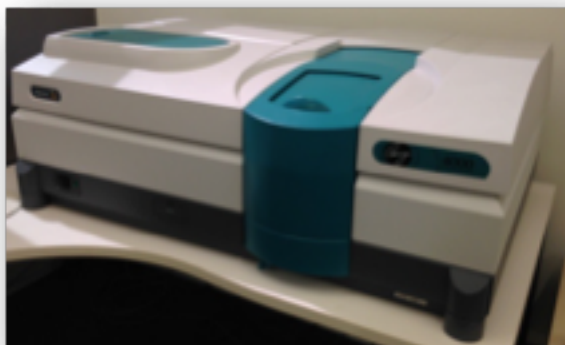


*Figure 5.11. Image of the UV-Visible spectrophotometer used in this thesis.*



### **Tauc Model.**

The Tauc Model, also known as the Tauc plot, is used to determine the energy gap of materials. Here, from the data determined by UV-Vis spectroscopy in the absorbance mode, the term  $\alpha h\nu^{1/r}$  is plotted against the wavelength-dependent energy of light, where  $h$  is Planck's constant,  $\alpha$  is the absorption coefficient of the material,  $\nu$  is the photon frequency and  $r$  is determined by the band transition mode of the material, Stenzel et al. 2005:

$r = 1/2$  for direct allowed transitions.

$r = 3/2$  for direct disallowed transitions.

$r = 2$  for indirect allowed transitions.

$r = 3$  for indirect disallowed transitions.

Extrapolated to the abscissa axis, the value where this axis touches corresponds to the energy gap value of the material (Stenzel et al. 2005), since the starting point where the linear growth begins on the graph will denote the beginning of the absorption of light by the material.

### **Fourier transform infrared spectroscopy (FTIR)**

Infrared spectroscopy is used for the identification and study of the functional groups of the molecules that make up the material to be analyzed. FTIR spectra reveal the composition of solids, liquids, and gases. The content of the information is very specific in most cases, which allows fine discrimination between similar materials. The speed of FTIR analysis makes it particularly useful in detection applications, while the sensitivity drives many advanced research

applications. Figure 5.12 shows the Fourier transform infrared spectroscopy (FTIR) equipment used in this work. FTIR is the TENSOR 27 FTIR (Bruker).



*Figure 5.12. Image of the FTIR equipment used in this thesis.*

## **Profilometry**

The profilometry scans a surface with a small needle and records differences in height. The lateral resolution is in the micrometer range due to the diameter of the needle tip, but the height resolution is in the nanometer range. The thickness of the active layer was measured using a profilometry. In order to measure the thickness of the films, a step was made in the center of the substrate. This step was created using a point, hard enough to scratch the surface of the active layer, wet with chlorobenzene. The contact profilometry does not require any modelling. Figure 5.13 shows the profilometry used in this present work.

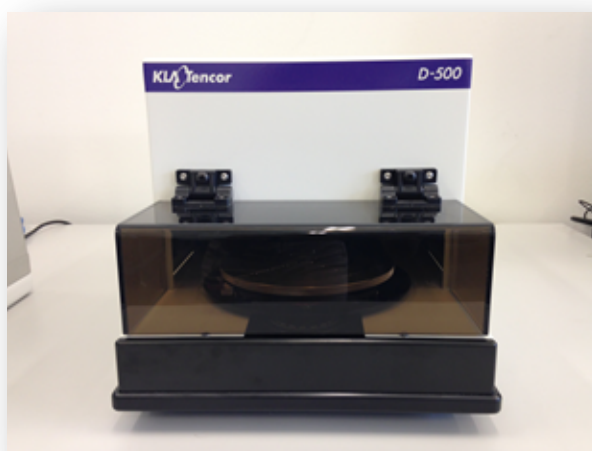


*Figure 5.13. Image of the profilometer used in this thesis.*

### **Solar cell characterization**

The devices were characterized by current density vs. voltage (J-V) measurements under light, in order to calculate the performance parameters of the cells. With a Keithley 2400 source measurement unit, measurements were made under JV light under the AM 1.5G spectrum at a light intensity of  $100 \text{ mW/cm}^2$  using the commercial solar simulator equipped with an arc lamp housing (Newport, model 66902, 50–500 W) using an arc lamp. of 450 W xenon. The voltage sweep rate was  $10 \text{ mV/s}$ . Cells were masked to obtain an active area of  $0.16 \text{ cm}^2$ . Light intensity was calibrated using a monocrystalline silicon cell certified by the National Renewable Energy Laboratory (NREL). All J-V characteristics were measured at room temperature.

### **Incident Photon-to-Current Conversion Efficiency (IPCE)**

An important indicator of solar cell performance is external quantum efficiency (EQE), which is defined as the percentage of

incident photons that are converted into charge carriers collected by the solar cell electrodes. That is, EQE tells us how efficiently incident light of different wavelengths is being converted into charge carriers and collected. The EQE depends on light absorption, transport and recombination of charge carriers as follows:

$$EQE = \eta_A \times \eta_{ED} \times \eta_{CS} \times \eta_{CC}$$

where  $\eta_A$  is the absorption efficiency,  $\eta_{ED}$  is the exciton dissociation efficiency,  $\eta_{CS}$  is the exciton separation efficiency, and  $\eta_{CC}$  is the charge collection efficiency. Figure 5.14 shows the equipment to measure the EQE used in this thesis work. This kit consists of a xenon lamp, a motorized monochromator, and a power meter, both from Newport. The monochromator is used to separate photons of a particular wavelength, by using an internal grating structure. The intensity of the irradiated light and the photocurrent were measured simultaneously, and the data was processed through the Lasing scan software, supplied by the manufacturer of the equipment. The system was calibrated using a monocrystalline silicon cell. All EQE measurements were carried out in the wavelength range of 300 nm to 800 nm.



*Figure 5.14. The IPCE setup used in this thesis.*

### **Stability analyses**

Degradation analysis was performed, the devices were subjected to a space with nitrogen as an inert gas in a sealed support, under continuous illumination and monitoring of the maximum power point at RT (25 °C). The light source consisted of a matrix of white LEDs powered by a constant current. The type of LED is LXM3-PW51 with an emission spectrum of 400 to 750nm. Equivalent solar intensities were calibrated using a calibrated Si reference diode equipped with a KG-5 filter. As for the protocol followed to study the stability of the devices, it was performed following the ISOS-L protocol for PSCs [5].

### **Charge Extraction, Transient Photocurrent Spectroscopy, and Impedance Analysis**

Charge extraction (CE), Transient Photocurrent Spectroscopy (TPC) and Impedance analysis was performed using the all-in-one measurement system PAIOS 3.2 (FLUXiM AG). PAIOS exploits a first function generator to control the light source (a calibrated white LED with a rise/fall time of 100 ns) and a second function generator to control the applied voltage bias. For TPC, a pulse width of 20  $\mu$ s was used with a settling time and follow-up time of 100  $\mu$ s. Light Intensity sweep and Voltage sweep were set between 1 to 100% and 0 to -2 V.

### **Multi I-V Tracking**

After poling once, the device parameters reach an optimum value, repeated I-V scans were performed after every 5 seconds. This was done in the same setup as for normal IV scans and poling experiments. The scan rate was fixed to 500 mV/s along with the optimum biasing condition achieved for that device. This helped to maintain a constant poling effect, also simultaneously tracking the parameters and MPP. The poling effect could not have been achieved by using a classical MPP algorithm.

### ***XPS & UPS: X-ray Photoelectron Spectroscopy (XPS) and Ultraviolet photoelectron spectroscopy (UPS):***

Measurements by XPS and UPS were carried out using a PHOIBOS 150 MCD spectrometer (SPECS) under ultrahigh vacuum conditions (base pressure  $3\text{E-}10$  mbar). The XPS measurements were carried out with an X-ray source (Al-K $\alpha$ , with an energy of 1486.6 eV and a power of 300 W) and the UPS measurements were carried out with a monochromatic HeI UV source (21.2 eV). Work function determination was performed by applying a -10 V bias to the samples. All measurements were taken at room temperature in an ultrahigh vacuum chamber. Figure 5.15 shows an image of the XPS/UPS equipment used in this present work.

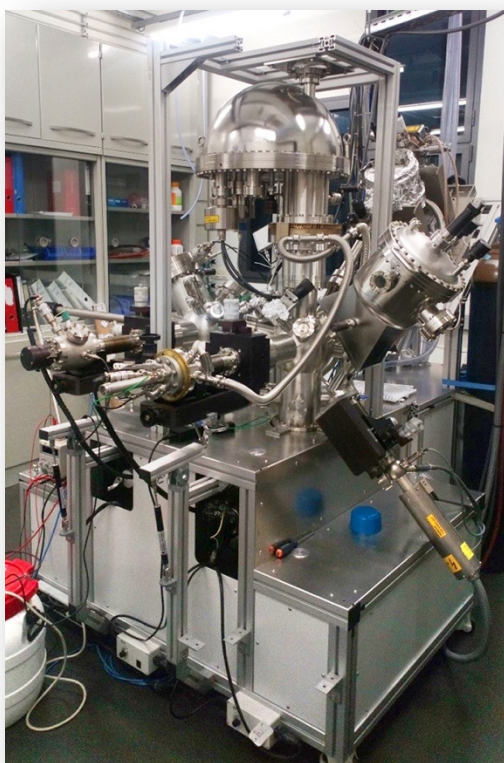


Figure 5.15. XPS and UPS equipment.

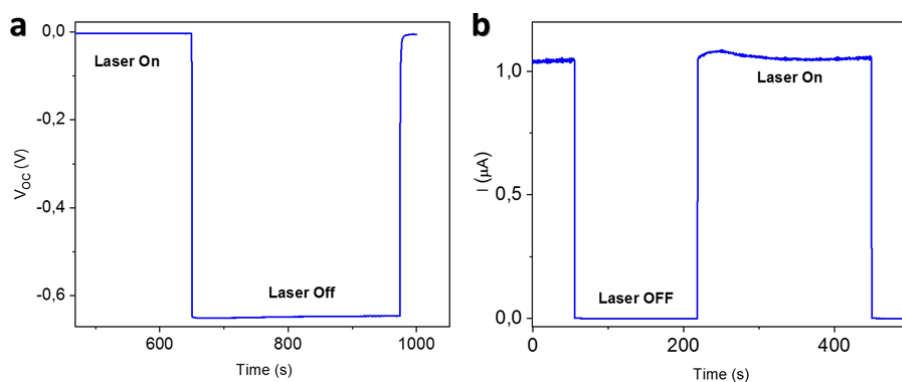


Figure 5.16. a) Open circuit potential ( $V_{oc}$ ) of a capacitor measured as a function of time with and without illumination at RT. b) Short-circuited photocurrent density measured in the film with and without illumination at RT.

### 5.3. References

- [1] J. C. de Mello, H. F. Wittmann, and R. H. Friend, "An improved experimental determination of external photoluminescence quantum efficiency," *Adv. Mater.*, vol. 9, no. 3, pp. 230–232, Mar. 1997.
- [2] J. Xing, Q. Wang, Q. Dong, Y. Yuan, Y. Fang, and J. Huang, "Ultrafast ion migration in hybrid perovskite polycrystalline thin films under light and suppression in single crystals," *Phys. Chem. Chem. Phys.*, vol. 18, no. 44, pp. 30484–30490, Nov. 2016.
- [3] J. Zhao *et al.*, "Strained hybrid perovskite thin films and their impact on the intrinsic stability of perovskite solar cells," *Sci. Adv.*, vol. 3, no. 11, 2017.
- [4] Y. Yuan *et al.*, "Photovoltaic Switching Mechanism in Lateral Structure Hybrid Perovskite Solar Cells," *Adv. Energy Mater.*, vol. 5, no. 15, p. 1500615, Aug. 2015.
- [5] M. V. Khenkin *et al.*, "Consensus statement for stability assessment and reporting for perovskite photovoltaics based on ISOS procedures," *Nat. Energy*, vol. 5, no. 1, pp. 35–49, Jan. 2020.



# Chapter 6: General Conclusions

---

From this thesis work we can extract some general conclusions involving the use of additives on the perovskite-based solar cells, the carbon-based perovskite solar cells or the use of ferroelectric oxides as electron transport layers. The main conclusions are presented divided by research topic:

## **Additive engineering**

- PSCs with phosphonopropionic acid (H3pp) family additive contains carboxylate and phosphonate functional groups.
- The H3pp additive does not change the photovoltaic properties from the PSC without additives, reaching  $V_{oc}$  of  $\sim 1.1$  V and PCE of  $\sim 21\%$  in presence of the additive.
- The PSCs with H3pp shows long-term stability properties under continuous light irradiation and it can retain the initial PCE after 1000 h under MPP operational conditions and light irradiation.
- H3pp improves nanostructural quality as a thin film absorber without changing the grain size of the H3pp:HP thin film.

- The strong interaction between HP and H3pp is created via the phosphonate group and include two types of hydrogen bonds. This enables ion immobilization and long-term stability by passivation of shallow point defects.

### **Carbon-based perovskite solar cells**

- We fabricated carbon-based perovskite solar cells (C-PSCs) with long-term stability and low-cost methodology by eliminating HTM, increasing the PSCs fabrication.
- A depletion region in C-PSCs is observed, shedding light on their mechanism, and demonstrated a high open-circuit voltage without HTM.
- Thermal and humidity stress modify PV stability and device performance, as hysteresis suppression, stabilizing solar cells and the structural properties of the perovskite absorbent.
- C-PSCs retain 90% of the initial efficiency after 100 h of thermal stress and showed a loss of 60% after 30 h, resulting in more stable device.
- The C-PSCs are promising and will be more competitive in the future with additional innovation strategies: materials, interfaces, device structures, additive engineering, stability etc.

## **Ferroelectric oxides as electron transport layers**

- We have prepared PSCs using ferroelectric oxides such as Bismuth Ferrite and Lead Zirconate Titanate as ETL.
- Bismuth Ferrite ( $\text{BiFeO}_3$ , BFO) was synthesized by sol gel solution and applied by spin coating on top of the FTO electrode.
- The BFO thin film was applied as a dense thin layer and a coating of the halide perovskite was deposited on top in a perovskite oxide/halide perovskite heterojunction.
- The as-prepared PSC observed almost null photovoltaic response with  $V_{\text{OC}}$  in the range of 0.9 V and  $J_{\text{SC}}$  in the range of 3  $\text{mA}/\text{cm}^2$ . The application of poling (bias voltage) to the PSC allowed the slow but constant enhancement of the photovoltaic properties with time reaching values of 0.925 V for  $V_{\text{OC}}$  and 16.61  $\text{mA}/\text{cm}^2$  for  $J_{\text{SC}}$ .
- The poling was carried out under AM 1.5G light irradiation at room temperature.
- Conductivity measurements performed to the BFO thin film confirmed the change in conductivity of the BFO in agreement with the improvement of PCE of the solar cell. This indicates that the initial ferroelectric oxide modifies its

transport properties from being an insulator to conductor in detriment to its ferroelectric properties.

- We also observed a dependency of the halide perovskite grain size on the final photovoltaic properties of the devices.
- In general, for halide perovskites with small grain sizes, the photovoltaic properties of the PSC improve with poling under light irradiation. On the contrary, large grain sizes results in detrimental effect of the photovoltaic properties of the solar cells with time. We initially attributed this effect to a difference in transport properties of the halide perovskite. Published reports indicate a possible horizontal and vertical transport of charges was observed for large and small grain sizes, respectively.
- However, although our PFM studies confirm higher conductivity and transport properties for the sample with small grains, we believe the grain boundaries play an important role. The smaller grain sizes allow for large amount of grain boundaries which are better electron paths for conductivity. The later is still under evaluation in our group.

Our results demonstrate that the FE oxide-based solar cells show good photovoltaic properties and stability even under conditions of UV light irradiation which confirms that the BFO provides enhanced stability to the solar cells.



# List of Publications

---

1. **Pereyra, C**; H Xie, et al., M. Lira-Cantu. Metal Oxides in Stable and Flexible Halide Perovskite Solar Cells: Towards Self-Powered Internet of Things. in Ahmad, S; Kazim, S. Grätzel, M. (Eds.): Perovskite Solar Cells. Materials, Processes, and Devices, Wiley-VCH.2021.
2. **Pereyra, C.**, Xie, H., Lira-Cantu, M. Additive engineering for stable halide perovskite solar cells. Journal of Energy Chemistry, 2021, 60, pp. 599–634.
3. Xie, H., Wang, Z., Chen, Z., **C. Pereyra**, ..Hagfeldt, A., Lira-Cantu, M. Decoupling the effects of defects on efficiency and stability through phosphonates in stable halide perovskite solar cells. Joule, 2021, 5(5), pp. 1246–1266
4. Hernández-Balaguera, E., del Pozo, G., Arredondo, B., **C. Pereyra** ...Xie, H., Lira-Cantú, M. Unravelling the Key Relationship Between Perovskite Capacitive Memory, Long Timescale Cooperative Relaxation Phenomena, and Anomalous J–V Hysteresis. Solar RRL, 2021, 5(4), 2000707.



5. Martinez, V.C., Xie, H., Mingorance, A., **C. Pereyra**, ...Narymany, A., Gómez, M.M. Carbon-based perovskite solar cells by screen printing with preheating. Journal of Physics: Conference Series, 2020, 1433(1), 012009
6. Enrique Hernández-Balaguera, Laura Muñoz-Díaz, ..., **Carlos Pereyra**, Mónica Lira-Cantú, Mehrdad Najafi, Yulia Galagan. Universal control strategy for anomalous ionic-electronic phenomenology in perovskite solar cells efficiency measurements. Submitted.
7. **Pereyra, C.** Xie, H; ... M. L. Calzada, M. Lira-Cantu. BFO as electron transport material in Halide perovskite solar cells. In preparation.
8. **Pereyra, C.** Xie H., ... M. Lira-Cantu. Tuning the switching response of halide perovskites through grain size variation. In preparation.

# Acknowledgements

---

This work has been presented to obtain the mention of PhD on Chemical at the Universitat Autònoma de Barcelona (UAB). The experimental work has been carried out at the Nanostructured Materials for Photovoltaic Energy Group of the Institut Català de Nanociència i Nanotecnologia (ICN2-CSIC) under the direction of Prof. Monica Lira-Cantú. A special thanks to all the members of the group who are still here and those who have already left, who have collaborated in this work. Also, thanks to the ICN2 staff, for the technical and administrative support.

Thanks to the government of Mexico and the support granted through the CONACYT scholarship for the completion of this doctoral thesis.

Thanks to SolarEra.Net Cofund 2 (EU) and Agencia Española de Investigación (AEI) for the PrOperPhotoMiLe project (PCI2020-112185) and the Self-Power project (PID2019-104272RB-C54 / AEI /10.13039/501100011033). Also thank the Agència de Gestió d'Ajuts Universitaris i de Recerca (AGAUR) of the Generalitat de Catalunya for its support in the consolidation of the 217 SGR 329 group and the Xarxa d'R + D + I Energy for Society (XRE4S). Thanks to the Ministerio de Economía y Empresa (MINECO; No. SEV-2017-0706) and the CERCA program of the Generalitat de Catalunya.



Thanks to Prof. Feng Gao and Fan Fu of the Department of Physics, Chemistry and Biology (IFM) and Linköping University, Linköping, Sweden and the Laboratory for Thin Films and Photovoltaics, Empa—Swiss Federal Laboratories for Materials Science and Technology, Switzerland, for the TAS measurements carried out.

Thanks to Prof. Suxha Tao and his laboratory at TUE (Netherlands) for the density functional theory (DFT) calculations.







